ADVANCED
ENERGY
MATERIALS
www.advenergymat.d

Smart Windows: Electro-, Thermo-, Mechano-, Photochromics, and Beyond

Yujie Ke, Jingwei Chen, Gaojian Lin, Shancheng Wang, Yang Zhou, Jie Yin, Pooi See Lee,* and Yi Long**

A smart window that dynamically modulates light transmittance is crucial for building energy efficiently, and promising for on-demand optical devices. The rapid development of technology brings out different categories that have fundamentally different transmittance modulation mechanisms, including the electro-, thermo-, mechano-, and photochromic smart windows. In this review, recent progress in smart windows of each category is overviewed. The strategies for each smart window are outlined with particular focus on functional materials, device design, and performance enhancement. The advantages and disadvantages of each category are summarized, followed by a discussion of emerging technologies such as dual stimuli triggered smart window and integrated devices toward multifunctionality. These multifunctional devices combine smart window technology with, for example, solar cells, triboelectric nanogenerators, actuators, energy storage devices, and electrothermal devices. Lastly, a perspective is provided on the future development of smart windows.

1. Introduction

Smart window refers to the on-demand window that can dynamically modulate light transmittance. It is recognized as a promising technology to economize building energy consumption by controlling the indoor solar irradiation.[1–7] The usage of building energy accounts for 30–40% of total energy consumption in developed countries, excessing the amount for industry or transportation.[5,8–11] Around 50% energy for building services is contributed by the heating, ventilation, and air conditioning (HVAC) system.[5,10] More importantly, both the building and the HVAC energy consumptions are predicted to increase in the next two decades.[10] Windows are considered as the least energy-efficient components of buildings,[12,13] therefore smart windows are becoming increasingly important as they are capable of reducing the HVAC energy usage by tuning the transmitted sunlight in a smart and favored way: blocking the solar irradiation in hot days, while passing through in cold days.[6,14–17] Besides for building energy efficiency, the technology has been attracting strong interests as functional devices in extensive areas, including the dynamic windows for privacy, the windows for civil aircraft, the sunroofs of automobiles, the covers for greenhouses, and the switchable sunglasses.[3,5,18–20]

The driving force behind the research interest in both the academic and industrial communities is the huge business market of the functional windows as well as to achieve the beautiful vision of an energy-efficient society.[4,18,21,22] The installed windows are ≈400 million square feet each year in the United States, while accounts for less than 10% of the global demand.[18,23,24] The size of the global market of smart windows was valued at \$2.8 billion in 2016 and is estimated to reach \$8.35 billion in 2023 with an average growth ratio of 16.6%.[25] Compared with traditional static windows, such as the low-emissivity windows, the smart windows are suggested to reduce ≈10% of total building energy usage.[23,26] Investments for companies have been rising for the smart window technology targeting occupants' comfort and energy saving.[27,28]

Smart window technology has attracted significant scientific interests and undergone rapid development in the last decade, including several categories of windows based on different stimuli. Significant research effort has been put onto the windows based on electro-, thermo-, mechano-, and photoresponses (**Figure 1**). Among them, the electrochromic (EC) window is the most attractive category that undergoes a gradual evolution in many years and several commercialized EC windows are now available in market.[29–32] It is commonly constructed of a sandwich structure with a functional material

---

Dr. Y. Ke, Dr. J. Chen, S. Wang, Dr. Y. Zhou, Prof. P. S. Lee, Dr. Y. Long
School of Materials Science and Engineering
Nanyang Technological University
50 Nanyang Avenue, Singapore 639798, Singapore
E-mail: pslee@ntu.edu.sg; longyi@ntu.edu.sg
Dr. G. Lin
School of Mechatronical Engineering
Beijing Institute of Technology
Beijing 100081, China
Prof. J. Yin
Department of Mechanical and Aerospace Engineering
North Carolina State University
Raleigh, NC 27695, USA
E-mail: jyin8@ncsu.edu
Prof. P. S. Lee, Dr. Y. Long
Singapore-HUJ Alliance for Research and Enterprise (SHARE)
Nanomaterials for Energy and Energy Water Nexus (NEW)
Campus for Research Excellence and Technological Enterprise (CREATE)
1 Create Way, Singapore 138602, Singapore
Dr. Y. Long
Sino-Singapore International Joint Research Institute (SSIJRI)
Guangzhou 510000, China

The ORCID identification number(s) for the author(s) of this article can be found under https://doi.org/10.1002/aenm.201902066.

DOI: 10.1002/aenm.201902066

layer between two transparent electrodes while the thermo- and photochromic windows have relatively more rapid advance in recent years. The thermochromic (TC) window is adopting thermal-responsive materials that can either coated on the glass surface as solid glazing or be encapsulated properly between two glasses. More technical details can be referred to the previous reviews focusing on the EC[3] and the TC.[4] Similar to the TC, the photochromic (PC) window is commonly based on photoresponsive solid glazing. The more recent mechanochromic (MC) smart window relies on the materials that display reversibly structure change, such as surface morphology and the configurations, in response to an external strain. The functional material plays a dominant role for light modulation in smart windows as it can display different states with distinct different optical properties due to either the chemical composition or the structure changes. The various stimulus-response mechanism and each material system is elaborated in different sections.

In the review, the recent progress of smart windows is overviewed, from the electro-, thermo-, mechano-, to photochromics, with particular attention on the functional materials. We outline the categories and discuss the advantages and disadvantages through comparisons. We systematically discuss the strategies for all four types of smart windows. We also summarize the integrated devices based on electro- and thermochromics toward multifunctionality. Lastly, our perspective in the smart windows is provided for future development.

2. Electrochromics

EC devices, typically consisting of multilayer structures (EC material, electrolyte, and ion storage layer) sandwiched by two transparent conductive electrodes (TCE), can reversibly modulate the optical properties upon application of potential.[3,33,34] Widely used TCE layers are indium tin oxide (ITO)-coated glass and fluorine-doped tin oxide (FTO)-coated glass due to the high transmittance and high electronic conductivity.[3,35] The EC material modulates its optoelectronic properties upon electrically induced cation insertion/extraction.[3,33,36] Common EC materials include inorganic metal oxides (WO_3, NiO, Nb_2O_5, TiO_2, V_2O_5, Ta_2O_5, MoO_3, etc.),[1,33] Prussian blue, conductive polymers (poly-3,4-ethylenedioxythiophene (PEDOT), polyaniline (PANI), polypyrrole, etc.), viologens, and transition metal-coordination complexes,[33,37] while NiO, CeO_2, and IrO_2 are commonly used as ion storage layer.[3] EC devices have found wide applications in smart windows, electronic displays, self-dimming rear mirrors, camouflage among others.[3,35] Smart EC windows, with the capability of reducing energy consumption, offer privacy and comfort for occupants, is one of the key feature for green buildings.[36] The ultraviolet (UV) durability of polymer-based EC materials is often unsatisfactory and therefore they are restricted to indoor applications.[3] In order to facilitate the wide application of EC technology, high color modulation, long-term cycling stability, high coloration efficiency (CE), and fast switching kinetics are highly desirable, while different colors are also being pursued.[37] Aside from reversible optical modulation, EC devices with extra functionalities are also of increasing interests to expand the application areas and open up more possibilities for the commercialization of EC devices.[35] There have been a few comprehensive reviews discussing the fabrication of scalable and flexible EC smart windows.[35,37,38] Here we mainly summarize the strategies to improve the performance of EC materials, and highlight the recent advances in multifunctional EC devices reported in the last 2–3 years.

Jie Yin is currently an Assistant Professor in the Department of Mechanical and Aerospace Engineering, North Carolina State University, Raleigh, NC, USA. He worked as an Associate Professor at Temple University and Postdoctoral Associate at Massachusetts Institute of Technology. He obtained his Ph.D. degree from Columbia University and M.S. from Tsinghua University. His research focuses on multifunctional interfacial materials for energy saving and water harvesting, mechanical metamaterials, and soft robotics.

Pooi See Lee is a full Professor in the School of Materials Science and Engineering, Nanyang Technological University. She obtained her B.Sc. (Hons) and Ph.D. degrees at the National University of Singapore. Her research focuses on nanomaterials for energy and electronics applications, flexible and stretchable devices, electrochemical inspired devices, and human–machine interface.

Yi Long is a Senior Lecturer in the School of Materials Science and Engineering, Nanyang Technological University. She obtained her Ph.D. degree from the University of Cambridge, UK. She has successfully implemented technology transfer from lab to industry for hard-disk company in her early career life. Her recent research is to develop micro/nanostructured functional materials and devices with focus on energy-saving smart windows and flexible/stretchable electronics.

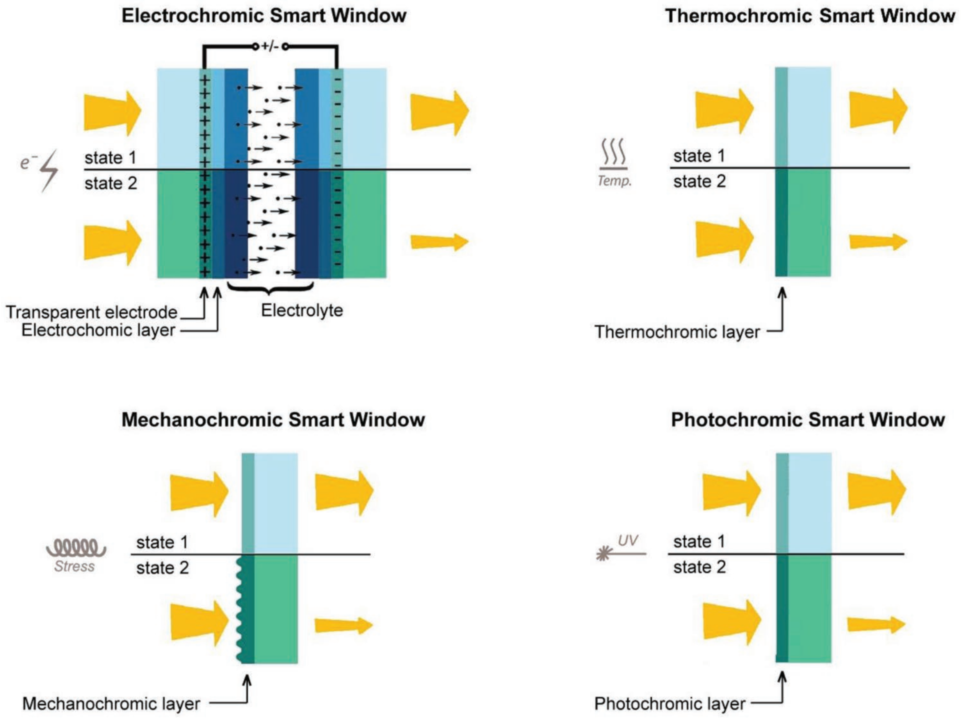

Figure 1. Illustration of the four types of smart windows: the electro-, thermo-, mechano-, and photochromic windows.

2.1. Strategies to Improve Electrochromics

2.1.1. Inorganic Electrochromic Metal Oxides

Nanostructured EC Materials: The optical modulation of inorganic EC metal oxides (ECM) is realized by electrochemically driven ion insertion/extraction, during which diffusion of ions in the ECM can be the rate limiting steps.[36] ECM with nanostructures and high specific surface areas are expected to deliver superior EC performance due to the shortened diffusion length and improved electrolyte exposure.[1,37,39] Improved EC performance resulted from tuning the nanostructures of ECM has been reported.[39–43] For example, Lee and co-workers reported that porous and interconnecting WO_3 networks can be obtained by pulse deposition with an interval time of 1.1 s as shown in **Figure 2**a, instead of compact WO_3 film obtained by continuous electrodeposition.[44] The porous WO_3 film delivers higher current densities evident from the cyclic voltammograms (CV) compared to compact WO_3 film as shown in Figure 2b, indicating the superior EC properties of porous WO_3 film. The porous WO_3 film exhibits larger optical modulation (97.7% at 633 nm) as displayed in Figure 2c, faster switching kinetics (t_c (coloration time) = 6 s, t_b (bleaching time) = 1.9 s), higher CE (118.3 $cm^2\ C^{-1}$) and better cycling stability (≈100% after 300 cycles) than the compact film, which is mainly attributed to its porous structure that enables fast charge transfer and facile electrolyte penetration as well as alleviates WO_3 expansion upon H^+ insertion/extraction. Similar protocols were also found to be effective in realizing increased EC performance in films consisting WO_3 nanotrees instead of WO_3 nanowires (NWs),[40] honeycomb-like porous WO_3 films over the drop-casted dense WO_3 films[42] and the hollow spherical WO_3 film over the radio frequency–sputtered dense WO_3 films.[43]

Hybrid EC Materials: Different EC materials have their respective pros and cons, thus aside from nanostructure engineering, it is also feasible to hybrid different materials into the EC layer, aiming at harvesting the advantages of respective components.[45,46] For example, as shown in Figure 2d, TiO_2–WO_3 inverse opal (IO) film obtained by two-step deposition delivered enlarged contrast of 65% at 1033 nm and also higher CE of 111.88 $cm^2\ C^{-1}$ as shown in Figure 2e,f, as well as extended cycling stability of 1200 cycles with contrast retention of 90%, superior to that of the WO_3 thin film.[47] The increase in the EC performance of TiO_2–WO_3 IO film was assigned to the higher surface area with improved charge transfer. By regulating the carbon contents, the optimum NiO@C realized faster coloration, higher CE and longer durability than the NiO film with lower carbon content, due to fast ion diffusion and higher electrical conductivity.[48] Other works employing hybrid materials also realized improved EC performance compared to the respective components, including MoO_3–$W_{0.71}Mo_{0.29}O_3$ film versus $W_{0.71}Mo_{0.29}O_3$ film,[49] $W_{0.71}Mo_{0.29}O_3$/PEDOT:PSS (polystyrene sulfonate) film versus $W_{0.71}Mo_{0.29}O_3$ and PEDOT:PSS film,[50] etc.

Amorphous EC Materials: Compared to crystalline counterparts, amorphous metal oxides (AMOs) have received increasing interests in electrochemical applications, due to the larger number of active sites, reduced length of ion diffusion, improved cycling stability with smaller volumetric change, and the fast kinetics enabled by the absence of grain boundary.[51–53] AMOs have shown improved cycling stability when applied as anode materials for lithium ion batteries (LIB) and sodium ion

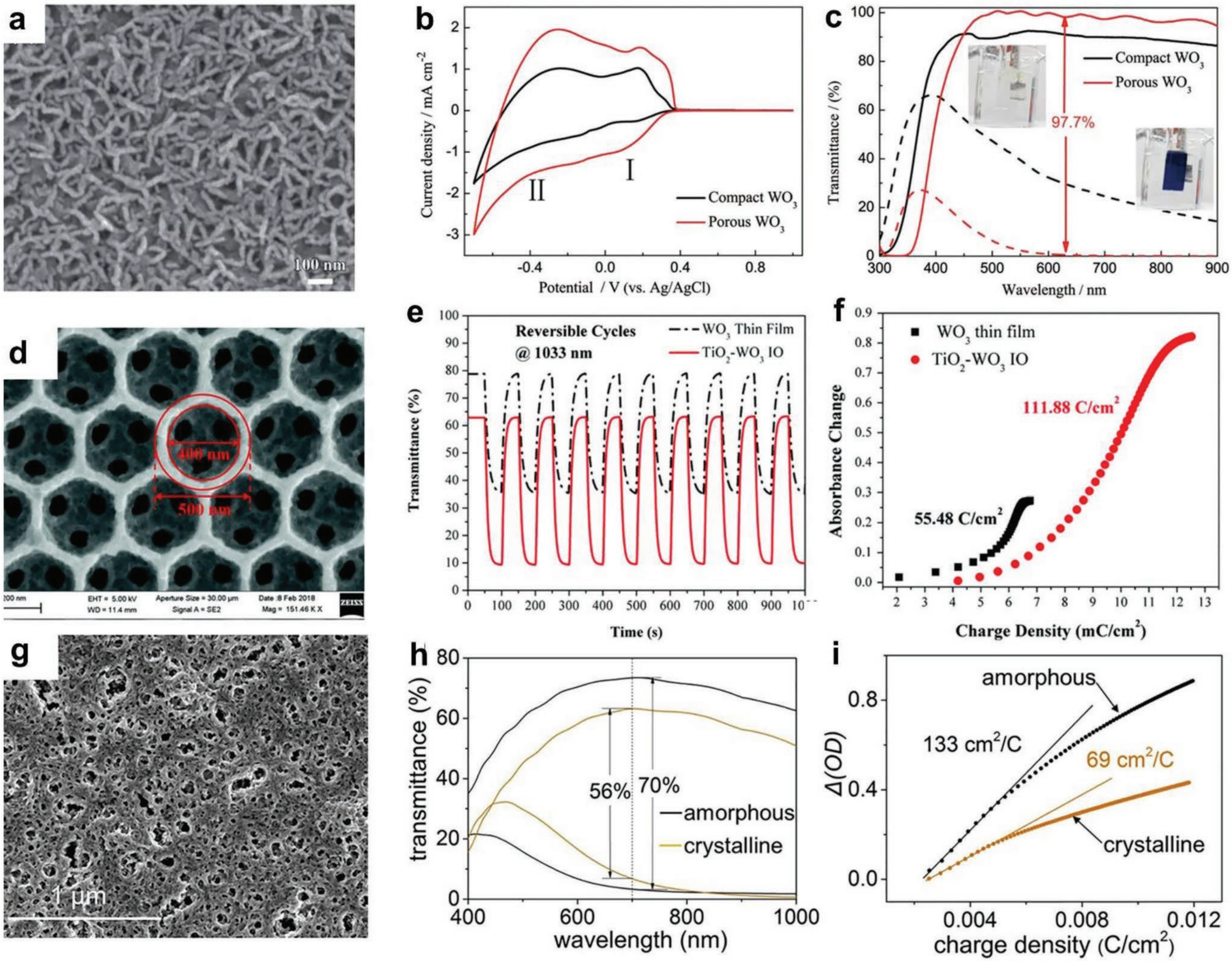

Figure 2. a) Scanning electron microscopy (SEM) of porous WO$_3$. b,c) cycling voltammograms (CV) and transmittance spectra at colored/bleached state of porous and compact WO$_3$. The insets in (c) show the photographs of porous WO$_3$ film at bleached and colored states. Reproduced with permission.[44] Copyright 2016, Royal Society of Chemistry. d) SEM of TiO$_2$–WO$_3$ IO composites, e) dynamic optical transmittance curves and the corresponding f) coloration efficiency of WO$_3$ thin film and TiO$_2$–WO$_3$ IO film. Reproduced with permission.[47] Copyright 2018, Royal Society of Chemistry. g) SEM image of a-WO$_3$ films. h) transmittance spectra and i) CE of amorphous and crystalline WO$_3$ film. Reproduced with permission.[52] Copyright 2018, Cell Press.

batteries (SIB).[51,54] Similar to LIB/SIB that involves ion intercalation/deintercalation, EC devices normally also function as a result of ion intercalation/deintercalation,[36,55] thus amorphous ECM are deemed as promising candidates to realize enhanced EC performance. For example, amorphous WO$_3$ (a-WO$_3$) obtained by rapid photodecomposition shows larger optical modulation (70%) and higher CE (133 cm^2 C^{-1}) than the crystalline WO$_3$ counterparts as shown in Figure 2g–i.[52] Improved cycling stability was also harvested by the a-WO$_3$ film. The superiority of a-WO$_3$ over crystalline counterpart was presumably explained by the higher atomic disorder and interstitial spacing available for amorphous films that facilitate the diffusion and storage of Li$^+$. This photodecomposition method is also applicable for the synthesis of other EC AMOs including V$_2$O$_5$, Nb$_2$O$_5$, and MoO$_3$. The higher hydrogen diffusion coefficient in a-WO$_3$ thin film than crystalline WO$_3$ films has been quantified.[56] Also, a cost effective method of acid-catalyzed condensation of polyniobate clusters at room temperature was employed to obtain amorphous NbO$_x$ thin film composed of 1D chain like NbO$_x$.[53] The amorphous NbO$_x$ shows significantly enhanced EC performance (CE = 29.5 cm^2 C^{-1}) than the 3D NbO$_x$ networks (CE = 15.2 cm^2 C^{-1}) obtained by conventional high-temperature thermal processing, which is related to the two orders of magnitude higher Li$^+$ diffusion coefficient in amorphous NbO$_x$ film.[53] Amorphous Nb$_2$O$_5$ film was also prepared by photoactivation and subsequent low temperature (150 °C) thermal annealing, which shows improved cycling stability (≈72% charge density retention after 1500 cycles) than the high temperature (300 °C) annealed Nb$_2$O$_5$ film (50% retention after 1500 cycles).[57]

Heteroatom Doping in EC: Doping of aliovalent atoms can often alter the electronic structures of parent metal oxide, offering intriguing optoelectronic properties, and in some cases, reducing particle and crystallite size and improving electronic conductivity as well as electrochemical durability.[55,58–61] Thus doping has been adopted as an effective strategy to improve the performance of ECM. Lee and co-workers reported that with Ti doping, small nanoparticles (NPs) were obtained as shown in **Figure 3**a.[58] Proper amount of Ti doping (WO_3–10Ti, Ti of 10 at%) results in higher contrast (67.6%) and higher CE (87.7 $cm^2\ C^{-1}$) as can be seen in Figure 3b,c, yet slower kinetics than those of the pure WO_3 due to the reduced proton diffusion coefficient. Fe doping of WO_3 was found to be effective in realizing faster kinetics (t_c = 7.2 s, t_b = 2.2 s) and higher CE (46.2 $cm^2\ C^{-1}$) than those of pure WO_3, due to the formation of mesoporous thin film with presence of O defects and increased electronic conductivity.[62] Similarly, Nb doping of WO_3 was conducive to improving the contrast (61.7%) and boosting the switching speed (t_c = 3.6 s, t_b = 2.1 s), which can be ascribed to the reduced crystallinity and increased O vacancies that enhanced the electronic conductivity.[63]

Ion Detrapping in EC: Long-term cycling stability is crucial to EC devices for practical applications, however, the cycling stability of EC device is often deteriorated by repeated intercalation/deintercalation of ions into the ECM, which may result in ions trapping that lead to the degradation of EC materials as well as EC devices.[64–67] Recently, there have been reports on ion detrapping that is able to resuscitate the EC materials by extracting the trapped ions, thus extending the cycling stability significantly. As shown in Figure 3d,e, after ion detrapping, the CV curves and optical modulation of the cycled a-WO_3 film can be restored.[64] The ion detrapping was realized by a galvanostatic method with extended duration. This long-term galvanostatic detrapping method is applicable for a-WO_3 after different number of cycles, with different deposition parameters, or in wider voltage ranges. However, deep trapped ions (Li_xWO_3, $x > 0.65$) are not effectively extracted using the same method. Similar concepts of ion detrapping were also attempted and found to be successful in rejuvenating the EC performance of MoO_3 films[68] and NiO films[69] by potentiostatic treatments and amorphous TiO_2 films by galvanostatic treatments.[70] This ion detrapping strategy seems to be universal in resuscitating the performance of cycled EC metal oxides, and is also applicable in other ion intercalation based devices for example rechargeable metal ion batteries.[70]

2.1.2. Organic Electrochromic Polymers

EC devices offering multiple colors are also highly desired for applications, especially for displays. Most of the inorganic metal oxides have limited color choices at their color states, with WO_3/MoO_3 as blue color, NiO as brown color, etc.[48,71,72] Nonetheless, polymer-based EC materials, with adjustable molecular structure, are able to offer various color options.[73]

Reynolds and co-workers reported that through Suzuki polycondensation, eletrochromic polymers (ECPs) composed of repeated units of propylenedioxythiophene (ProDOT) in

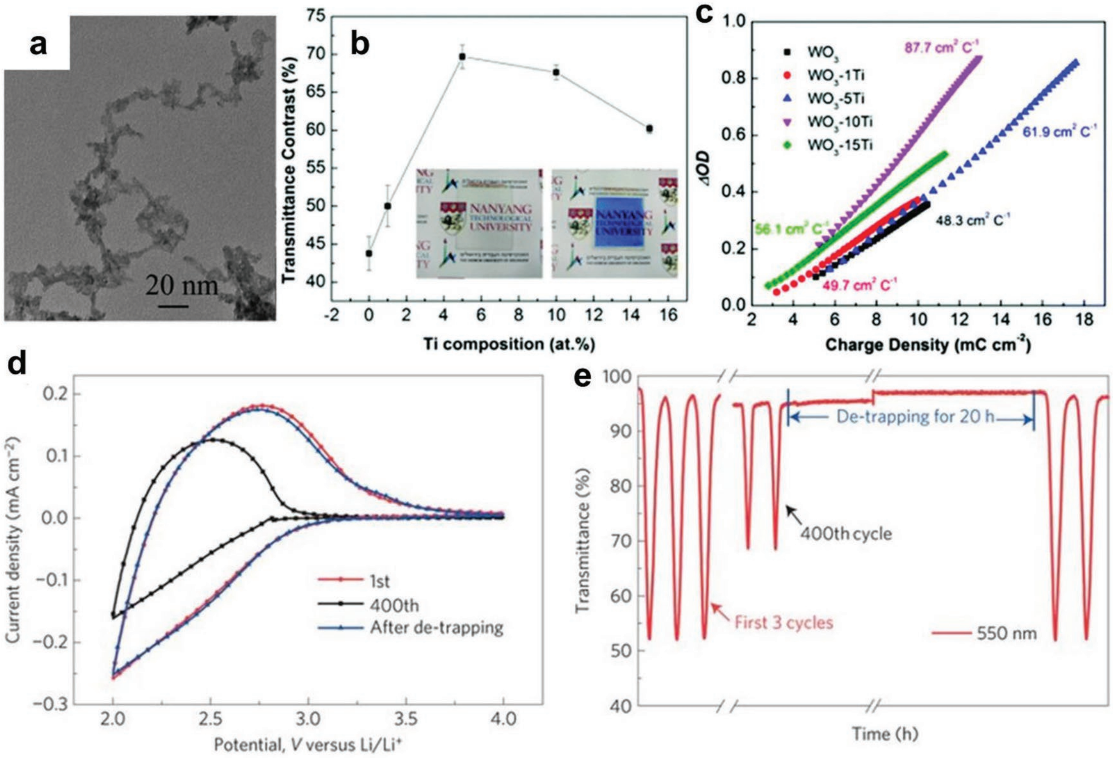

Figure 3. a) Transmission electron microscopy (TEM) image of WO_3–10Ti. b) transmittance contrast and c) CE of WO_3 doped with different Ti concentration. Reproduced with permission.[58] Copyright 2017, Royal Society of Chemistry. d) CV curves of a-WO_3 films at the 1st cycle, 400th cycle, and after detrapping. e) Optical transmittance of a-WO_3 at 550 nm after different numbers of cycles and after detrapping. Reproduced with permission.[64] Copyright 2015, Nature Publishing Group.

alternation with various arylenes can be obtained with different oxidation potentials.[73] Through subtle C–H *ortho* interactions from the arylene unit, these ECPs are able to maintain yellow neutral states with transmissive or near-transmissive oxidized states. Thereafter, by replacing the hydrogen atom on phenylene with electron-rich methoxy, ECPs copolymerized with DOTs have higher HOMO level, lower oxidation potential as well as improved redox stability and EC contrast.[74] Subsequently, as shown in **Figure 4**a,b, the same research group created red, yellow and orange ECPs at neutral states, by increasing interring strain on the polymer chains.[75] Strain modulation along the backbone of all donating DOT ECPs was also found effective in obtaining desired shades of blue and magenta colors at neutral states, while offering high EC contrast.[76] Hybridization of ECPs with different colors was able to create new color options, either by simply mixing different ECPs on the EC layer, printing patterns, or stacking EC devices fabricated with different EC materials. As displayed in Figure 4c,d, ECPs with cyan, magenta and yellow color states were selected, the mixed solution of which can produce other accessible colors displayed in Figure 4e.[77] Mixing these ECPs in EC layer with different ratios were also demonstrated to produce EC thin films with multiple colors at colored states, yet still transmissive at bleached states. Blending of different color

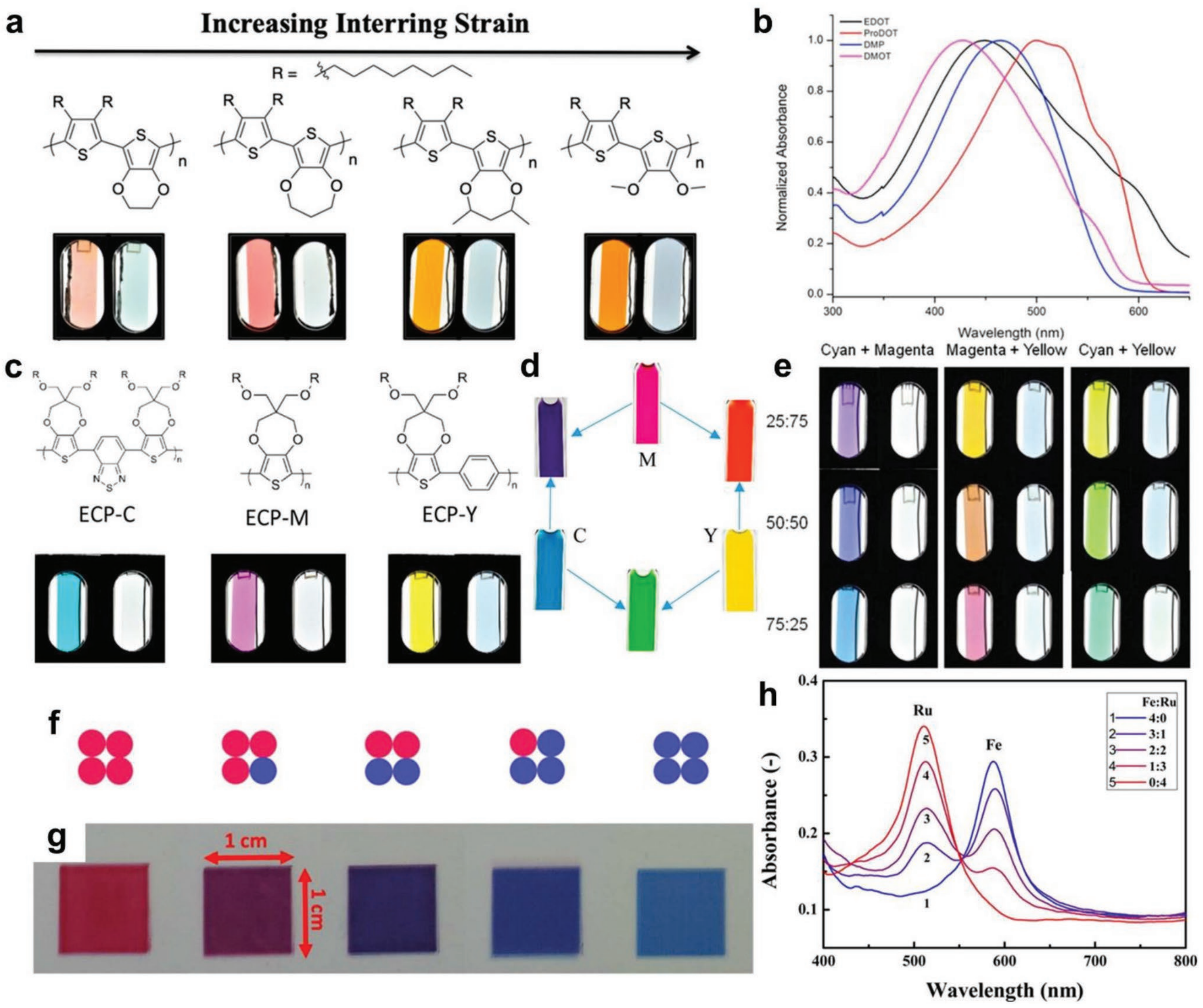

Figure 4. a) Different EC polymers (ECPs, from left to right: DAT–EDOT, DAT–ProDOT, DAT–DMP, and DAT–DMOT) of dioxythiophene comonomer with increasing interring strain and their respective photographs at colored and bleached states. b) Absorbance spectra of DAT–EDOT, DAT–ProDOT, DAT–DMP, and DAT–DMOT at neutral state on ITO glass in 0.5 M $TBAPF_6$/PC electrolyte, tested after 10 CV cycles. Reproduced with permission.[75] Copyright 2018, American Chemical Society. c) The repeat unit structures of the three CMY (cyan, magenta and yellow) representative ECPs selected, where R = 2-ethylhexyl and the photographs of their (left) colored and (right) bleached states. d) Solutions of ECPs-C, ECPs-M, and ECPs-Y (2 mg mL^{-1}) and 1:1 w/w ratios of these solutions. e) Photographs of the films of different ECPs mixed at various ratios at (left) colored and (right) bleached states. Reproduced with permission.[77] Copyright 2015, American Chemical Society. f) Color-mixing scheme and g) resultant EC material thin films with different mixing ratios of RuMEPE to FeMEPE. h) In situ UV–vis spectra of color-mixing MEPE thin films deposited on ITO glass. Reproduced with permission.[86] Copyright 2015, American Chemical Society.

ECPs was also able to produce brown or black to transmissive EC films.[78,79] On the other hand, patterning of the different color ECPs by inkjet printing is also able to produce EC films with a broad range of colors.[80] Alternatively, secondary mixing of two distinct ECPs films was also able to produce EC devices with various color states.[81]

2.1.3. Inorganic–Organic Hybrids: Metallo-Supramolecular Polymers

The above-mentioned EC materials are generally based on inorganic metal oxides or conjugated polymers with varied molecular structures. A new class of inorganic–organic hybrid materials, metallo-supramolecular polymers (MEPE) also show electrochromism based on the metal-to-ligand charge transfer and the intervalence charge transfer.[82] These MEPE are also able to offer multiple color choices by varying the metal ion center or the surrounding organic ligands. Higuchi and co-workers reported that coordination nanosheets synthesized by coordinating Fe^{2+} with different bis(2,2′-bipyridine) derivatives show blue to colorless and magenta to yellow electrochromism.[83] Also, introduction of 10% branching structure in the linear Os(II)-based MEPEs also alters the EC properties, increasing EC contrast, switching speed and CE of the hyperbranched polymer.[84] Hetero-MEPE prepared by complexation of Fe(II) with *cis*- or *trans*-conformational organo-Pt(II) ligands exhibited similar magenta-to-yellow electrochromism, yet the *trans*-polyFePt gave higher EC stability with faster switching kinetics due to the higher ionic conductivity and more amorphous nature.[85] The pH value was also found to affect the EC performance of Co(II)–bis-terpyridine MEPE in aqueous solution of KCl, stable deep black color can be obtained upon reduction of Co(II) center, yet increased pH resulted in higher transmittance across 400–800 nm wavelength at bleached states upon oxidation.[82] Blending of MEPE was used to create different colors. As shown in Figure 4f,g, by tuning the dot ratios of Ru(II)–MEPE and Fe(II)–MEPE, inkjet-printed films can have different colors between red to blue, corresponding to the varied absorption spectra as shown in Figure 4h.[86]

For a direct comparison, the EC performance (optical contrast $\Delta T\%$ measured at a certain wavelength, switching speed, coloration efficiency, cycling stability and the electrolyte used) of different EC materials discussed above are summarized and listed in **Table 1**. It can be seen that different EC materials have their respective advantages for EC applications. For example, generally WO_3 has relatively higher CE values than other inorganic metal oxides,[1] which may explain the commercial application of WO_3 in addition to the extensive academic publications.[35] Also, organic polymers and MEPE-based EC materials normally have faster switching speed than inorganic metal oxides, while offering color tunability at the same time, making them candidates for electronic displays.[35] However, how to manifest the advantages of respective EC materials

Table 1. Electrochromic performance of various EC materials discussed above.

EC materials		ΔT % [@ nm]	Switching speed(s)	CE [cm^2 C^{-1}]	Cycling	Electrolyte	Ref.
Inorganic metal oxides	WO_3	97.7 (633)	6, 2.7	118.3	300	0.5 M H_2SO_4	[44]
		70 (700)	12, 5	133	1000	1 M $LiClO_4$ in PC	[52]
		74.7 (630)	7.28, 2.64	75.35	250	1 M H_2SO_4	[40]
		55.9 (633)	1.7, 1.0	80.2		1 M H_2SO_4	[87]
		75.6 (633)	2.4, 1.2	79.7		0.5 M H_2SO_4	[41]
	$W_{18}O_{49}$	73 (633)	8.6, 7.0	97.9	300	1 M H_2SO_4	[42]
	MoO_3	≈36 (500)		57		1 M $LiClO_4$ in PC	[52]
		63 (1500)				1 M $LiClO_4$ in PC	[72]
	V_2O_5	≈25 (450)		36		1 M $LiClO_4$ in PC	[52]
	Nb_2O_5	≈33 (500)		22		1 M $LiClO_4$ in PC	[52]
	NbO_x	≈40 (500)		29.5	1000	0.1 M LiTFSI in TEG	[53]
	NiO	63.6 (550)	11.5, 9.5	42.8	5000	1 M KOH	[88]
		60.6 (550)	0.46, 0.25	113.5	20 000	1 M KOH	[48]
Organic polymers	$PProDOT_2–Ph(OMe)_2$	70 (500)	1.17, 0.71		100	0.5 M $TBAPF_6$ in PC	[74]
	DAT–DMP	65 (466)	<5 s		1000	0.5 M $TBAPF_6$ in PC	[75]
	$ProDOT_2–EDOT_2$	70 (608)	<1 s			0.5 M $TBAPF_6$ in PC	[76]
	$AcDOT_2–ProDOT$	73 (543)	<1 s			0.5 M $TBAPF_6$ in PC	[76]
MEPE	polyCo	74.3 (550)	31.6, 21.5		100	0.1 M KCl (pH = 13)	[82]
	NBP1	62 (590)	0.48, 0.57		1500	0.1 M $LiClO_4$ in CH_3CN	[83]
	NBP2	57 (568)	0.50, 0.54		1500	0.1 M $LiClO_4$ in CH_3CN	[83]
	polyOs $L1_{90\%}L2_{10\%}$	59.4 (508.9)	0.41, 0.54	467.5	200	0.1 M $LiClO_4$ in CH_3CN	[84]

Note: The performance of EC materials listed in this table is based on single electrode testing. LC-based materials are not included. PC: propylene carbonate; TEG: tetraglyme; $TBAPF_6$: tetrabutylammonium hexafluorophosphate.

while mitigating the shortcomings for practical and large-scale applications still remains a challenge.

2.2. Liquid Crystal (LC)-Based Electric-Driven Smart Windows

LC-based electric-driven smart windows are already commercialized, and some research can be found in literatures, e.g. polymer-dispersed liquid crystal (PDLC), polymer-stabilized liquid crystal (PSLC), cholesteric liquid crystal (ChLC) cells, etc.[89–91] Unlike typical EC devices that alter the transmittance/absorption based on electrochemical processes, LC-based devices are normally switching between the opaque and transparent state through light scattering/absorption by electrically controlled alignment of liquid crystals.[90] The voltage needed to drive an LC device is normally in the order of tens of volts, without optical memory or retention effect. In contrast, only <3 V is required for typical EC devices to induce large optical modulation that can last for a few hours when power is off.[92]

A PDLC cell is able to switch between opaque (off) and clear (on) state. Dichroic dye doping can increase chromism of PDLC, in order to avoid stain contamination associated with dichroic dye doping, the dichroic dye was encapsulated by core–shell microcapsules through membrane emulsification and interfacial polymerization, forming monodispersed microcapsules based on LC crystals/dichroic dye cores and polyurethane/polyurea shells.[93] A PDLC device utilizing these microcapsules exhibited a high contrast ratio of >120 at 600 nm with a maximal transmittance of 90% at 700 nm. A flexible PDLC cell with heat shielding capability was demonstrated by employing $TiO_2/Ag(Cu)/TiO_2$ (TCAT) on PET as the electrodes instead of ITO.[94] At on state, a superior heat-shielding effect was realized in the TCAT devices, with 4.6 °C temperature decrease compared to ITO device. Furthermore, it was shown that PSLC devices with mixture doping of non-dichroic dye (LT1641B) and dichroic dye (RL002) showed high transparency at off state with increased contrast and faster switching time.[95]

Dye doping in ChLC cell was also employed toward smart windows applications.[96] By doping ChLC cell with a push-pull azo dye molecules, *trans–cis* photoisomerization caused by UV light will induce cholesteric-isotropic phase transition. The same cell can also be switched with application of electric field. The initial opaque cell with specular transmittance 18.1% and haze of 72.2% can be tuned to 81.5% and 2.5%, respectively, upon application of 40 V voltage. Unlike the as-discussed ChLC cells that are normally opaque at off state, a normally transparent ChLC cell can also be created based on field-induced dielectric instability of ChLC.[97]

Other than doping LCs with dye, inclusion of ionic species was also conducted.[98] By doping the LCs (with negative dielectric anisotropy)/dichroic dye mixture with an ionic material TBAB (tetra-*n*-butylammonium bromide), both strong light absorbance and light scattering were realized at opaque state due to the turbulence caused by the rotation of ions under an electric field. At opaque state, the ion-doped LC cell exhibited a lower specular transmittance than ChLC cell and lower total transmittance of ≈20% than the PSLC cell (≈30%).

It was shown that polymer-dispersed ChLC (PSChLC) cell can be used as electrically tunable infrared reflectors.[99] At low voltage $<2.1\ V\ \mu m^{-1}$, the PSChLC cell is transparent to visible light and reflective to IR, with increased voltage to $5.4\ V\ \mu m^{-1}$, visible light is scattered and IR reflection remains almost unchanged. When the voltage was further increased to $8.6\ V\ \mu m^{-1}$, the cell is transparent both to visible light and IR. An electrically tunable IR reflector with adjustable bandwidth, with inclusion of long ethylene glycol crosslinker in a PSChLC cell was also demonstrated.[100]

2.3. Multifunctional Electrochromic Devices

There has been increasing attention in multifunctional devices that integrate different mechanisms for future applications. As for EC devices, reversible optical modulation is the main function. Immense efforts have been devoted to integrate multifunctionalities into EC devices, which are able to store and release energy, actuate, or self-powered by harvesting mechanical and solar energy, and so on.

2.3.1. Electrochromics with Energy Storage Devices

EC devices operate on the basis of ion insertion/extraction, resembling the electrochemical processes in pseudocapacitors or batteries.[36] Thus EC devices intrinsically have the capability to store energy, making them bifunctional EC-energy storage (EES) devices. The concept of bifunctional EC-energy storage has been prototyped in literatures rece ntly.[41,87,101–106] As displayed in **Figure 5**a–d, a bifunctional EES device with configuration of $Ta\text{-}TiO_2//1\ \text{M}\ LiClO_4$ in PC//NiO was assembled with ITO as the TCE layers, which shows dual-band electrochromism in both visible and near-infrared (NIR) wavelength, offering "cool" state that blocks most of the IR heat yet maintaining high visible transparency (65–70% transmittance).[17] Simultaneously, the bifunctional EES device is able to release the energy stored within, giving discharge capacity of $466.5\ mAh\ m^{-2}$ at a current density of $150\ mA\ m^{-2}$. For demonstration purpose, a fully charged EES device was able to light up a red LED, showing energy storage capability of the EES device. Another example is the WO_3 electrodeposited onto the flexible PEDOT:PSS protected Ag grid on polyethylene terephthalate (PET) films, which is able to reversibly change color along with the galvanostatic charge/discharge process as shown in Figure 5e,f.[107] The specific capacitance of WO_3 on Ag grid/PEDOT:PSS is measured to be 221.1 and $148.6\ F\ g^{-1}$ in $0.5\ \text{M}\ H_2SO_4$ aqueous solution, at current density of 1 and $10\ A\ g^{-1}$, respectively. Aside from monovalent H^+ and Li^+ based electrolyte, this concept of bifunctional EES was also realized in multivalent Zn^{2+}-based electrolyte as shown in Figure 5g,h.[108] Elezzabi and co-workers reported that Ti-substituted $W_{0.71}Mo_{0.29}O_3$ (MTWO) electrode is able to change color in the visible range in $ZnSO_4$ aqueous electrolyte with optical modulation of 76% at 632.8 nm, which also has areal capacity of $260\ mAh\ cm^{-2}$. A self-coloration phenomenon was observed when the MTWO cathode and the Zn anode was connected,

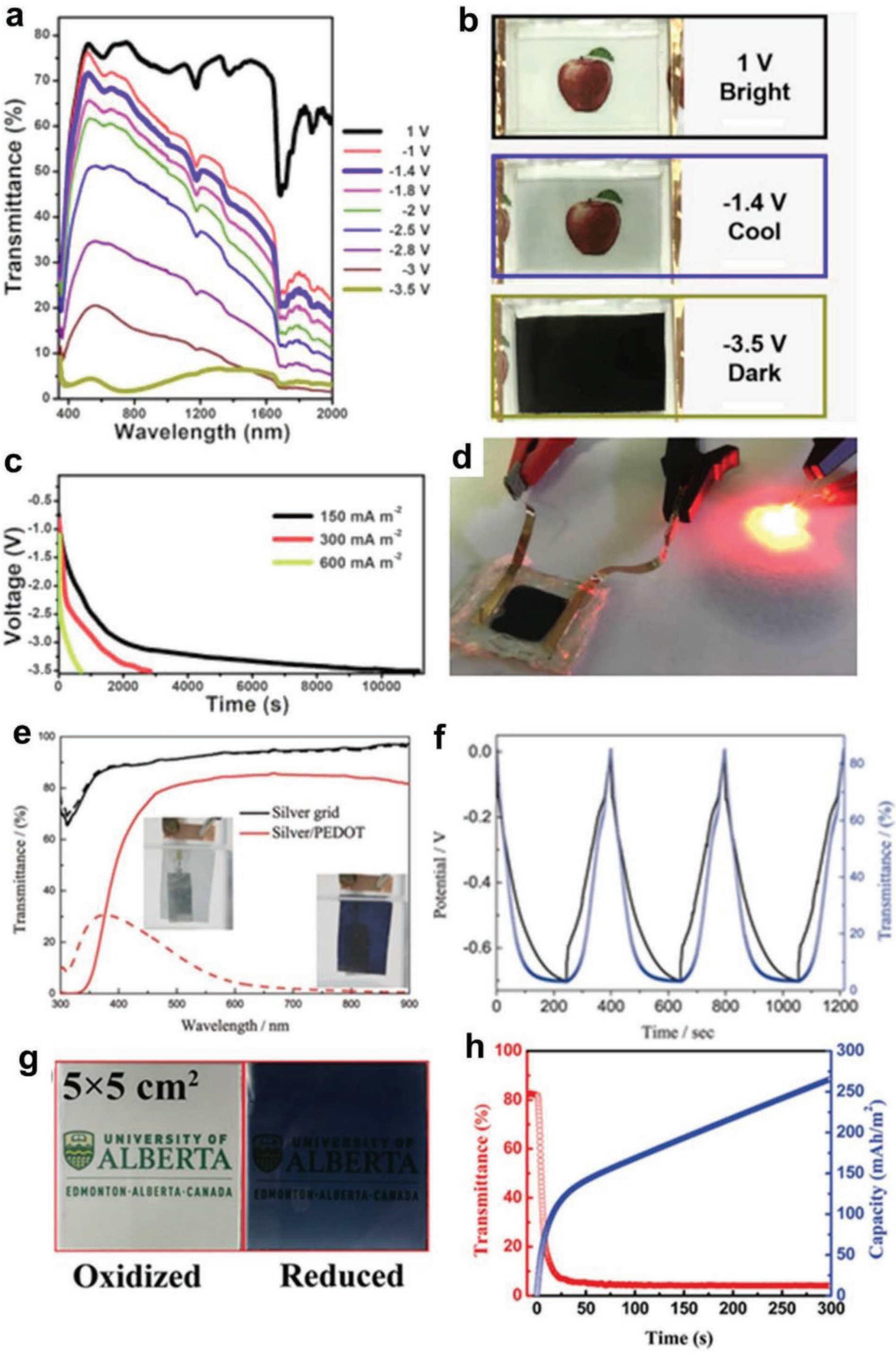

Figure 5. a) Optical transmittance spectra and b) digital photos of the EES device between 1 and –3.5 V. Scale bar is 1 mm. c) Galvanostatic discharging curves of the EES device. d) Optical image of an EES device (in the dark state) powering a red LED. Reproduced with permission.[17] Copyright 2019, Cell Press. e) Transmittance spectra of WO_3/Ag grid and WO_3/Ag grid/PEDOT:PSS hybrid films in the colored (–0.7 V) and bleached (0.1 V) states. f) Galvanostatic charge–discharge curves at 1 A g^{-1} and corresponding transmittance change at 633 nm of the hybrid film. Reproduced with permission.[107] Copyright 2016, John Wiley & Sons. g) Photographs of a 5 × 5 cm^2 MTWO cathode at bleached and colored state. h) In situ self-coloring process of MTWO cathode. Reproduced with permission.[108] Copyright 2019, John Wiley & Sons.

due to the intercalation of Zn^{2+} into MTWO caused by the different redox potential between MTWO versus Zn. A full device composed of MTWO//$ZnSO_4$//Zn was also fabricated, which is able to change color (with contrast of 62%) with areal capacity of 150 mAh m^{-2}. This full cell EES device was demonstrated to light up an LED for more than 40 min.[108]

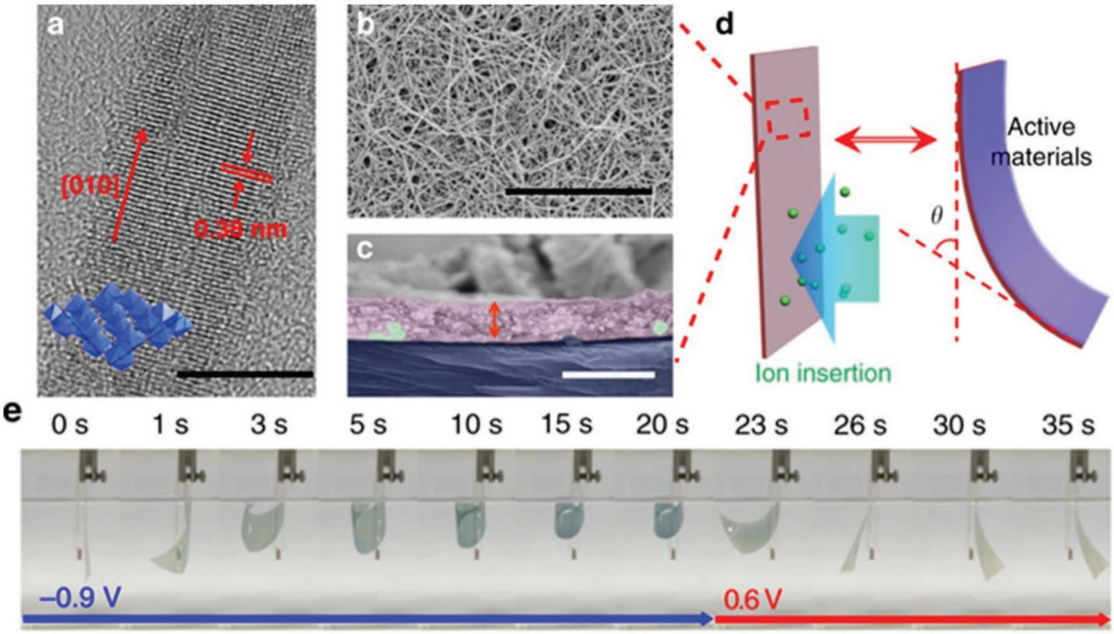

Figure 6. a) High-resolution TEM image of a single $W_{18}O_{49}$ NW (scale bar: 10 nm); SEM images of b) surface (scale bar: 3 μm) and c) cross-section (scale bar: 500 nm) of the dual-responsive film. d) Schematic illustration of measurement criteria of electrode deformation angles. e) Digital photographs of synchronous EC/actuating processes of the dual-responsive film. Reproduced with permission.[109] Copyright 2018, Nature Publishing Group.

2.3.2. Electrochromics with Actuator

Resembling chameleons that reversibly change skin color, EC devices can be applied for camouflage due to their adjustable optical properties. However, other camouflage animals including octopus, cuttlefish and Andean rain frog are able to change their texture/posture aside from color changing, increasing the survival chance.[109] Actuators are able to generate motions and forces/torques upon various stimulus of light, electricity, heat, etc., which can be applied in a lot of fields including soft robotics, adaptive camouflage, etc.[109,110] Thus EC-actuator bifunctional devices simulating those camouflage animals are of great interests. As displayed in **Figure 6**, $W_{18}O_{49}$ NWs with high aspect ratios (diameter: ≈20 nm; length: ≈12 μm) were sprayed onto Ag NWs/PEDOT: PSS films on PET, forming a dual-responsive film that is able to change color and bend upon application of bias.[109] This bifunctional EC/actuating film has both excellent EC performance (t_c = 4.1 s, t_b = 2.9 s; contrast of 26.6% (at –0.9 V); CE = 119.2 $cm^2\ C^{-1}$; cycling stability of >90% after 100 cycles) and actuating performance, with maximum bending angle of 238° within 5 s. Results of control experiments confirmed that the actuation was caused by the Li^+ intercalation-induced lattice contraction in $W_{18}O_{49}$ NWs ($d_{(010)}$ from 0.374 to 0.368 nm), excluding possible actuation from Ag NWs/PEDOT:PSS substrates nor from non-Faradic ion absorption in $W_{18}O_{49}$ NWs. A symmetric air-working ionic polymer metal composite (IPMC) actuator was assembled based on two layers of $W_{18}O_{49}$ NWs/carbon nanotube (CNT) films sandwiching the polymer gel electrolyte (1 M $LiClO_4$ in propylene carbonate, with 17 wt% poly(methyl methacrylate) and acetone). The IPMC actuator realized maximum actuating displacement of ± 1.83 mm within 1.4 s at ± 1.8 V. The outstanding performance of the bifunctional EC/actuator and the fast response of the air-working IPMC actuator are attributed to the formation of interconnecting networks with large surface area and the high electronic conductivity of the Ag NWs/PEDOT:PSS and CNT substrates.

2.3.3. Electrochromics with Triboelectric Nanogenerator

Triboelectric nanogenerators (TENGs) are able to generate electricity from different kinds of mechanical impulse based on triboelectrification effect and electrostatic induction, with merits of high output voltage, high power density, high conversion efficiency and low cost.[111–113] Thus, TENG is suitable power source for other electronic devices, especially for self-powered systems.[114–116] For example Lee and co-workers reported a self-powered fast charging supercapacitor integrating electrical double layer capacitor with TENG[117] and a self-powered physiological sensor that harvests energy from human motions while simultaneously monitoring physiological signals.[115] Similarly, the energy harvested by TENG can also be used to power an EC device. As prototyped in **Figure 7**a, Wang and co-workers reported a TENG (wind powered) that has optimum power density of 130 mW m^{-2}.[116] By integrating the TENG with an EC device composed of Prussian blue NPs//$LiClO_4$//$Zn_3[Fe(CN)_6]_2$ nanocubes, the absorption spectra of the EC device is clearly altered along with extended duration till 5000 s. From the transmittance spectra shown in Figure 7b,c, it is clearly seen that the original EC device at bleached state was charged to blue state, giving optical contrast of 32.4% (at 695 nm), which is comparable to the contrast realized by conventional potentiostat. These results clearly demonstrate the possibility of realizing a self-powered EC bifunctional device, yet the color switching time still needs to be shortened.

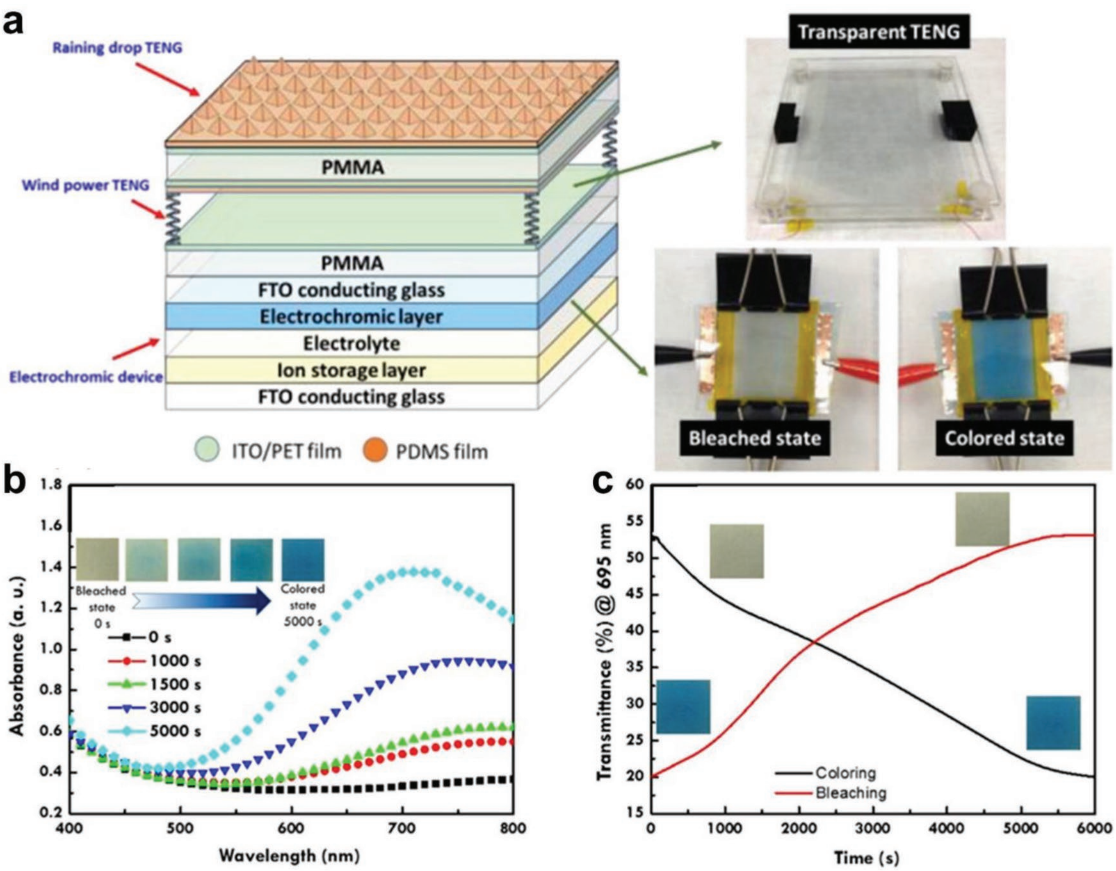

Figure 7. a) Schematic diagram of the self-powered smart window integrated with a raindrop-TENG, a wind-powered-TENG, and an EC device, and the photographs of TENG and EC device at bleached and colored states. b) UV absorption spectra of the self-powered EC device obtained at different durations. Insets are EC device at different duration times with changing colors. c) Transmittance change of the self-powered smart window in response to various duration times for bleaching and coloring. Reproduced with permission.[116] Copyright 2015, American Chemical Society.

2.3.4. Electrochromics with Solar Cells

Unlike TENG that harvest mechanical energy, solar cells are able to convert solar energy into electricity. As schemed in **Figure 8**a, a perovskite solar cell harvesting solar energy is able to charge the EES device, which in turn can act as a power source to power up an LED, showcasing the multifunctionalities including energy harvesting, energy storage, electrochromism and energy reutilization.[118] The photograph of the solar cell and EES devices can be seen in Figure 8b. The perovskite solar cell is able to produce voltage output of ≈0.89 V with maximum current density output of ≈18 mA cm^{-2}, while the EES device is able to offer optical modulation of 43% at 750 nm and 62% at 2000 nm as depicted in Figure 8c, with high CE of 135.5 cm^2 C^{-1} and fast switching kinetics ($t_c = 2.5$ s, $t_b = 2.6$ s). The energy storage capability of the EES device was also quantified, with specific capacities of 75 and 52 mAh g^{-1} at current densities of 1 and 10 A g^{-1}, respectively. Variation of optical transmittance at 2000 nm of the EES device along with the charge/discharge process is presented in Figure 8d. The energy harvested by a serial of 8 perovskite solar cells was utilized to power 2 EES devices, which are able to light up two red LEDs for a certain duration. Another example is the photoresponsive EC supercapacitor.[119] The EC layer was composed of WO_3 NPs/Ag NWs/reduced graphene oxide (rGO), which were sprayed coated in sequence onto cellulose nanofiber paper substrate. This electrode is able to deliver contrast of 41% at 600 nm with CE of 64.8 cm^2 C^{-1}, while the specific capacity of the same was calculated to be 406 F g^{-1} at current density of 1 A g^{-1}. Mechanical deformability was also incorporated in a symmetric EES device, which is able to sustain 99.1% of its original capacitance and 97.6% of its original transmittance after 100 repeated bending cycles. A solar cell connected to the EES device is able to reduce the transmittance (from 83% to 71%) of the EES device with increased Xenon lamp irradiation intensity, while an EES device at colored state (charged by the solar cell) is able to color another EES device. This photoresponsive EC supercapacitor clearly prototyped the concept of self-powered device that harvests solar energy to induce EC phenomenon, which in turn acts as a power source to charge another EC device, getting rid of any external power sources.

2.3.5. Other Multifunctional Electrochromic Devices

Aside from the above-mentioned multifunctional EC devices that store energy, actuation and self-powered, other multifunctional EC devices were also demonstrated in literature. Most of the above-mentioned multifunctional EC devices are based on

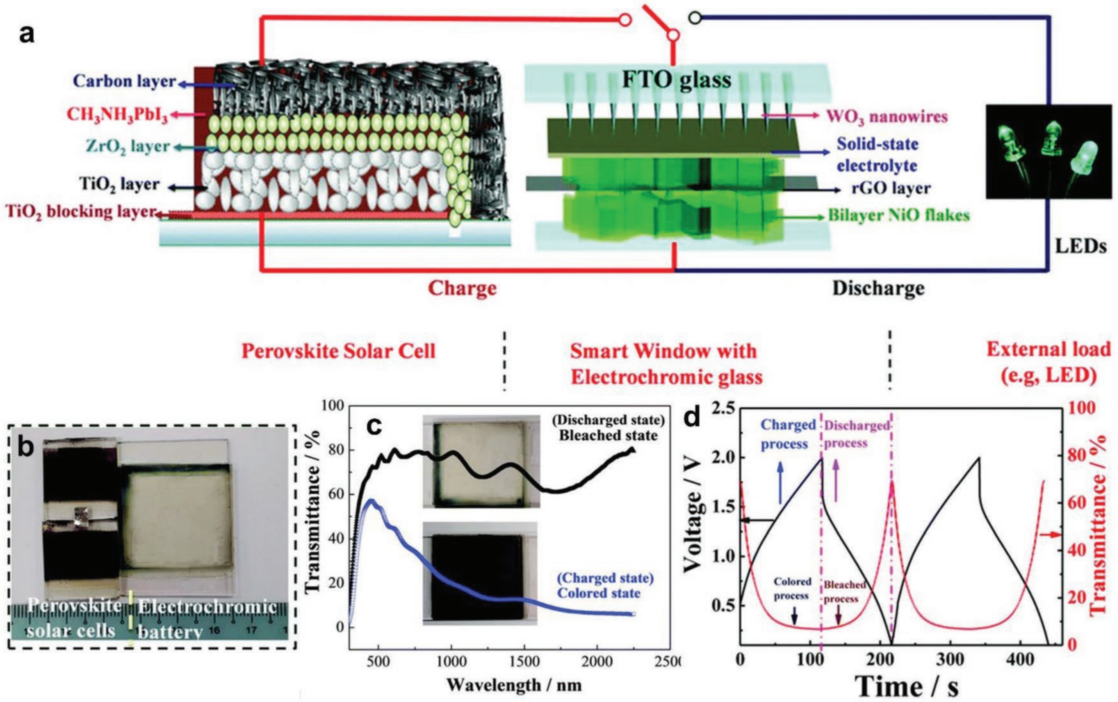

Figure 8. a) Schematics of the structure and working principle of the combined devices. Perovskite solar cell (left); solid-sate EC battery (middle); external load (right). b) Photographs of perovskite solar cell and solid-state EC battery. c) Transmittance spectra of the solid-state EC device, insets are the EC device at bleached and colored states. d) Charge/discharge profiles at 5 A g^{-1} within in situ transmittance spectra measured at 2000 nm. Reproduced with permission.[118] Copyright 2016, Royal Society of Chemistry.

optical modulation in transmittance/absorption mode, whereby reflective EC mirror (REM) device are also one of the trend for EC applications based on modulation in reflectance.[120] Different from conventional ion insertion/extraction enabled EC device, the electrochemical mechanism of REM devices are based on the reversible electrodeposition/dissolution of metals, e.g., Ag, Bi, Al, Pb, Ni, Cu, etc.[120] Lee and co-workers reported an REM device based on Cu electroplating/dissolution, offering transparent, blue and mirror states, realizing reflectance contrast of 54.8% at 660 nm with memory effect of ≈30 min, yet the cycling stability of ≈200 cycles needs to be extended.[120] Xia and co-workers reported an EC-photothermal sterile window by coupling Au nanorods with WO_3 honeycomb into the EC layer, which realizes CE of 88.1 cm^2 C^{-1}.[121] The same electrode also shows photothermal and anti-bacterial effect, which at colored state is able to increase the temperature of a 3 mL phosphate buffered solution by 24.5 °C under irradiation of a 915 nm laser for 300 s, and simultaneously reduce the survival rate of E. coli bacterium to 0%. This electrode shows multifunctionalities of EC, photothermal and bactericidal effects. Wang and co-workers reported a redox flow EC window without the presence of TCE layers, which is able to reversibly change color based on the interaction between the triphenylamine derivative/TiO_2 EC layer and I_3^-/I^- redox pair in the aqueous electrolyte.[122] The realizable contrast can be ≈60% at 730 nm.

2.4. Brief Conclusion

In a nutshell, strategies reported in recent years to improve the performance of inorganic ECM and organic ECP materials, as well as LC-based materials have been summarized and discussed, inspiring strategical design of future high-performance EC materials. These novel EC materials are the basis of developing high performance and also mechanically deformable (e.g., flexible, stretchable, self-healable) EC devices, paving the way for large-scale commercialization of EC technology (e.g., energy-efficient glazing in green buildings, soft electronic displays, etc.) in the future. Multifunctional EC devices that act as energy storage devices, actuators, self-powered by harvesting mechanical and solar energies have been showcased, opening new application fields that adopt the merits of EC technology. However, efforts are still needed to have deeper understanding of improved EC performance by different strategies while the cost-effectiveness, scalability and reliability are also to be considered. For EC devices integrating multifunctionalities, strategies to improve the efficiency, manufacturability and scalability remains the question to be answered for future advancement of EC applications.

3. Thermochromic Smart Windows

The smart window based on thermochormics can change its transparency according to the temperature.[4,123] This mechanism is commonly considered to be a passive way for light modulation, as such a smart window may modulate the light adaptively in response to the dynamic environmental temperature.[5] The mechanism makes such window a good candidate for the building energy economization, where the indoor solar irradiation is more transmitted in cold day than in hot days automatically without extra energy input.[4,124] Another advantage of the TC smart window is that it is purely materials-driven and does not require the additional control system, while is an essential part of the EC and the MC smart windows.

The thermal-responsive material plays a critical role in TC smart windows. These materials have undergone rapid development in the last five years. To date, several kinds of thermal-responsive materials have been successfully applied, including the vanadium dioxide (VO_2), hydrogels, ionic liquids, liquid crystals, and perovskites.[5] These materials were explored with different ways to change the transmittance. The VO_2-based nanocrystals (NCs), ionic liquids, and perovskites tune the absorbance intensity or shifting the absorbance band through the crystal phase transition. The hydrogels and liquid crystals rely on reflecting or scattering the incident light due to the phase separation and crystal orientation transition respectively.[125,126] Moreover, there is an increasing research interest to integrate the thermochormics with other functionalities, such as the energy conversion, electrothermal-based active control, or electro/mechanochromics, leading to better optical modulation and energy utilization. These integration methods promise the functional smart windows to match the diverse requirements in the extensive practical circumstances.

3.1. Strategies for Thermochromic Windows

3.1.1. VO_2-Based Nanocrystals

The VO_2 is the most-studied material for TC smart windows. It undergoes a reversible crystal phase transition from the monoclinic to the tetragonal phases at ≈68 °C, the critical transition temperature of VO_2 (τ_c) (**Figure 9**a),[127] resulting in an increasing absorbance in the NIR spectrum and negligible

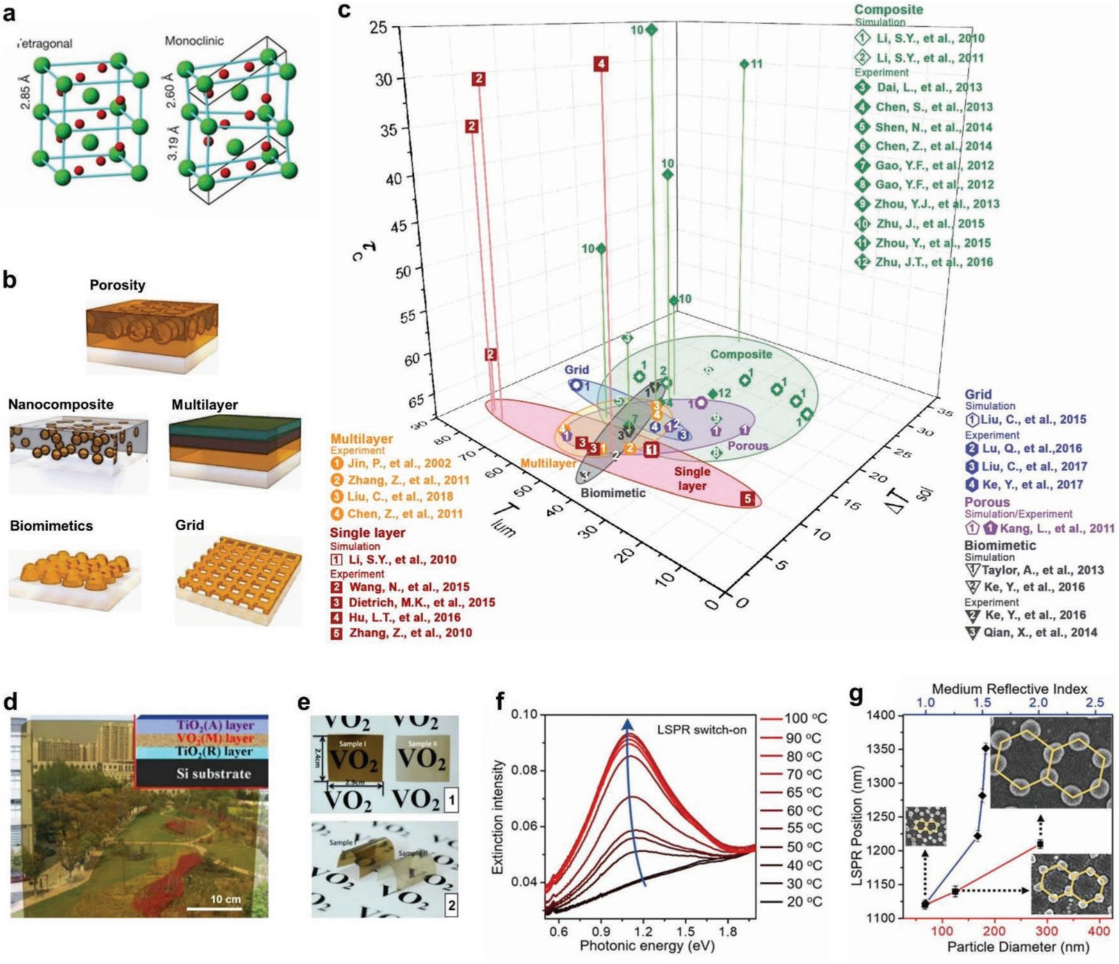

Figure 9. a) Schematic crystal structures of tetragonal and monoclinic VO_2. Reproduced with permission.[127] Copyright 2014, Nature Publishing Group. b) Schematic of the methods to promote the performance of VO_2-based smart windows. c) Summary of the performance of VO_2-based TC windows, including ΔT_{sol}, T_{lum}, and τ_c. The data points of multilayer,[166–169] single layer,[146,148,170–172] composite,[132,133,135,136,145,148,149,151,173–176] grid,[142,150,177,178] porous,[130] and biomimetic[139,140,179] methods are summarized from literatures. Reproduced with permission.[4] Copyright 2018, Elsevier. d) Prepared TC windows based on the TiO_2-VO_2-TiO_2 multilayer. Reproduced with permission.[128] Copyright 2015, Elsevier. e) Prepared TC foils based on VO_2 NCs in the poly matrix. Reproduced with permission.[132] Copyright 2012, Royal Society of Chemistry. f) The temperature-dependent extinction spectra of VO_2 NP arrays. g) Analysis of the LSPR position related to the particle diameter and the medium reflective index. Insets show the SEM images of VO_2 NPs with a periodicity of 160, 490, and 830 nm (yellow hexagons). Reproduced with permission.[150] Copyright 2017, American Chemical Society.

changes in the visible and the UV spectrum. The invertible challenge of VO_2 based thermochromic window is to reduce τ_c, enhance luminous transmission (T_{lum}) and solar modulation (ΔT_{sol}) simultaneously. So far, a number of methods have been developed to tackle this issue of planar VO_2 films, including dopants,[4] the introduction of porosity or multilayer structures,[128–131] the incorporation of VO_2 NPs in nanocomposites,[132–138] and the preparation of biomimetic or griding structures (Figure 9b).[139–142] The performance is summarized by the previous report and reprinted in Figure 9c.[4] The group of Jin has produced the large-scale multilayered VO_2 films (Figure 9d) and demonstrated several advantages of the design, including the self-cleaning functionality, the enhanced durability, and the antireflection for the promoted T_{lum} and ΔT_{sol}.[128,129] Flexible TC films are achieved by Gao et al. by dispersing the VO_2-based NCs into the polyurethane matrix.[132] The polymer matrix can protect the VO_2 from oxidation, and the prepared foils are flexible (Figure 9e). The group of Gao has also prepared porous VO_2 films using a removable polymer addictive and calculated their ΔT_{sol} and T_{lum} in functions of the film thickness and the porosity as the air pores can enhance the ΔT_{sol} by decreasing the optical constants.[130] The group of Long prepared the bio-inspired VO_2 films, demonstrating the antireflection structure can enhance both ΔT_{sol} and T_{lum}.[139] They also demonstrated the butterfly-inspired photonic crystal structures can modulate the intrinsic yellow-brown color of VO_2.[140] Significant research interests have been put on the doping effect, which is demonstrated to effectively lower the τ_c of pristine VO_2 and increase the T_{lum}.[4,143–145] For example, the introduction of the tungsten (W) dopant has been proved to lower the τ_c of VO_2 by ≈20 °C at%$^{-1}$.[146] The magnesium (Mg) dopant can promote the T_{lum} by widening the bandgap of VO_2.[146,147] Though progresses achieved, precisely controlled synthesis of high-quality VO_2 NCs are relatively challenged especially with structural features less than 100 nm.[4]

Nanocomposite based on the VO_2 NCs in transparent matrixes is a very efficient way. The quality of VO_2 NCs plays a significant role in the method. The group of Granqvist simulated the VO_2 NCs with ellipsoids,[148] spheres,[148] and core–shell structures in a transparent matrix.[149] They found both the ΔT_{sol} and T_{lum} can be enhanced through the method. One of the advantages of nanocomposite is the plasmonic-enhanced ΔT_{sol},[150–152] presenting as the temperature-dependent localized surface plasmon resonance (LSPR) that can shift the extinction peak position to the spectrum with the denser solar energy (Figure 9f). The LSPR was reported to shift according to the size of VO_2 NPs and medium reflective index (Figure 9g).[150] The effects of dopants to tune the τ_c, ΔT_{sol}, and T_{lum} are summarized in the latest review.[4] So far, a number of preparation methods have been developed for VO_2 NCs, such as chemical/physical vapor deposition (CVD/PVD),[153,154] pulsed laser deposition (PLD),[155,156] molecular beam epitaxy,[157] hydrothermal method,[158] and so on. Chen et al. prepared fine crystalline VO_2 NPs with an average diameter down to ≈30–40 nm and a relatively broad size distribution through the hydrothermal method.[133] The group of Li has successfully prepared ≈60–80 nm VO_2 NPs with a narrow size distribution through a hydrothermal method and a subsequent annealing treatment.[137,159] Besides NPs, VO_2 NCs have been achieved with a variety of different morphologies, including nanobeams (NBs),[160,161] 2D patterned arrays,[131,150,162] 3D nano/micronetworks,[163] and so on. The NB structure is one of the most common morphologies of VO_2 due to its preferred growth direction along the C_R axis. Preparation methods via, for examples, vapor deposition and hydrothermal synthesis are widely reported to successfully produce the VO_2 NBs.[151,161,164] Besides the ΔT_{sol} and T_{lum}, to reduce the τ_c is important.[144,145,165] More details of the theoretical calculation and experimental strategies can be found in the latest review.[4]

3.1.2. Ionic Liquid

The exploration of alternative materials beyond VO_2 has attracted increasing research interest. The group of Jin has pioneered the application of thermal-responsive ionic liquids to TC windows.[176] They have prepared a nickel–chlorine-based ionic liquid complexes by dissolving the di-(1-butyl-3-methylimidazolium)$[bmim]_2NiCl_4$ in the 1-(3-hydroxyethyl)-3-methylimidazolium tetrafluoroboride ($C_2OHmimBF_4$). In the complex, the octahedral $[NiCl_{6-x}(C_2OHmomBF_4)]^{x-4}$ undergoes a reversible ligand exchange process to the $C_2OHmim\ BF_4$ under elevated temperature (**Figure 10**a). The TC foil based on such complex is colorless at 20 °C while display a distinguish blue color at 80 °C (Figure 10b) due to the strongly enhanced absorbance ≈680 nm at elevated temperature (Figure 10c). The visible modulation of such complexes is further incorporated with the NIR modulation of VO_2 NPs to achieve a visible–NIR dual-band modulation with a promoted solar energy modulation ability (Figure 10c). Besides the nickel–chlorine complex, they have also investigated other similar complexes for smart windows, including the nickel–bromide and the cobalt–bromide systems,[180–182] which of all exhibit a strong absorbance in the visible spectrum and a reversible color change from the colorless to the blue.

3.1.3. Perovskite

TC perovskites have attracted quite research interest for smart windows in recent years. These materials are extensively studied for solar cells in conventional studies,[183–187] and emerge to smart windows recently. The group of Yang has prepared the TC perovskite,[188] the cesium lead iodide/bromide ($CsPbI_{3-x}Br_x$, $0 \le x \le 3$), which exhibits a reversible crystal structure change between the, namely, low-T and high-T phases (Figure 10d).[188] Increasing temperature leads to the $CsPbI_{3-x}Br_x$ changed from low-T to high-T phase, accompanying with a color change from colorless to orange. The high-T phase can be converted to low-T phase in a decreasing temperature under a moisture environment. A big T_{lum} contrast from 35% to 80% is achieved. The group of Bakr has prepared methyl-ammonium iodide ($MAPb_{3-x}I_x$) perovskite.[189] The perovskite gradually changes from yellow at 25 °C to orange at 60 °C (Figure 10e). This color change is due to the increasing iodide in the crystals (the increasing stoichiometric number of X), resulting in the redshift of the absorption edge (Figure 10f). The TC performance of $MAPb_{3-x}I_x$ perovskite is also demonstrated to be reversible.

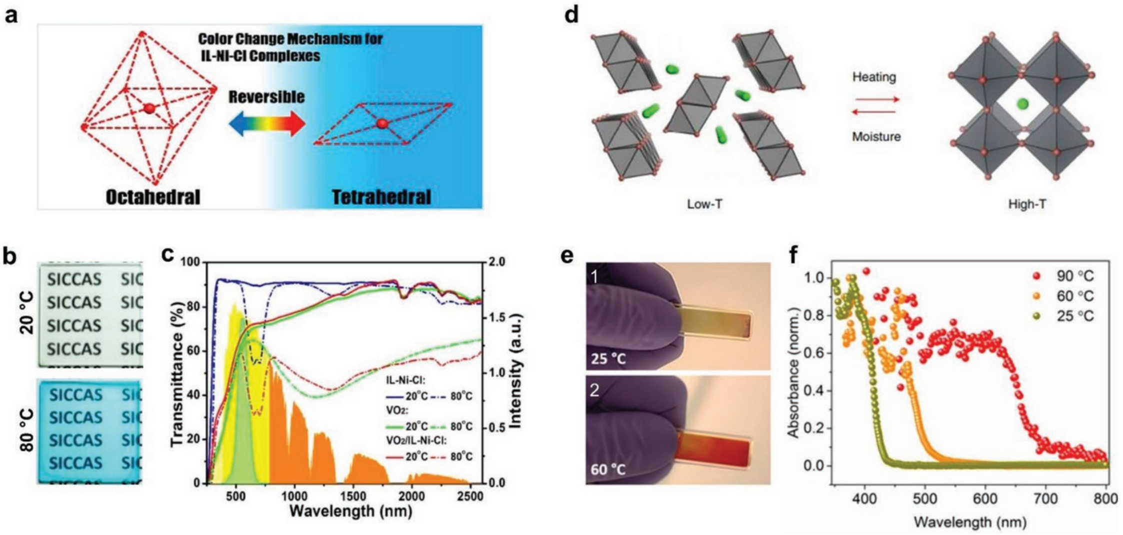

Figure 10. a–c) Smart windows based on thermal-responsive ionic liquid. a) The temperature-dependent crystal structure change. b) Photographs of ionic liquid–based foils at 20 and 80 °C. c) The temperature-dependent transmittance spectra of TC foil based on the ionic liquid, the VO_2, and the hybrid of them. Reproduced with permission.[176] Copyright 2016, American Chemical Society. d–f) Smart windows based on the TC perovskite. d) The crystal structure transition of perovskite during heating and cooling processes in a moisture environment. Reproduced with permission.[188] Copyright 2018, Nature Publishing Group. e) Photographs of the TC perovskite foil at b1) 25 °C and b2) 60 °C. f) Absorbance spectra of the perovskite-based foil. Reproduced with permission.[189] Copyright 2017, American Chemical Society.

Halder et al. found the color of $MAPbI_3$ also can be reversibly tuned by applying its dehydration-hydration process during the heating–cooling loop, leading to a bandgap change between 3.82 (25 °C) and 1.80 eV (60 °C).[190] Recently, the group of Gao prepared the lead-free TC perovskite, consisting of the cesium Ag bismuth bromide ($Cs_2AgBiBr_6$).[191] The $Cs_2AgBiBr_6$ was demonstrated with a slight color transition from 25 to 100 °C due to the changes in the bond lengths of Ag–Br and Bi–Br. The lead-free perovskite promises a safer choice than materials such as $CsPbI_{3-x}Br_x$ to remedy the lead toxicity for perovskite-based smart windows.

3.1.4. Crystal Orientation Transition in the Liquid Crystal

The tunable liquid crystal is also a potential candidate for TC smart windows.[192] The group of Yang has investigated the several polymer-stabilized thermal-responsive liquid crystals for smart windows.[193–197] They found the TC liquid crystals displayed a reversibly crystal orientation transition between the smectic (SmA) and the chiral nematic (N*) phases (**Figure 11**a).[193,197] The liquid crystal–based TC foils exhibit highly transparent at the low temperature while is opaque at the high-temperature state due to the strong light scattering effect (Figure 11a). To make the materials more processable, they developed a polymer-stabilized and polymer-dispersed coexistent system with strong shear strength.[194] The coexistent system was demonstrated a similar thermal–optical mechanism to the polymer-stabilized system. The TC films based on such a system is observed with a huge transmittance contrast of 70–80% in the visible spectrum. The films are flexible and demonstrated to be successfully produced on the meter scale. Kakiuchida et al. have reported a thermal-responsive liquid crystal system with controllable mesoscale domain structures by mixing with the reactive mesogen.[198] These domains are controlled by the reactive mesogen to be either disordered or ordered, leading to either the multiaxial or uniaxial orientation of liquid crystals. With the ordered domains, the system is transparent at low temperature and can scatter light at high temperature. Moreover, the liquid crystal composite films with the NIR shielding functionality have been prepared by incorporating with the NIR-blocking materials, such as the ITO[196] and the tungsten bronze (Cs_xWO_3) NCs.[197] For example, Liang et al. have prepared the core–shell SiO_2–ITO NPs through a colloidal method.[196] By decreasing the dopant concentration, these NPs display a tunable color from blue to colorless as well as an LSPR position redshift on NIR range from ≈1500 to 2500 nm. They further incorporated these NPs in the coexistent liquid crystal system. It is demonstrated the thermal–optical response of the liquid crystal system functions well in the visible spectrum and the introduction of ITO NPs significantly decrease the NIR transmittance at both low and high temperature (Figure 11b). The liquid crystal and the ITO incorporated film display narrow thermal hysteresis less than 2 K in ≈303 and ≈305 K, respectively (Figure 11c). Similar to ITO, the Cs_xWO_3 nanorod is also demonstrated to be suitable for NIR shielding for the liquid crystal films due to its high transparency and strong absorption in the visible and NIR spectrum, respectively.[197] In addition, Schenning and co-workers reported the reflection band of liquid crystals is tunable and may be suitable for smart windows.[20,199] For example, the hydroscopic cholesteric liquid crystals are developed to be thermal-responsive.[20] The system displays a tunable reflection band from ≈1150 nm at 70 °C to ≈1550 nm at −2 °C due to the temperature-induced swelling effect through the water vapor absorption. They suggested such films may suitable for high humidity green houses.

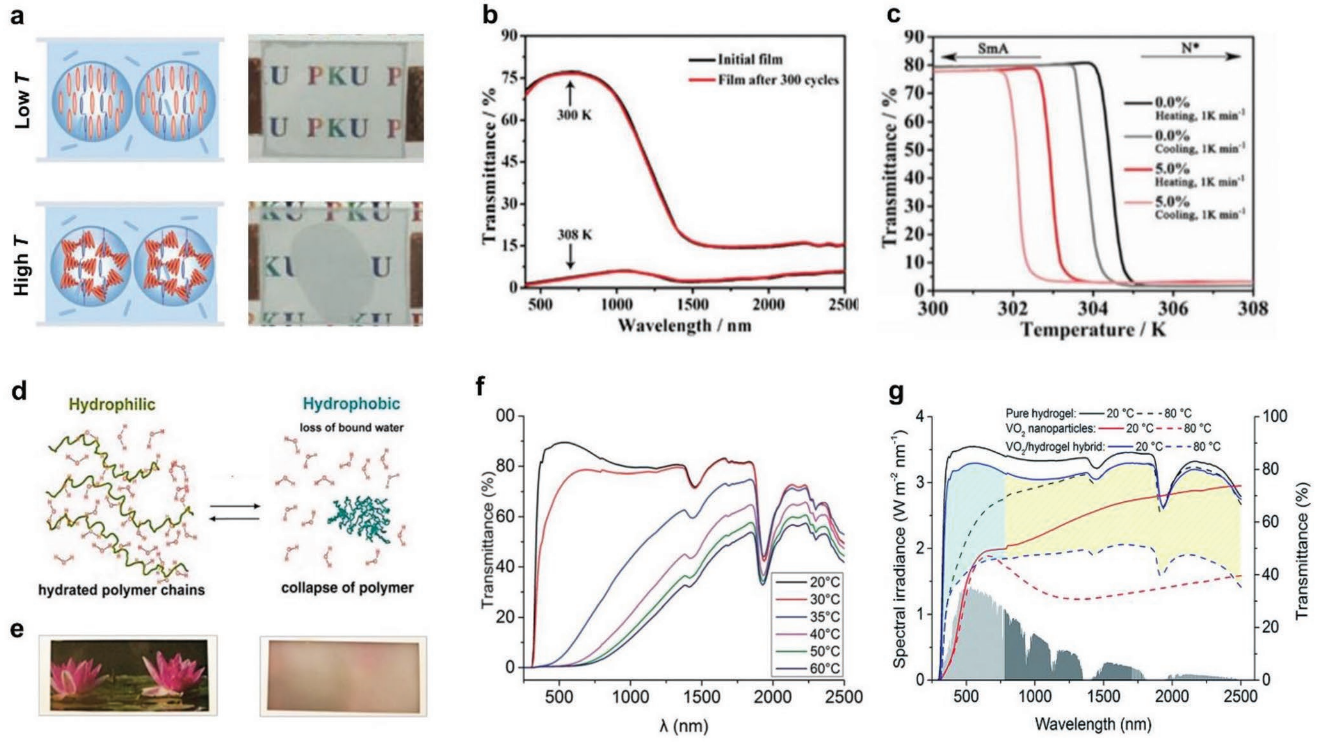

Figure 11. a–c) Smart windows based on liquid crystals. a) The temperature-dependent orientations of s and the corresponding photographs of liquid crystal–based foils at different temperature. b) Transmittance spectra of the liquid crystal–based foils at 300 and 308 K. c) Heating and cooling loops of the liquid crystal–based foil and the film containing 5 wt% ITO. Reproduced with permission.[197] Copyright 2017, Royal Society of Chemistry. d–g) Smart windows based on thermal-responsive hydrogels. d) Schematic of the temperature-induced hydrogel responses. e) the corresponding photographs of TC films based on such hydrogel. Reproduced with permission.[204] Copyright 2018, John Wiley & Sons. f) The temperature-dependent transmittance spectra of TC films based on the hydrogels. Reproduced with permission.[126] Copyright 2014, Royal Society of Chemistry. g) The temperature-dependent transmittance spectra of TC films based on the hydrogel, VO_2, and their hybrid. Reproduced with permission.[175] Copyright 2015, Royal Society of Chemistry.

3.1.5. Phase Separation of Hydrogel

The thermal-responsive hydrogel for TC windows has been first reported by Long's group using the poly-(*N*-isopropylacrylmide) (PNIPAm) hydrogel.[126] The hydrogel allows the incident light to pass through at low temperature, while strongly scatters the incident light at high temperature due to the formation of scattering centers of the aggregated polymer microparticles (Figure 11d). The change is due to the phase transition of the material at a lower critical solution temperature (LCST) (Figure 11d).[126] Foils based on such hydrogel can reversibly change from colorless high-transparency at low temperature to white color to block the background image at elevated temperature (Figure 11e). The transmittance is demonstrated to decrease gradually from 20 to 60 °C, leading to a strong visible modulation and a relatively moderate NIR modulation (Figure 11f). The biggest spectrum contrast is observed between 30 to 35 °C that is consistent with the LCST of the PNIPAm (Figure 11f). The NIR-shielding effect can be achieved by incorporating with antimony-doped tin oxide (ATO) NCs and increasing the thickness of hydrogel.[200] Also, the hydrogel can also be incorporated with VO_2 for the broadband optical modulation enhancement (Figure 11g),[175,201] or be integrated with transparent electrodes for electrical control.[202] More recently, the group of Fang has developed the PNIPAm-2-aminoethylmethacrylate hydrochloride with a controllable particle size of ≈1400 nm at 20 °C to ≈550 nm at 35 °C.[203] They have demonstrated the scattering effect is strongly related to the particle size and can be explained by the Mie theory. To make the materials easily processable, Zhou et al. have prepared a composite by incorporating the PNIPAm into the water-rich matrix based on the silica–alumina gel.[204] They have demonstrated the composite is suitable for printing.

3.2. Multifunctional Thermochromic Devices

3.2.1. Thermochromic with Electrothermal Devices

The passive way may be an obstacle to the TC smart windows for applications, such as the privacy windows, where active control is necessary. To actively control the TC windows, the electrothermal devices are developed to integrate with TC materials. Generally, the highly transparent electrodes are applied to heat up the TC materials through a Joule heating upon an applied voltage to the electrodes.

As the most studied TC material, VO_2 layer was investigated to combine with electrothermal devices. The devices are commonly based on transparent electrodes using conductive materials with either high T_{lum} or a very low loading. The group of

Zou has prepared the VO_2 thin films on the mica substrates through an rf-plasma assisted molecular beam epitaxy technique, followed by the vapor deposition of a conductive layer consisting of CNT (**Figure 12**a).[205] The prepared mica-VO_2-CNT foils can be easily peeled off to form freestanding foils that are ready for attaching to other substrates (Figure 12a). The peel-off process using a tweezer is presented in Figure 12b, and the freestanding foils are flexible and can be produced in centimeter-scale (Figure 12c,d). Li et al. prepared the transparent electrodes using Ag NWs, followed by the deposition of TC VO_2 NPs with a significant decreasing in NIR spectrum under an applied voltage around 6.5–8 V observed (Figure 12e).[206] Further increasing the voltage does not lead to an obvious spectrum change in NIR transmittance, which demonstrates a typically optical modulation property of VO_2. The Ag–VO_2 system is very stable and displays no transmittance change after 100 times on–off cycles. Moreover, they also applied the ITO glassed for the electrothermal layer to heat the adjacent VO_2 layer. They have deposited the VO_2 NPs onto a commercialized ITO glass.[207] The applied voltage to tune the transmittance around 12–15 V, which is slightly higher than the Ag-based layer.

The transition temperature of hydrogel (≈40 °C) is relatively lower than that of VO_2 (≈65 °C). Thus, a relatively lower voltage is required to tuning the hydrogel-based smart windows. Zhou et al. have developed an Ag mesh based transparent electrothermal electrodes, and have integrated such electrodes with hydrogel-based TC foils for actively optical modulation.[202] A voltage lower than 2 V is sufficient to heat up the attached

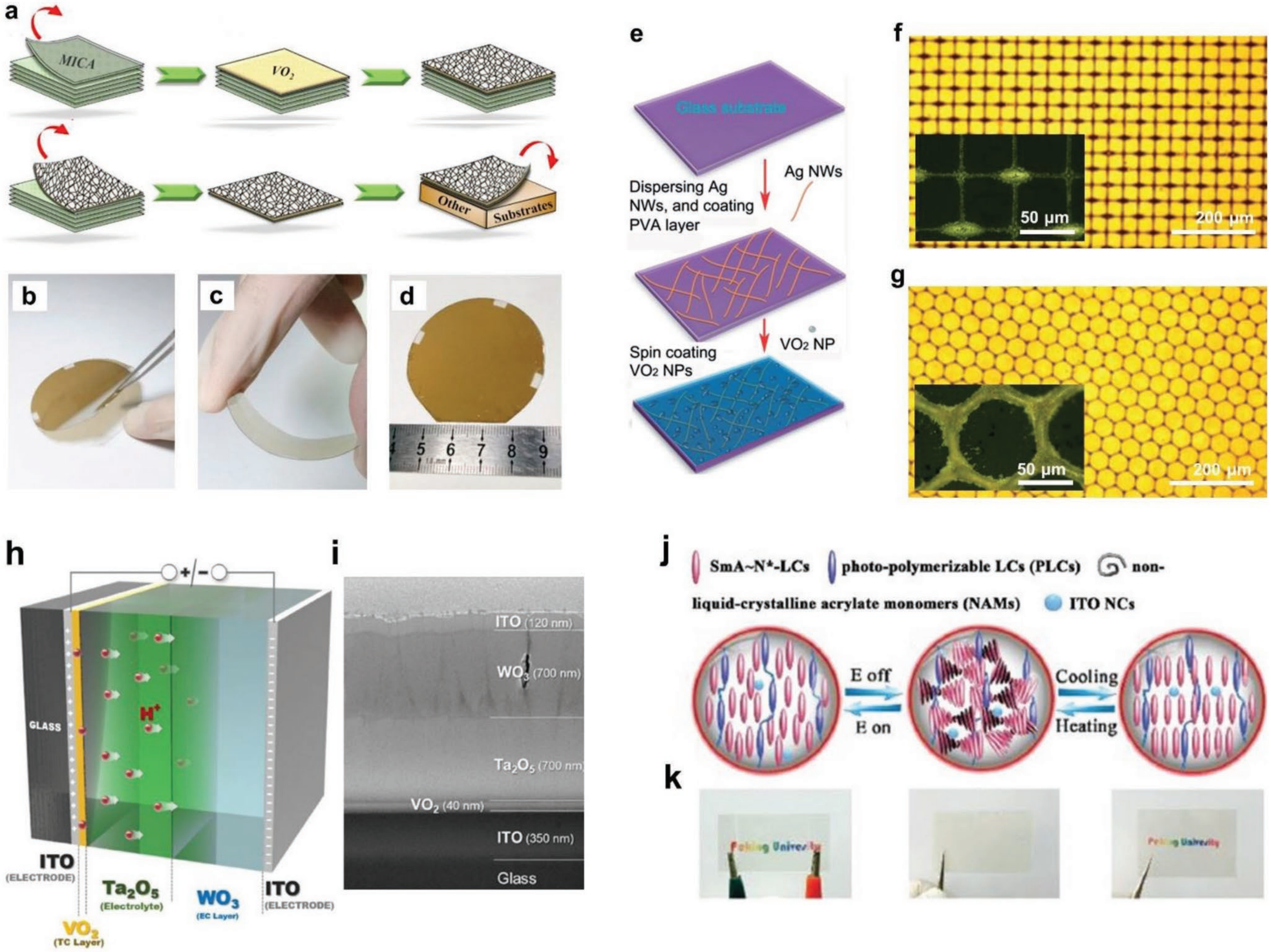

Figure 12. a) Schematic of the fabrication process of the CNT–VO_2–mica films. The CNT network is illustrated as the black mesh. Photographs of b) the peel-off and c) the bending processes, as well as d) the large size of the film. Reproduced with permission.[205] Copyright 2017, Elsevier. e) Schematic of the fabrication process of the Ag–VO_2 electro-thermochromic film through the sequential depositions of Ag NWs and VO_2 NPs. Reproduced with permission.[206] Copyright 2014, Royal Society of Chemistry. f,g) Microscope images of the produced Ag mesh electrodes with f) the square and g) the honeycomb arrays. Inserted figures are the high-magnification images. Reproduced with permission.[202] Copyright 2016, John Wiley & Sons. h) Schematic of the VO_2–WO_3 hybrid TC–EC system. The design is constructed of the ITO/VO_2/Ta_2O_5/WO_3/ITO multilayer structures on the glass. i) The cross-section SEM image to illustrate the multilayer structures on the produced sample. Reproduced with permission.[210] Copyright 2019, American Chemical Society. j) Schematic of the mechanism for the dual-stimuli responsive optical modulation of the TC-EC system based on liquid crystals only. k) Corresponding photographs of the sample under the electric or thermal stimulus. Reproduced with permission.[196] Copyright 2017, Royal Society of Chemistry.

PNIPAm-based TC film to its LCST that is the critical temperature for optical modulation. In the experiment, Ag mesh is fabricated through a mesh-assisted assembly process using Ag NPs. The Ag meshes are produced with the microsquare and honeycomb structures (Figure 12f,g), of which lines consist of aggregated Ag NPs (inset in Figure 12f,g). They demonstrated the response time decreases from 120 to 40 s when increasing the voltage from 2 to 6 V. The group of Kulkarni has applied the Sn mesh electrodes with the TC foil consisted of hydroxypropyl methyl cellulose (HPMC).[208] The Sn electrodes display a high transmittance of 80%, and the integrated device is demonstrated with a switch-on voltage of 8 V. Besides, they also developed the Cu-based electrodes for HPMC-based foils, resulting in a similar electro-thermochromic properties with an on–off voltage of 4.5 V.[209] They suggested the use of Sn or Cu provides a more affordable candidate to replace the Ag electrode. Though active control can be achieved by the electrothermal method, additional electricity consumption is required for the persistent heating process to maintain the temperature.

3.2.2. Thermochromic with Electrochromic Devices

The integration of TC with EC gives rise to dual-responsive multifunctional devices. These devices commonly consist of TC and EC materials that work independently, which is distinguished differently from the electro-thermochromic techniques that rely on the electroinduced Joule heating effect. The group of Kim has developed a hybrid system by integrating the VO_2-based TC layer with the WO_3-based EC system.[210] In their design, a VO_2 TC layer is incorporated in the EC system, which is constructed of two ITO layers as electrodes, a Ta_2O_5 layer as an electrolyte, and a WO_3 EC layer (Figure 12h). The hybrid system is successfully produced with ITO/VO_2/Ta_2O_5/WO_3/ITO multilayer structures (Figure 12i). The device presented an effective EC mode. At room temperature, the device displays a yellow-brown color with a T_{lum} of 70% at the bleached state, while changes to the dark color with a T_{lum} of 30% at colored state under an electric stimulus. However, the transmittance further decreases under an increasing temperature to 80 °C, suggesting the TC mode of VO_2 is affected by the WO_3-bases system. The group of Yang has developed a hybrid system based on TC VO_2 and the EC liquid crystals.[195] In general, the VO_2 NCs and the liquid crystals are dispersed in the porous polymer matrix. A dual-band modulation property is demonstrated in the produced films. The transmittance modulation on the spectrum range of 400–1000 and 1000–2500 nm is successfully achieved by controlling the applied voltage and the temperature. The VO_2 and liquid crystals work independently, leading to the four different optical states: 1) low temperature/no electrical field, 2) high temperature/no electrical field, 3) low temperature/electrical field, and 4) high temperature/electrical field. They also demonstrated both the thermal- and electrochromic on systems using liquid crystals only. The liquid crystals in polymer matrix can also reversibly change from a chiral N* to a SmA phases under either a temperature variation or an applied electric field (Figure 12j),[196,211] accompanying with a distinguish transmittance changes from high transparent to entirely opaque (Figure 12k).[196] The group of Yan incorporated the PNIPAm-based TC with the diallyl-viologen-based (DAV-based) EC.[212] In the EC, the colorless DAV^{2+} can be changed to the blue/violet viologen cation radicals in the electrochemistry system. They have suggested the DAV also played a role to assist the temperature-dependent cross-linking of PNIPAm. The thermal- and electrochromic modes can work independently in the device. The device changes its appearance from a transparent to a white opaque under the temperature increases from 20 to 36 °C, while it tunes to the blue/violet color under the applied electric field regardless to the temperature (20 or 36 °C).

3.2.3. Thermal-Responsive Reconfigurable Structures

It is also a promising method to integrate reconfigurable structures with thermal-responsive materials. Through the integration, the reconfigurable structures can change its effect area or the tilting orientation of functional parts in programmable ways.[213–215] The group of Yin investigated the thermal response of kirigami-inspired metamaterials using thermal shrinkable tapes.[216] They found the structure and orientation evolutions of the metamaterials are strongly related to the localized stress induced by the attached tapes. The group of Long integrated the reconfigurable structures with VO_2 by dispersing the VO_2 NPs in the kirigami-inspired metamaterials consisted of polydimethylsiloxane (PDMS).[152] The fully thermal-responsive system is fabricated by attaching the thermal-shrinkable tapes by sides and is tested in the house demo (**Figure 13**a). It is observed the open cuts are gradually closed under an increasing temperature from 20 to 70 °C (Figure 13b). Such an integration method is demonstrated to improve the ΔT_{sol} of VO_2-based TC films by enhancing the modulation ability in the visible range, which cannot be controlled by films with VO_2 only (Figure 13c). The method is feasible and robust, which may inspire the novel design of smart windows.

3.2.4. Photo-thermochromics

TC materials can also response to the optical stimulus through the absorption-induced heating effect (photothermal effect). To enhance the effect, TC materials are commonly incorporated with high-absorbance materials, such as such as GO,[217] ATO,[218] Cs_xWO_3,[197] or the LSPR material such as gold NPs to produce heat and prompt the phase change of TC materials.[219] It should be noted that the absorbance peak of the photo-thermochromic material should be carefully designed as the luminous transmittance is an important criterion for window application. For example, although amorphous carbon shows good photothermal performance,[165] it cannot be used as light absorption material for window due to its strong absorption in the visible range (380–780 nm).

Cs_xWO_3/hydrogel composite is one of the photo-thermochromic material that has been intensively researched in recent year. Compared with other light absorbing material, Cs_xWO_3 selectively absorb the NIR light, which does not contribute to the indoor lighting.[220] On the other hand, as the NIR is one of important factor for heating effect,[221] the

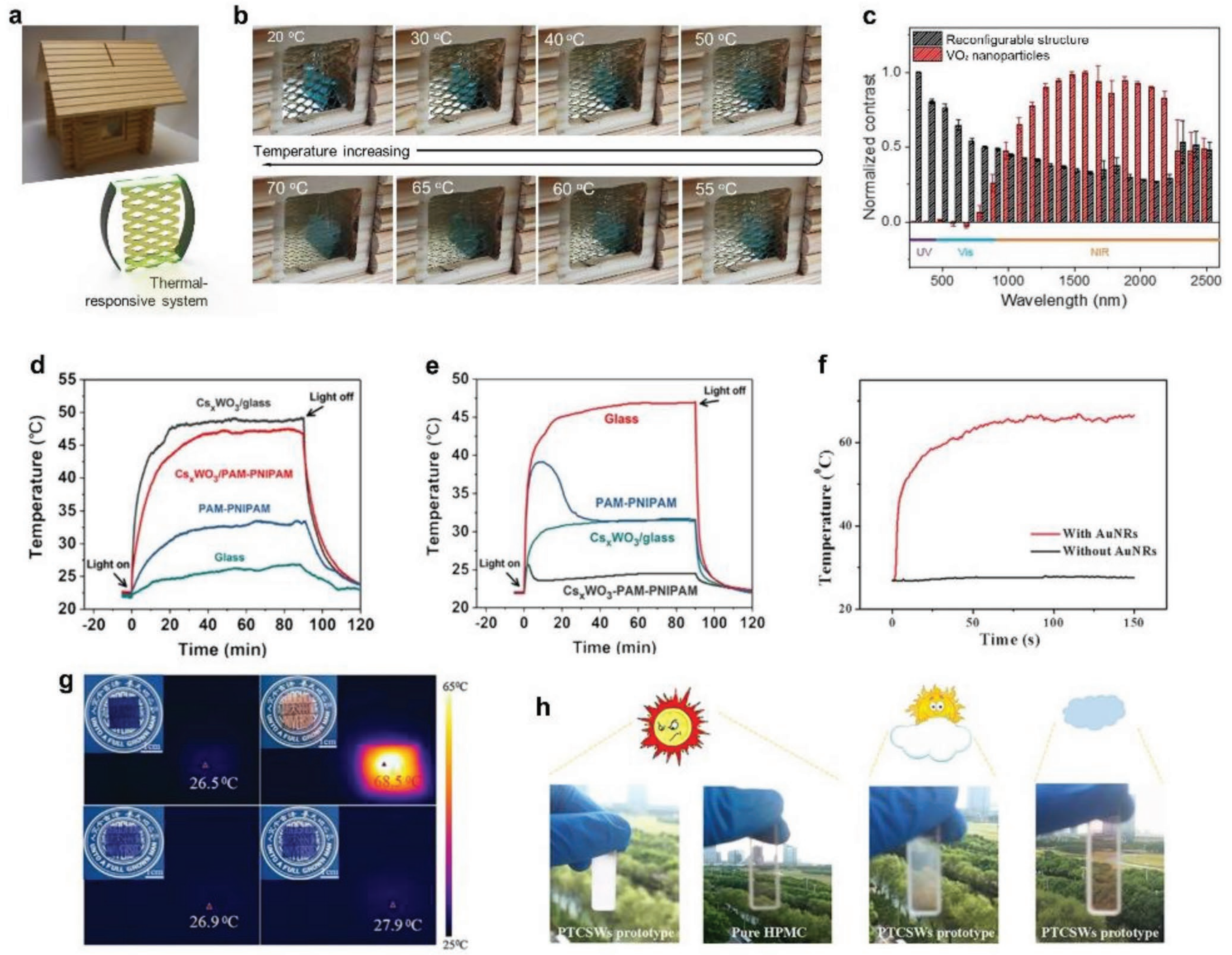

Figure 13. a) The photograph of the house demo and the illustration of the thermal-responsive system constructed by the reconfigurable foil and the thermal-shrinkable tapes. b) Photographs of the temperature-dependent configurations the foil as in the smart window demo. c) The wavelength-selective modulation capabilities of the reconfiguration structures and the VO_2 NPs. The normalized transmittance contrasts are recorded for assessment. Reproduced with permission.[152] Copyright 2019, Elsevier. d) Time-dependent top surface temperature changes of Cs_xWO_3 film, Cs_xWO_3/PAM–PNIPAM, PAM–PNIPAM, and glass windows in response to 1000 W m^{-2} light irradiation. e) Time-dependent room temperature changes of Cs_xWO_3 film, Cs_xWO_3/PAM–PNIPAM, PAM–PNIPAM, and glass windows in response to 1000 W m^{-2} light irradiation. Reproduced with permission.[220] Copyright 2018, American Chemical Society. f) Temperature rise traces of PVA/dyes films with and without Au NPs. g) The infrared photographs of the PVA/dyes/Au NP film (upper row) and PVA/dye film (lower row) before and after illuminated by laser. h) The photographs of the composite and pure hydrogel at blistering summer day (left), at soft sunlight summer day (middle), and at cloudy day (right). Reproduced with permission.[219] Copyright 2018, John Wiley & Sons.

blocking of NIR reduces the heating effect induced by solar light. Upon the irradiation of light, the surface temperature of Cs_xWO_3/polyacrylamide–PNIPAM (PAM–PNIPAM) composite reaches 47 °C, which is ≈20 °C higher than the glass (Figure 13d). Therefore, the composite shows promising photothermal effect. On the other hand, the indoor temperature of the composite is ≈25 °C at the stable state, which is significantly lower than the glass (Figure 13e). Moreover, it worth to note that the Cs_xWO_3/PAM–PNIPAM composite shows a faster color switching speed than the pure PAM/PNIPAM hydrogel. As the result, the temperature decreasing happens earlier for the composite. The authors then demonstrate the hydrogel is capable for flexible smart window applications. Different from conventional light absorb material, the LSPR material such as gold NP interact with light with certain wavelength and generate the heat.[222] As the wavelength that excites the LSPR effect is relate to the size and geometry of the NP, it is possible to control the color of the composite through control the size and shape of the NP. Similar to the Cs_xWO_3, the Au NP/polyvinyl alcohol (PVA) composite shows good photothermal performance (Figure 13f,g) and light regulation ability. Moreover, the outdoor experiment shows that the transmittance of the composite is related to the solar light intensity (Figure 13h). When the sun light is not strong, the composite will become translucent instead of opaque to ensure a sufficient indoor lighting.

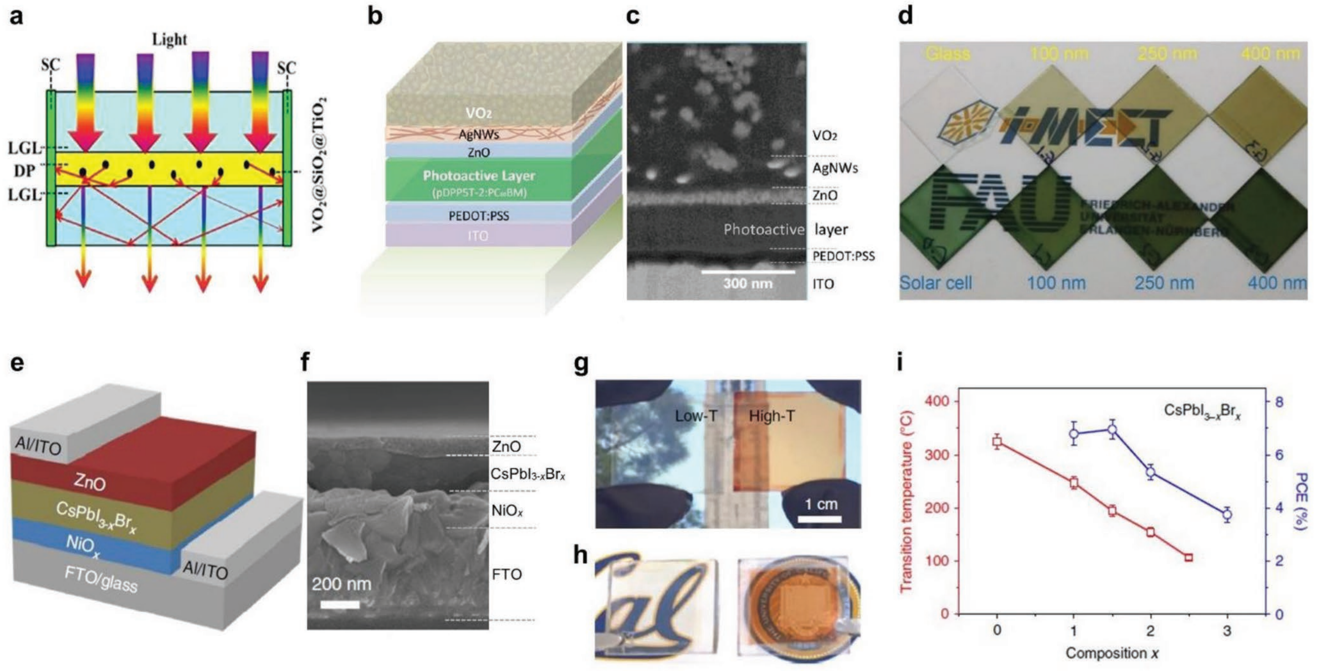

Figure 14. a) Schematic of the TC VO_2 layer with solar cells on laterals to collect the scattering light. The "LGL," "DP," and "SC" indicate the light guide layer, the low reflective index medium (DP), and the solar cells, respectively. Reproduced with permission.[228] Copyright 2013, Nature Publishing Group. b) Schematic of the TC VO_2 layer that overlays on the solar cell to collect the transmitted light and c) the corresponding SEM cross-section image of the produced sample. d) The produced pure VO_2 and the VO_2/solar cells composite samples with different VO_2 layer thickness. Reproduced with permission.[229] Copyright 2015, John Wiley & Sons. e) Schematic of the $CsPbI_{3-x}Br_x$-based perovskite solar cells with TC, and f) the corresponding SEM cross-section image of the produced sample. Photographs of g) the TC $CsPbI_{3-x}Br_x$ coating and h) the $CsPbI_{3-x}Br_x$-based solar cells at low (samples on left) and high temperature (samples on right). i) The composition-dependent power conversion efficiency (PCE) and transition temperature of $CsPbI_{3-x}Br_x$. Reproduced with permission.[188] Copyright 2018, Nature Publishing Group.

3.2.5. Thermochromic with Solar Cells

The emerging integration of solar cells to smart windows promises the possibility to achieve both the energy (electricity) conservation and generation functionalities for architectural windows,[223] which promises better energy utilization than the window based on semitransparent solar cells with solely energy conversion functionality.[224–227] The group of Gao has combined the TC VO_2 layer with solar cells through two methods: 1) the solar cells are attached to the laterals of TC layer to collect the light scattered by the VO_2 NCs (**Figure 14**a),[228] and 2) the TC layer is overlaid on the solar cell to collect the light that passes through the layer (Figure 14b).[229] In the first method,[228] the TC layer consists of VO_2–SiO_2–TiO_2 NCs in polyurethane matrix. These NCs can scatter the incident light and forward to the solar cells on laterals (Figure 14a). The prototype achieves a ΔT_{sol} of 7.5% and a power conversion efficiency of 0.5%. In the second method,[229] the VO_2 NPs are coated onto the solar cell, consisted of the sequential layer of Ag NWs, ZnO, photoactive layer, the poly(3,4-ethylenedioxythiophene):poly-styrene sulfonate, respectively (PEDOT:PSS), and ITO layers (Figure 14c). The samples are produced with different VO_2 thickness. All samples display the green color and the darkness increases on samples with thick VO_2 coatings (Figure 14d). The device is demonstrated with a power conversion efficiency of 3.1%, which is significantly higher than that of the device based on the scattering effect. The group of Yang has successfully developed a TC perovskite solar cells.[188] The solar cells are designed as in Figure 14e based on the functional layer of $CsPbI_{3-x}Br_x$, and the layer structures are successfully prepared (Figure 14f). The functional layer displays temperature-dependent colors that are the low-temperature colorless and the high-temperature orange states (Figure 14g), which also be observed on the produced solar cells (Figure 14h). The devices are demonstrated a peak power conversion efficiency of 7% (Figure 14i). Though the transition temperature is relatively too high for TC windows (Figure 14i), the method provides a new way for bifunctional energy-conservation and -generation smart windows.

3.3. Brief Conclusion

The TC windows develop rapidly in the past few years, including the development of thermal-responsive materials and additional functionalities beyond light modulation as summarized in **Table 2**. It is a promising direction to explore novel temperature-responsive materials for TC smart windows as well as further enhance the performance of current materials and technologies. Suitable materials should be able to switch the optical property between the cold and the hot states with significant contrast, an appropriate transition temperature in ≈20–40 °C with high luminous transmission maintained Further research effort to develop the multifunctional TC windows

Table 2. Summary of strategies and multifunctional devices.

	Materials	Mechanism	Modulated solar spectrum [nm]	Transition temperature [°C]	Appearance change	Physical phase	Ref.
Strategies	VO_2-based nanocrystals	Crystal structure transition	750–2500	30–68	Unchanged yellow-brown	Solid	[4,123,134,153,154,230,231]
	Ionic liquid		500–800	–[a)]	Transparent-to-colorful	Liquid	[176,180–182]
	Perovskite		400–700	25–90	Colorful-to-colorful	Solid/liquid	[188–191]
	Liquid crystal	Crystal orientation transition	400–2200	29–33	Transparent-to-white	Solid/liquid	[193–197]
	Hydrogel	Phase separation	250–2200	≈32	Transparent-to-white	Liquid	[126,175,200–204]
		Methods			Comments		
Multifunctional devices	With electrothermal technique	Using inorganic conductors, such as ITO, Ag NW, CNT, Sn, or Cu			The consistent heating process is required, consuming additional electricity		[202,205–209]
	With EC	By either combining a TC and an EC material or using liquid crystals with dual functionality			A complex system may decrease the T_{lum} and ΔT_{sol} performance for both the functionalities		[195,196,210–212]
	Thermal-responsive reconfigurable structures	By attaching thermal-responsive materials to target places of the structures			Additional space is required for the structure deformation; also, an additional control system may be needed		[152,216]
	Photo-thermochromics	Using composites with TC and high-absorbance materials			The introduced TC materials may decrease the T_{lum} and ΔT_{sol}		[197,217–219]
	With solar cells	By either integrating with photoactive layers or using TC perovskites			Solar energy conversion efficiency is relatively low and the durability is questionable		[188,228,229]

a)Note: "–" means data not available.

are meaningful; though current techniques (Table 2) are far from being mature, these works are indeed inspiring. For example, the energy-conservation and generation bifunctionality promises very useful, even though the performance and durability are limited. Lastly, to commercialize the TC windows, the materials and techniques are preferred to be durable, inexpensive, and easy to process.

4. Mechanochromics

MC smart window is often made of mechanoresponsive optical materials, which represents an emerging smart window with its optical properties tuned by simple mechanical strain. It has a few unique advantages compared to conventional TC and EC smart windows, e.g., simple construction, low cost, and fast response time. The working principle of mechanoresponsive smart windows is relatively straightforward: mechanical strain can deform and reconfigure either the surface morphologies or internal structures of composed mechanoresponsive optical materials, which in turn change the optical transmittance through light scattering or diffraction of visible light. Several strategies have been proposed by harnessing mechanical strain for switchable optical properties in smart window, including surface wrinkling or buckling-driven delamination, NPs-matrix composites, and tilting of kirigami structures. Each strategy has its own advantages and drawbacks. In this section, we review the recent progress in the emerging mechanoresponsive smart windows in terms of mechanism, transmittance range, and strain dependency.

4.1. Wrinkling-Based Smart Windows

Wrinkling is a ubiquitous phenomenon in our daily life ranging from crumpled raisins to human skin wrinkles.[232] In 1998, Bowden et al. first reported the fabrication of self-assembled nanoscale surface patterning through wrinkling of gold nanofilms on soft elastomeric PDMS substrates.[233] A gold nanofilm was first coated on the PDMS substrate at an elevated temperature. Subsequent cooling led to the compressive stress in the film due to the larger thermal expansion coefficient in PDMS substrates. When the temperature is beyond a critical value, spontaneous surface wrinkling occurs, resulting in different ordered and disordered wrinkling patterns at small scales. Since then, extensive researches have been conducted to exploit the underlying mechanism and broad potential applications of surface wrinkling in surface-related properties. Compared to thermal loading, mechanical strain is simpler and more controllable by simply stretching or compressing the soft substrate in one or two directions. One of the most intriguing properties of wrinkling is that both periodicity (wrinkle wavelength) and height (wrinkle amplitude) of wrinkles are highly controllable and dynamically tunable by simple mechanical strain, e.g., the wrinkles could be reversibly flattened and generated upon mechanical stretching and releasing, consequently, the surface properties arising from the morphable wrinkles can be dynamically and continuously tuned by the applied strain.

The dynamic tunability of mechanoresponsive wrinkles makes it a promising potential candidate for constructing MC smart windows. It requires the wrinkling bilayer system (thin films on soft substrates) to satisfy several conditions for potential smart window applications. First, both films and substrates at unwrinkled state will be optically transparent for allowing high optical transmittance. Second, after wrinkling, the periodicity or wavelength of patterned surface wrinkles should be in the sub-micrometers range to interact with light. Similar to the Bragg gratings, reflecting and scattering visible light from the surface wrinkles will lower the optical transmittance of the bilayer system. Third, the MC smart window should be mechanically robust under cycles of mechanical loading and unloading without sacrificing its optical performances.

Depending on the directions of applied strain in the soft substrates, 1D or 2D wrinkling patterns can be generated through uniaxially or biaxially compressing the soft substrates, respectively. Correspondingly, different wrinkling patterns will lead to distinct optical and mechanical performances, as discussed below.

Based on 1D wrinkles, Kim et al. proposed a potential smart window through oxygen plasma treatment of prestrained PDMS thin sheets (**Figure 15**a–c).[234] It achieved a reversible transition between an optically transparent state and a translucent state by flattening and reinstating wrinkles through mechanical strain. PDMS is widely used as substrates for smart window applications due to its similar optical clarity to glass. The fabrication process is shown in Figure 15a. A thin sheet of PDMS substrate is first uniaxially prestretched to a small strain of 20%, followed by oxygen plasma treatment under stretched state to generate a thin layer of amorphous stiff silica nanofilm. Release of the prestrain leads to orthogonal microwrinkles to the prestretched direction. Restretching the PDMS sheet flattens the microwrinkles and returns to its initial transparent state (Figure 15b). Further stretching (50% strain) beyond its original prestrain leads to the orientation switch of microwrinkles to align with the

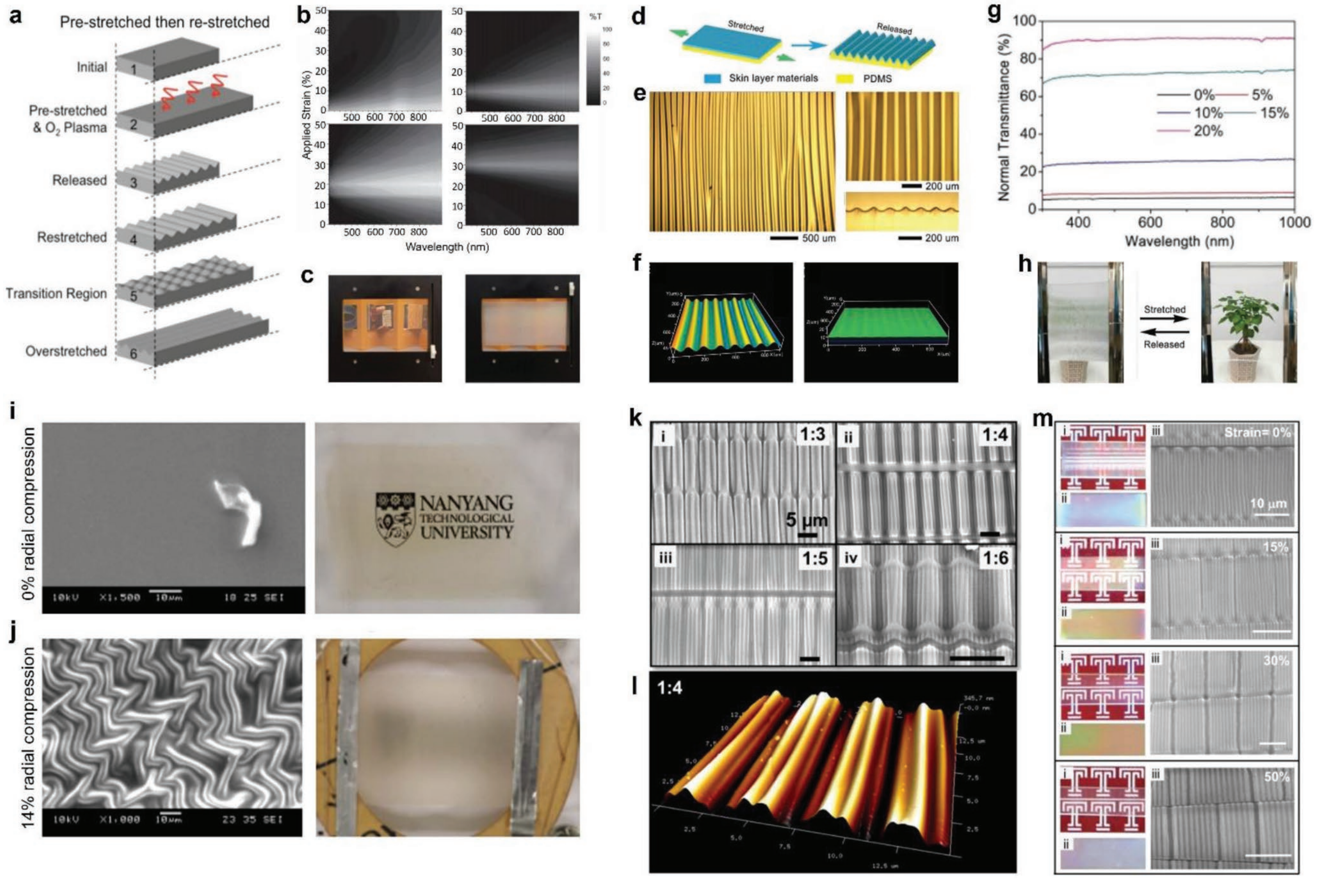

Figure 15. a) Schematics of preparation procedures for samples with prestretching. b) Optical transmittance contour plot of wrinkled PDMS sheets as a function of wavelength and applied strain with prestretching values of 0%, 10%, 20%, and 30%. c) Photographs showing the transition between optically clear state (left, unstretched) and opaque state (right, stretched). Reproduced with permission.[234] Copyright 2013, John Wiley & Sons. d) Schematic illustration of the fabrication process of surface wrinkles on the PVA/PDMS bilayer film. e) Bright-field optical microscope images of the surface wrinkles on top. f) Confocal laser scanning microscope images of the PVA/PDMS bilayer film at (left) released state and (right) stretching state with 20% mechanical strain. g) UV–vis normal transmittance spectra of the film under different mechanical strains. h) A large size PVA/PDMS bilayer film with surface wrinkles for smart windows. Reproduced with permission.[235] Copyright 2018, John Wiley & Sons. i,j) SEM images of a ZnO thin film coated on VHB elastomer membrane and optical appearance of a log placed 10 mm beneath the same membrane: i) the clear state at 0% radial compressive strain; j) the translucent state at 14% radial compressive strain. Reproduced with permission.[236] Copyright 2016, Optical Society of America. k) SEM images of hierarchical wrinkles with different wavelength ratios. l) AFM images of 1:4 hierarchical wrinkles. m) The optical images showing the transparency and iridescent color and corresponding SEM at different stretching strain. Reproduced with permission.[237] Copyright 2017, American Chemical Society.

stretching direction. Correspondingly, the PDMS sheet transits from translucent (less than 20% optical transmittance, orthogonally wrinkles upon full release of prestrain) to transparent (flattened upon restretching), and to translucent again (parallel wrinkles upon overstretching), with the monotonic increase of restretching strain (Figure 15c). The whole stretching process is fully reversible by releasing the applied strain. The stretching/releasing cycling was tested for more than 100 000 times with no noticeable changes in the optical properties. Similarly, Li et al. applied UV–ozone to treat both sides of the PDMS sheet forming a silica/PDMS/silica sandwiched structure for potential smart window application.[238] They showed that double-sided wrinkled PDMS sheet can achieve a lower optical transmittance compared to single-sided wrinkled one. Similar to plasma treatment, UV–ozone treatment could generate an oxidized layer of silica on the surface of PDMS sheet but with a much larger thickness of over tens of nanometers. Rather than the substrate prestrain method for generating wrinkles, a combined orthogonal wrinkles and cracks were formed by directly stretching the treated PDMS sheet uniaxially, which could strongly scatter the light through largely increased surface roughness for a low opacity. They showed that they can modulate the optical transmittance from 92% to 9.2% at an applied strain of 50%. Similar transparent to opaque transition is observed from strain-controlled cracks and folds by stretching transparent PVA/laponite films on PDMS substrates.[239]

It should be noted that when uniaxial strain is applied to PDMS substrates, microcracks are unavoidable in their oxidized coating through either plasma or UV–ozone surface treatment of PDMS substrates due to the brittleness of silica coating. To address the cracking issue, Jiang et al. prepared a cracking-free wrinkling based tunable optical film through dip-coating deposition of more stretchable polymeric films on prestrained PDMS substrates (Figure 15d–f).[235] They tested different coatings, including PVA, chitosan (CS), hydroxyethyl cellulose, and the mixtures of PVA and CS. They showed that PVA/PDMS bilayer film exhibits the best mechanoresponsive optical switching properties. Despite the applied large prestrain of 50% in the substrate, they showed that the transmittance in the visible light range could be tuned from 6% to 91% by only applying 20% stretching strain, showing high sensitivity of transmittance on the strain change (Figure 15g,h). The switch between opaque and transparent states was cycled for over 2000 times without failure.

Compared to the case of uniaxial strain, the biaxial compression can generate more complex 2D wrinkling patterns, which could be ordered or disordered.[240] The 2D wrinkling patterns will have a stronger interaction with light and result in a lower transmittance. For example, Shrestha and Lau presented a tunable window device based on the wrinkling of a ZnO thin film on acrylic elastomer membrane.[236] The acrylic membrane is radially prestretched to a 14% strain followed by deposition of 50 nm ZnO thin film through e-beam evaporation technique. Prestrain release leads to zig-zag wrinkles with a wavelength of 10 μm and amplitude of 1 μm (Figure 15i,j). By analyzing the effect of microscopic wrinkles on diffuse refraction of light, they found that higher aspect ratio of wrinkles, defined as the ratio of wrinkle amplitude to wavelength, leads to a higher spatial variation of incident angle, and thus stronger diffusing refraction of light. Furthermore, the biaxial wrinkling micropatterns will scatter light more effectively compared to the unidirectional wrinkling patterns. The transmittance of the zig-zag wrinkles fabricated in this work could be reversibly tuned in the range of 93–3% by mechanical strain (Figure 15i,j). The stretching and releasing cycles were repeated 30 times to test the durability of smart windows. The result shows no obvious degrading after 30 cycles.

The wrinkles could be combined with other structures to form a hierarchically structured surface to enhance the optical switching performance such as lowering the transmittance, multistate tunability, and combined structural color. For example, Cao et al. combined wrinkling with high-aspect-ratio ridges to form a hierarchical surface on Au films through release of extreme biaxial strain of 200% in the elastomer,[241] which results in an extremely low transmittance of 0.2%. Kim et al. fabricated a mechanoresponsive smart window consisting of wrinkles on top surface of PDMS film and a thin layer of embedded silica particles inside.[242] In contrast to conventional wrinkled surfaces with their monotonic transmittance change with increased strain, the hierarchical wrinkling structure can achieve a multistate tunability of transmittance, which increases first and then decreases with the increased applied strain. The decrease in transmittance was due to the secondary wrinkles and nanovoids caused by delamination of particles and PDMS interfaces. Similar multistate tunability could also be obtained by integrating nanopillar arrays on wrinkled surfaces.[243] The wrinkling wavelength was designed to match the pitch of PDMS pillar array, thus when the PDMS surface became wrinkled, the pillars would be tilted to cross each other. With the increased tensile strain, the sample changed from opaque to transparent with iridescent structural color to transparent without structural color. Similar optical transparency switch but with nonvanishing iridescent structure color is observed by Lin et al. in self-similar hierarchical wrinkles-based smart window (Figure 15k,l).[237] Through sequential prestrain release and plasma treatment, hierarchically wrinkled PDMS samples are generated with features ranging from microscale to nanoscale. Iridescent color and opaqueness require different surface feature size, therefore typically one phenomenon will dominate and the other one will be weakened. However, in hierarchical wrinkles, the authors showed that the hierarchical wrinkles display both opaqueness from the large microsize wrinkles and iridescent color from the small sub-micrometer wrinkles (Figure 15m). Restretching the hierarchically wrinkled PDMS leads to the reversible and repeatable switch from opaqueness (40% transmittance) to transparency (80% transmittance), resulting from the flattening of large wrinkles (Figure 15m). While a nonvanishing iridescent structural color occurs arising from the nondisappearing small wrinkles even at 50% strain (Figure 15m). Sometimes structural color is favored for aesthetics while for other applications structural color should be avoided by choosing proper feature sizes.

From the viewpoint of practical applications such as building envelope, the mechanical strain required to switch the opacity on-and-off of smart windows should be as low as possible in order to save the space or function in a limited space. In other words, a high strain sensitivity of transmittance is preferred. Currently, the smart window with highest strain sensitivity was composed of ZnO film on acrylic elastomer, whose transmittance could be modulated from 3% to 93% by 14% biaxial tensile strain.[244] The biaxial stretching and compression in this work generated a crack-free disordered labyrinth pattern. No cracking eliminates the light travel through the cracks. The disordered labyrinth micropatterns induced stronger light scattering. In contrast, another crack-free wrinkling case, the PVA film on PDMS substrate, with uniaxial wrinkling was not as good as the biaxial wrinkling one.

It is worthy to be noted that in addition to direct mechanical stretch, the mismatch strain between films and substrates in forming mechanoresponsive wrinkles can also be tuned through external stimulus. For example, Zeng et al. fabricated a moisture responsive wrinkling based smart window.[245] Uniformly crosslinked PVA film via shielding from oxygen during UV crosslinking was deposited on PDMS substrates. With moisture provided, PVA swells but PDMS does not, resulting in compression in PVA films causing wrinkling. After drying, the wrinkles vanish and ready for re-moisturizing. A high tunable transmittance range of 10%-90% was successfully achieved through moisture control. Other external stimulus that could induce wrinkling includes electricity[244,246,247] and temperature.[248]

4.2. Delamination Buckling Based Smart Window

Wrinkling occurs when the stiff film is perfectly bonded to the soft substrate. However, if the bonding is weak, buckling driven delamination of stiff films on soft substrates can occur. Upon the increase of compression in the film, it transits from localized blisters to similar periodic buckle-delaminated patterns over large areas as wrinkling. Compared to wrinkling, delamination buckling could accommodate much larger compressive strain and form higher aspect ratio structure.[249,250] The high aspect ratio feature of delamination buckling leads to extreme optical properties, makes it a promising candidate for smart window application.

Zang et al. first applied the crumpling and unfolding of graphene to tune the optical property through mechanical strain (**Figure 16**a–f).[251] Few layer graphene films grown on nickel films was transferred to the prestretching acrylic elastomer membrane with prestrain 200–400%. The transferred graphene only has weak bonding to the acrylic substrate. Thereafter, the biaxial prestrain in the substrate was sequentially released to induce the delaminated crumpling of graphene film (Figure 16d). At the relaxed state, the crumples resulted in an opaqueness with 30% transmittance at visible range. After stretching with 500% strain, the transmittance could be enhanced to 80% showing a reversible tenability of optical transmittance (Figure 16f). But the required strain of 500% is too large, making it challenging as an optical switching device.

Instead of using graphene film, Thomas et al. applied GO film to generate crumpling film (Figure 16g–l).[252] Compared to graphene, GO has lower transmittance loss per layer for achieving high transmittance optical device. The 20 nm thick GO film was deposited by drop-casting on biaxially prestretched silicone rubber (SR) substrate with 400% prestrain. After releasing the prestrain, flower-like folding pattern with blister and sharp folds was obtained with amplitudes of 4–5 µm

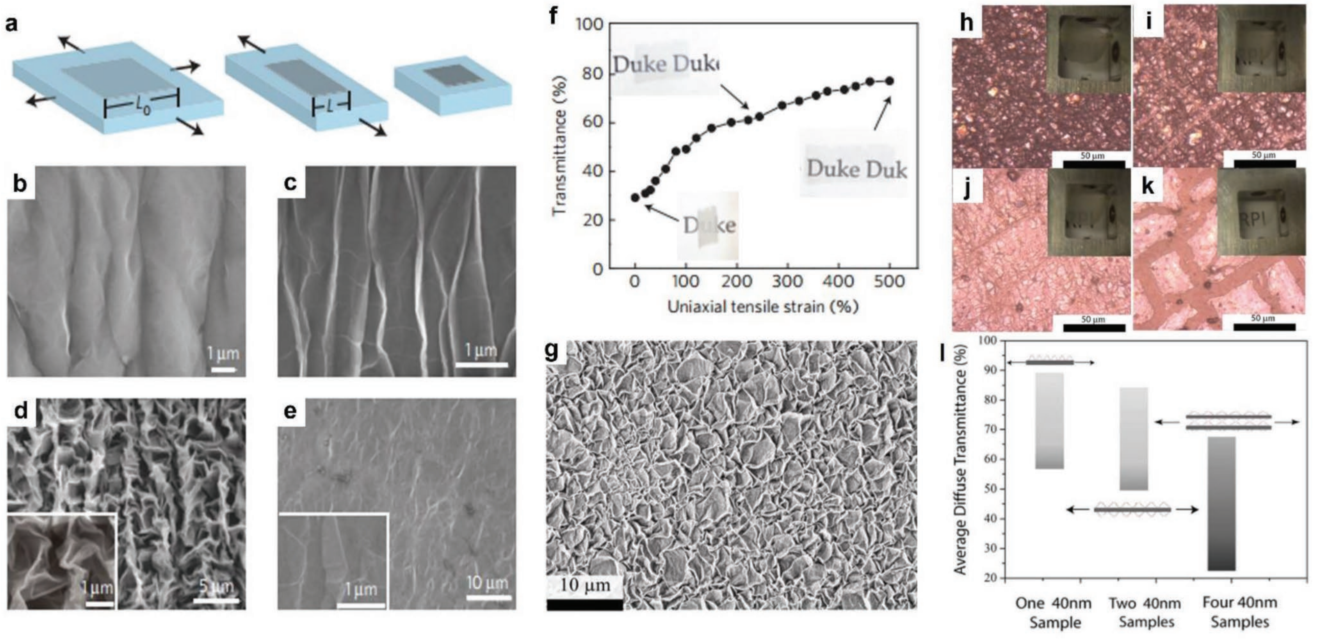

Figure 16. a) Schematic illustration of macroscopic deformation of graphene sheet on a biaxially prestretched substrate. SEM images of patterns developed on the graphene sheet: b) first wrinkles, then c) delaminated buckles, followed by d) crumples, which e) unfold as the substrate is biaxially stretched back. f) Transmittance in the visible range as a function of stretching strain. g) SEM image of the typical buckling pattern of GO film with prestrain 400%. Reproduced with permission.[251] Copyright 2013, Nature Publishing Group. Optical images of GO film during the transition from a fully crumpled to a fully flat state by applying stretching strain h) 0%, i) 200%, j) 300%, and k) 400%. l) Dynamic modulation range for average diffuse transmittance in the visible region for different layers of crumpled GO films. Reproduced with permission.[252] Copyright 2015, John Wiley & Sons.

and delaminated widths of 1–2 µm (Figure 16g). Figure 16h–k shows the structure evolution during applying tensile strain and corresponding optical transmittance. The crumpled GO film exhibited a very low normal transmittance of less 10%. Increasing applied biaxial tensile strains of up to 400% allowed for the normal transmittance to be varied from most opaque to most transparent state (90% transmittance). By stacking multilayer of crumpled GO film, the authors also achieved a controlled tunable range of diffuse transmittance. With single layer crumpled Go film, the tunable range of diffuse transmittance is from 60% to 90%. While with four layers crumpled GO film coupling together, the tunable range shift to 20–70% (Figure 16l). The stretching and releasing cycling were tested for over 100 times showing a neglectable degrade. Furthermore, the modulated transmittance through mechanical strains in most studied mechanoresponsive optical materials is only examined in the visible light range. For energy-saving smart window, the visible light (wavelength of 400–700 nm) only accounts for 44.7% of the solar energy while the near-infrared light (wavelength of 700–2500 nm) accounts for another 48.7% solar energy. Therefore, the authors also characterized the modulated normal transmittance of crumpled GO films on silicone rubber over the full spectrum with applied strain. At crumpled state, despite the low transmittance of below 10% for visible light, the average transmittance for NIR dramatically increase to over 30%. Thus, the transmittance over both visible and NIR range is needed for the MC smart window for energy-saving purpose. Similar crumpling of metallic glass film on PDMS substrates was studied by Xian et al. for tunable optical devices.[253] The semitransparent metallic glass film was deposited on biaxially prestretched PDMS substrate. Through crumpling and unfolding controlled by mechanical strain up to 84%, the transmittance could be tuned from 30% to 55%.

4.3. Kirigami Structure-Based Smart Window

Kirigami, close cousin of origami, is a paper cutting art by utilizing cutting or folding to realize 2D or 3D dynamically tunable structures.[254,255] The opening and closing of line cuts in kirigami structures make it a promising candidate for a new type of smart windows by letting light through or blocking light. Normally, patterned line cuts or slits are introduced to a thin sheet of materials. It will break the originally continuous thin sheet into discretely connected units. Upon stretching the kirigami sheet, the originally closed line cuts are open through out of plane buckling of the units between line cuts to let light in. The tilting orientation of the cut units can be dynamically tuned by the applied mechanical strain to interact with light in different incidence angles. Upon release of the mechanical strain, the popped 3D kirigami structure returns to 2D to close the pores to block the light.

Zhang et al. first proposed the application of kirigami structure for optical devices.[256] As shown in **Figure 17**a, a representative element consists of a reflective membrane in a square shape and two cuts. The two ends are bonded to a transparent, uniaxially prestrained PDMS substrate. The horizontally configured reflective membrane heavily blocked the incident light with only 30% transmittance left. Upon the releasing of prestrain in the PDMS substrate, the compressive buckling of

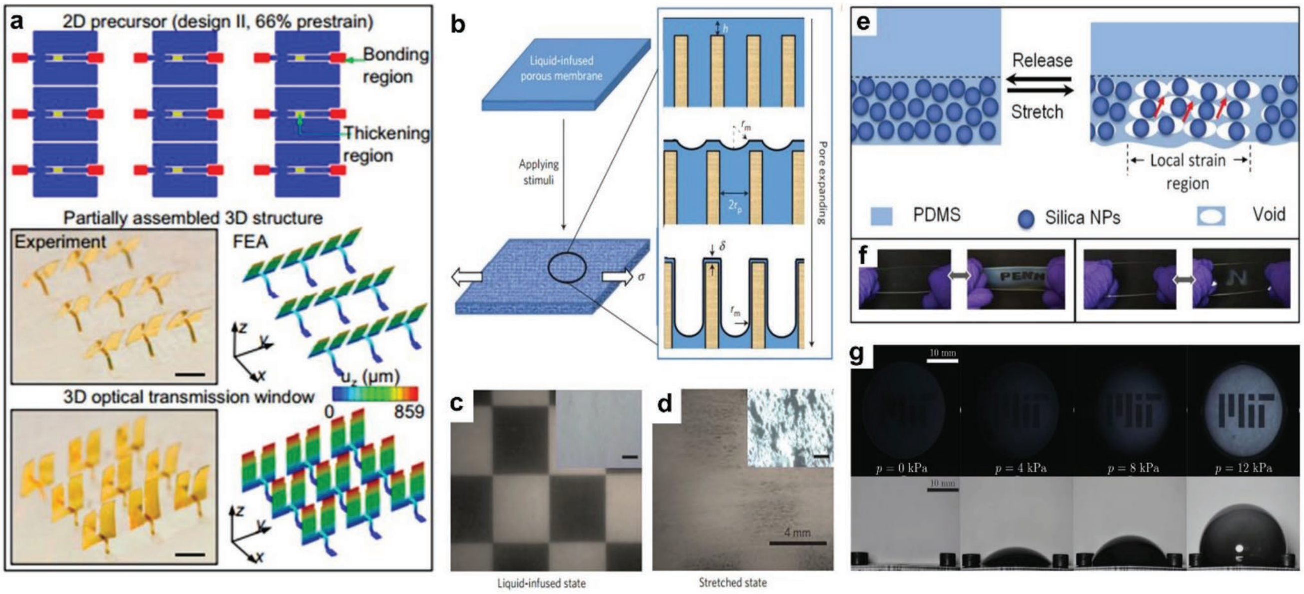

Figure 17. a) Schematic illustration of the kirigami structure and its regions of bonding (red rectangles) (top), optical images and finite-element analysis predictions of the intermediate state (middle) and final state (bottom). Reproduced with permission.[256] Copyright 2015, United States National Academy of Sciences. b) Scheme showing the concept of the fluid infused film on porous substrate. The photographs demonstrating the stretch-induced optical transmittance change before c) and after d) stretching. Reproduced with permission.[258] Copyright 2013, Nature Publishing Group. e) Schematic illustration of the void formation when stretched. f) Optical images showing reversible revealing and hiding of the letters. Reproduced with permission.[259] Copyright 2015, John Wiley & Sons. g) Top and side views as the internal pressure is progressively increased. Reproduced with permission.[260] Copyright 2016, John Wiley & Sons.

central ribbon rotated the reflective membrane upward, thus decreased the block of normal incident light. The maximum transmittance was reached when the rotation angle was 90°, which means that the reflective membrane was perpendicular to the transparent substrate. By carefully designing the structures, they achieved 90° rotation with 66% prestrain and a high transmittance of 97% was obtained after rotation. The buckling of kirigami structures can also be induced by direct tensioning. Tang et al. fabricated a programmable kiri-kirigami structure and investigated its potential application as a smart window for energy saving building through numerical simulation.[16,216] The kirigami structure in their work is a thin planar sheet material with patterned line cuts in centered rectangular arrangement. When under tensile strain, the beams in the kirigami structure will buckle out of plane and tilt. By introducing the prescribed notches, the individual local tilting orientations of the cut units can be controlled in a programmable fashion. Thus, it can potentially reflect either indoor or outdoor light in selected regions for improved personalized local comfort. Numerical simulations were conducted to explore the effect of kirigami structure on reflecting and redirecting the sunlight for building energy saving. The results showed that the kirigami envelope diffuses the daylight more evenly and redirect the light, which can help to save electricity by 26% on a yearly basis.

The lowest and highest transmittance are the key parameters for designing a mechanoresponsive smart window. In general, high aspect ratio features, hierarchical structures, and high integrity of the film (no cracking or other slits) could lower the transmittance. To date, the lowest transmittance reported could drop to nearly 0%.[241,257] The highest transmittance is highly dependent on constituent materials itself. Any materials will absorb certain amount of light, therefore even those works using highly transparent materials such as PDMS and acrylic could only get around 90% transmittance with still 10% loss. However, the kirigami structures-based smart window could achieve as high as 97% transmittance when the cut unit rotates to be parallel to the light incident direction by minimizing the loss from material adsorption, which is another unique advantage of kirigami structures-based smart window.

4.4. Other Strategies

In addition to light scattering, reflecting, and redirecting through interacting with structured or nonstructured surfaces, other strategies for tuning optical transmittance have been demonstrated through light interaction with microstructures embedded inside optical materials.

Yao et al. developed an adaptive liquid-infused porous film with tunable optical transparency made of liquid film supported on porous elastic substrate (Figure 17b–d).[258] The liquid infused porous film is transparent (Figure 17c). As the substrate was stretched, the pores expanded and the liquid retreated into the expanded pores, causing the original smooth liquid film surface to become roughen (Figure 17b), thus the partially air-filled pores made the film become opaque (Figure 17d). Rather than infusing liquid in porous materials, Ge et al. embedded silica NPs in PDMS matrix to form mechanoresponsive composite optical materials for smart window.[259] Initially, the prepared composite sample was transparent with 90% transmittance. After stretching, the NPs became delaminated from the PDMS matrix due to the weak interface bonding, resulting in the formation of microvoids inside the composite as shown in Figure 17e. The voids exhibited significantly different refractive index with silica particle and PDMS, thus causing a dramatic drop in transmittance (Figure 17f). When applied with 100% tensile strain, the transmittance could be reduced to 30%. In addition, the silica NPs also induced angle-independent structural color upon stretching. The structure color can be tuned by the NP size from blue, green to yellow. Similar PDMS–microparticle composites are proposed by López Jiménez et al.,[260] for tunable optical transmittance through mechanical stretching and pneumatic bulging (Figure 17g). By reorientating the polydomain in liquid crystal elastomers (LCE) through deformation, Wang et al. developed a reversible MC LCE-based optical device.[257] When subjected to mechanical stretching, the original opaque polydomain in LCE can transform to transparent monodomain, thus achieving tunability on transmittance.

4.5. Brief Conclusion

A recent progress of mechanoresponsive smart windows is covered in this section, also summarized in **Table 3**. To achieve an opaque/invisible state, the incident light could be either reversibly blocked by macroscale structures or scattered by microscale structures of smart windows. Based on the deformation strategies, some of them were designed to “display” when stimulated by mechanical strain while others were supposed to “hide” under strain. To date most mechanoresponsive smart windows developed were based on surface instability such as wrinkling and buckling-induced delamination while novel strategies with promising and exciting performances are also emerging. In order to facilitate the commercialization of mechanoresponsive smart window, several challenges still need to be overcome. Applied biaxial strain over 10% is still too large for practical smart window applications considering its over 21% area expansion due to the stretching. New strategies which allow large transmittance modulation via small strain (less than 5%) are still highly desired. Furthermore, so far only one research tested the mechanical robustness of such mechanoresponsive optical materials at the level of 10^5 cycles of mechanical stretching/releasing without degradation in optical performances.[234] Most researches only tested a fatigue life of thousands or hundreds cycles of mechanical stretching and releasing. Despite the demonstrated benefits of microcracks in wrinkling and folding of thin films for enhancing the optical properties, the fatigue life of cracks under high level of mechanical loading cycles without catastrophic structural failure may present an issue for designing smart windows.

5. Photochromics

PC materials change color when exposed to certain wavelengths of light, which is a reversible process. Similar to TC window, PC devices allow simple fabrication without extra energy input. Generally, PC smart window is made by embedding active

Table 3. Summarization of mechanoresponsive smart windows reported in literature.

Deformation mechanism$^{a)}$		Characteristic feature size	Performance	Cycling performance	Ref.
Wrinkling based	Wrinkling on PDMS	Wrinkles: wavelength 4–5 µm amplitude 1.2 µm	Opaque @ $\varepsilon = 0\%$ to Transparent @ $\varepsilon =$ prestrain value to opaque @ $\varepsilon = 50\%$	100 000 cycles with no noticeable change in optical property	[234]
	Orthogonal wrinkling and cracking	Wrinkles: wavelength 90 µm amplitude 9 µm; cracks: density 7 mm^{-1} at 50% strain crack depth 16.6 µm	$T_{\mathrm{n,v}} = 92\%$ @ $\varepsilon = 0\%$ to $T_{\mathrm{n,v}} = 9.2\%$ @ $\varepsilon = 50\%$	1000 cycles with a few new cracks generated	[238]
	Ag deposition on wrinkling PDMS	Wrinkles: wavelength 6 µm	$T_{\mathrm{n,v}} = 9.48\%$ @ $\varepsilon = 0\%$ to $T_{\mathrm{n,v}} = 45.27\%$ @ $\varepsilon = 30\%$	–	[261]
	Wrinkling of PVA on PDMS	Wrinkles: wavelength 120 µm amplitude 16.2 µm	$T_{\mathrm{n,v}} = 6\%$ @ $\varepsilon = 0\%$ to $T_{\mathrm{n,v}} = 91\%$ @ $\varepsilon = 20\%$	2000 cycles with no degradation	[235]
	Biaxial wrinkling of ZnO on acrylic membrane	Wrinkles: wavelength 10 µm amplitude 1 µm	$T_{\mathrm{n,v}} = 3\%$ @ $\varepsilon = 0\%$ to $T_{\mathrm{n,v}} = 93\%$ @ $\varepsilon = 14\%$	30 cycles with no degradation	[236]
	Ridges and small wrinkles of gold film on acrylic membrane	Ridges: wavelength 8 µm amplitude 2–4 µm; Wrinkles: wavelength 100–160 nm	$T_{\mathrm{n,v}} = 0.2\%$ @ $\varepsilon = 0\%$ to $T_{\mathrm{n,v}} = 54.3\%$ @ $\varepsilon = 70\%$	–	[241]
	Wrinkles on top of PDMS film; silica particles embedded inside	Wrinkles: wavelength 2.3 µm amplitude 190 nm; particles: diameter 200 nm	$T_{\mathrm{n,v}} = 60.5\%$ @ $\varepsilon = 0\%$ to $T_{\mathrm{n,v}} = 86.4\%$ @ $\varepsilon = 10\%$ to $T_{\mathrm{n,v}} = 40\%$ @ $\varepsilon = 30\%$	–	[242]
	Pillars on wrinkles	Wrinkles: wavelength of 2.4 µm amplitude of 750 nm; pillars: diameter 1 µm pitch 2 µm height 4 µm	$T_{\mathrm{n,v}} = 40\%$ @ $\varepsilon = 0\%$ to $T_{\mathrm{n,v}} = 70\%$ with iridescent color @ $\varepsilon = 30\%$ to $T_{\mathrm{n,v}} = 80\%$ @ $\varepsilon = 40\%$	After 50 cycles, the maximum transmittance decreased due to formation of cracks and defects	[243]
	Self-similar hierarchical wrinkles	Large wrinkles: wavelength 3–5 µm amplitude 345 nm; small wrinkles: wavelength 400–950 nm amplitude 125 nm	$T_{\mathrm{n,v}} = 40\%$ with iridescent color @ $\varepsilon = 0\%$ to $T_{\mathrm{n,v}} = 80\%$ with iridescent color @ $\varepsilon = 30\%$	100 cycles with minor extra cracks	[237]
Delamination buckling based	Crumpling graphene with 1D or 2D ridges	Ridges: wavelength 0.2–2 µm	$T_{\mathrm{n,v}} = 30\%$ @ $\varepsilon = 0\%$ to $T_{\mathrm{n,v}} = 80\%$ @ $\varepsilon = 500\%$	50 cycles with no change in performance	[251]
	Crumpling GO film	Ridges: delaminated widths 1–2 µm amplitude 4–5 µm	$T_{\mathrm{n,v}} = 10\%$ @ $\varepsilon = 0\%$ to $T_{\mathrm{n,v}} = 90\%$ @ $\varepsilon = 400\%$	100 cycles showing a neglectable degradation	[252]
	Crumpling metallic glass film	Ridges: widths 200 nm	$T_{\mathrm{n,v}} = 30\%$ @ $\varepsilon = 0\%$ to $T_{\mathrm{n,v}} = 55\%$ @ $\varepsilon = 84\%$	–	[253]
Rotation of Kirigami structure		Up to 90° rotation at 66% strain	$T_{\mathrm{n,v}} = 30\%$ @ $\varepsilon = 0\%$ to $T_{\mathrm{n,v}} = 97\%$ @ $\varepsilon = 66\%$	No failure after 150 cycles at 0.04 Hz	[256]
		30° rotation	26% energy saving when used as building envelope	–	[216]

Table 3. Continued.

Deformation mechanism[a)]	Characteristic feature size	Performance	Cycling performance	Ref.
Fluid infused porous film	Pore diameter 200 nm	Transparent @ $\varepsilon = 0\%$ to Opaque @ $\varepsilon = 13.3\%$	–	[258]
Silica NPs embedded inside PDMS	Particle diameter 200–300 nm	$T_{n,v} = 90\%$ @ $\varepsilon = 0\%$ to $T_{n,v} = 30\%$ with angle-independent color @ $\varepsilon = 100\%$	1000 cycles with no degradation	[259]
Orthogonal cracks and folds of PVA film	Average crack distance 24 µm, crack depth 1.5 µm; average fold distance 70 µm, depth 12 µm	$T_{n,v} = 85\%$ @ $\varepsilon = 0\%$ to $T_{n,v} = 30\%$ @ $\varepsilon = 50\%$	Over 50 000 cycles with no significant degradation	[239]
Switch between polydomain and monodomain of liquid crystal elastomer	–	$T_{n,v} = 0\%$ @ $\varepsilon = 0\%$ to $T_{n,v} = 80\%$ @ $\varepsilon = 150\%$	10 cycles showing no degradation	[257]
Pneumatically expand a cavity made of PDMS mixed with black dyes	–	Increased transmittance with increasing pneumatic pressure	10 cycles showing no degradation	[260]

[a)] Note: $T_{n,v}$ is the average normal transmittance in visible range, and ε is the applied mechanical strain.

materials into transparent host matrices followed by coating on a transparent substrate. For an ideal PC smart window, a high coloration contrast is desirable for a good solar energy modulation together with fast reversible switching speed and high photochemical stability to ensure practicability for building section applications. It is important to note that PC smart window is not desirable in four seasoned countries as even in winter, the colored state will block the sunlight. This section reviews some important types of organic and inorganic PC materials.

5.1. Organic Photochromic Molecules and Polymers

Organic PC materials undergo a photoinduced structure transition between two chemical isomers with different absorption spectra. During the transformation process of the molecules, the chemical bond rearrangement results in structural and electronic changes. There are many groups of organic molecules that exhibit photochromism, most commonly known as fulgide, diarylethene, spiropyran, spirooxazine, naphthopyran (chromene), azobenzenes, and their polymers.[23] Although all the organic PC materials will experience the colorization process upon the irradiation of UV, the color of material cannot be switched back by simply removing the UV. According to the bleaching method, the organic PC material can be categorized into two groups, namely thermal irreversible PC materials and thermal reversible PC materials. The thermal irreversible PC materials turn back to its original color by exposing under the visible light. On the other hand, thermal reversible PC materials are usually thermally unstable, and their bleaching process can be triggered by heating or irradiation with visible light.[262,263]

Only diarylethenes and fulgide derivatives exhibit thermally irreversible photochromism, their acquired coloration after UV exposure does not fade in the dark, which make them suitable for applications such as optical memories, optical switching devices and displays.[264] Diarylethenes undergoes a photocyclization reaction upon the UV exposure, due to its structure change.[262] As a result, the color of the material changes from colorless to red. Li et al. developed four types of PC diarylethenes with different amount of benzofuran and benzene moieties attached (namely, diarylethenes 1 to diarylethenes 4, respectively) that showed excellent photochromism.[264] As shown in **Figure 18**a, all diarylethenes 1 to 4 in hexane are colorless at original state (1o–4o), and after exposure to UV light, diarylethenes 1 turn to purple (1c), while diarylethenes 2–4 turn to orange (2c–4c).

Different from the diarylethenes, photochromism of fulgide family materials is based on the reversible photochemical conrotatory electrocyclization of the 1,3,5-hexatriene moiety, such as furoyl- and indolylfulg(im)ides.[265] Exposure furylfulgides solution to irradiation with UV light converts the stable E-form (typically pale yellow) into the strongly colored C-form (typically red) via a 6 π-electrocyclization.[266] As shown in Figure 18b, during this process, E-form crystals first start turn to C-form under UV light exposure, and the mixed crystals keep the lattice structure of reactant in the early stages of the photoreaction. In this stage, the lattice mainly consists of E-form, and a small amount of C-form is presence. With the reaction going on, more E-form is converted into C-form. As C-form exhibit different crystal lattice to E-form, crystals with high C-form concentration separated from the mixed phase crystal and change the color.

In contrast, the thermally reversible PC isomers, including spiropyrans, spirooxazines, azobenzenes, and naphthopyrans are thermally unstable.[262,267] Their bleaching process can be triggered by either expose under the visible light or heating. For

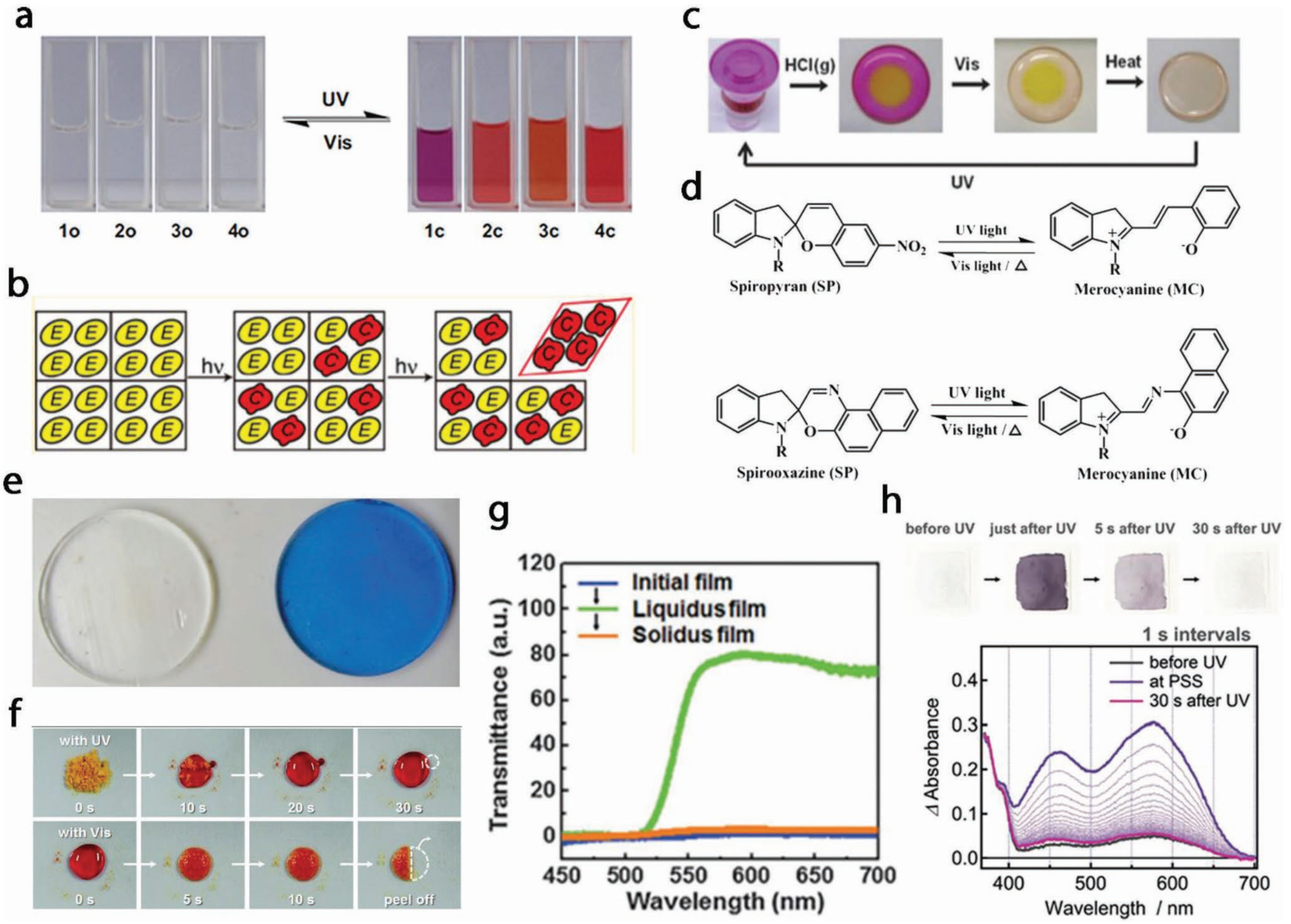

Figure 18. a) Color changes of diarylethene (1–4) in hexane at room temperature. Reproduced with permission.[264] Copyright 2014, Elsevier. b) Progress of the PC reactions of furylfulgide crystals focusing on the crystal lattice and its disruption. Reproduced with permission.[266] Copyright 2017, American Chemical Society. c) Chromatic changes of a UV-irradiated spiropyran containing the PDMS film. Reproduced with permission.[269] Copyright 2014, Royal Society of Chemistry. d) Chemical structure of spirooxazine (above) and spiropyran (bottom). Reproduced with permission.[271] Copyright 2017, Molecular Diversity Preservation International and Multidisciplinary Digital Publishing Institute. e) Spirooxazine before (left) and after (right) UV irradiation. Reproduced with permission.[274] Copyright 2013, Scientific Research. f) Photoinduced solidus to the liquidus phase transition of CAz-OH crystal under UV light irradiation for 20 s (above) and subsequent liquidus to the solidus phase transition of CAz-OH liquid by irradiating Vis light for 10 s (bottom). g) its corresponding light modulating efficiency. Reproduced with permission.[272] Copyright 2015, Royal Society of Chemistry. h) Color change and Transient absorption spectra of the triblock copolymer film doped with 7MR-Y and 5MR-B upon irradiation with light from a solar simulator and that after ceasing light irradiation. Reproduced with permission.[273] Copyright 2019, John Wiley & Sons.

spriopyran, the structural change between a closed spiropyran form (colorless) and an open merocyanine form (purple) which can be triggered by light, pH, pressure, and so forth.[268] Under UV irradiation, spiropyran-embedded PDMS film changed color from clear to purple, while the purple colored film changed to yellow once exposed to HCl gas (Figure 18c).[269] Spirooxazine has a similar ring opening process as spiropyran under UV exposure (Figure 18d), which has been widely studied due to its high fatigue resistance among different PC dyes.[270] As shown in Figure 18e, spirooxazine is colorless in its closed ring form and becomes blue under UV irradiation (open ring form).[271]

Azobenzene (and its derivatives) undergo trans-cis photoisomerization when exposed to the UV. The azobenzene-based PC material shows opposite PC properties compared with other PC materials. The material is opaque at its original state, while switches to transparent under UV exposure.[272] As shown in Figure 18f, opaque yellow color azobenzene-based photoresponsive amphiphilic molecule (CAz-OH) powders turned to red transparent liquid droplet fast under UV exposure. Subsequently, by removing the UV light was and irradiating visible light on the droplet, the CAz-OH liquid droplet immediately returns to the solidus state within 10 s. Figure 18g shows that the transmittance of CAz-OH liquid status is about 40 times higher than that of the initial solidus film.

PC naphthopyrans can be divided into two subgroups: the 3*H*-naphtho[2,1-*b*]pyran (3*H*-NP) and the 2*H*-naphtho[1,2-*b*]pyran (2*H*-NP) families. In general, molecules from the 2*H*-NP families have more stable colored forms than the corresponding 3*H*-NP molecule, while 3*H*-NPs have much faster thermal bleaching than 2*H*-NP's together with a much lower ΔOD (difference in absorption between dark and bleached states, measured at λ_{max}).[262] Recently, Kuroiwa et al. reported an on-demand control of the decoloration speed of the transient colored species of naphthopyran derivatives (3H-NP family), which is able to apply for PC lenses, smart windows, and dynamic holographic materials usage.[273] As shown in Figure 18h, under irradiation light, the film changes from colorless to grey. Once the light removed, the grey color rapidly decays to colorless with a similar time constant. Such on-demand control makes naphthopyrans responsive to the irradiating and removing of the UV at room temperature.

5.2. Inorganic Photochromic Materials

The frequently reported inorganic PC material includes transition metal oxides (TMOs), such as WO_3,[275] TiO_2,[276] MoO_3,[277] V_2O_5,[278] and Nb_2O_5,[279] metal halides,[280] and rare-earth complexes.[281] Although metal halides and rare-earth complexes are widely used as PC lenses,[282] optical switches,[283] and optical storage media,[284] TMOs material is preferred for large-scale application such as smart windows due to its the good stability and cost efficiency.[285] WO_3 and TiO_2 are the most intensively discussed TMOs PC materials. The photochromism principle of WO_3 is the interval electron transfer between tungsten ions with different valence states. Upon the irradiation of light, pair of electron and hole is formed in WO_3 film. The hole will react with the water that absorbed on the surface of WO_3, forming hydrogen ions. The hydrogen ions, electron, and WO_3 will further react to form the H_xWO_3 compound and change the color of the film.[285] The formulae below show the chemical reactions in this process

$$WO_3 + h\nu \rightarrow WO_3^* + e^- + h^+ \tag{1}$$

$$h^+ + \frac{1}{2}H_2O \rightarrow H^+ + \frac{1}{4}O_2 \tag{2}$$

$$WO_3 + xe^- + xH^+ \rightarrow H_xWO_3 \tag{3}$$

The performance of pristine WO_3 is limited due to its poor revisability, low PC activity, and narrow photochromism response range.[286] Therefore, several strategies such as morphology modification,[287] elemental doping,[288] and composite forming[289] have been implemented to tackle this issue. Adachi et al. reported a WO_3/silicon oxycarbide/silica hybrid xerogel with high transparency, promising PC properties, and investigated its color switching response process.[290] In this composite material, 3-(triethoxysilyl)propyl methacrylate (TESPMA) and tetraethoxysilane (TEOS) were used to form the xerogel matrix, and WO_3 NP was evenly dispersed into the matrix. Meanwhile, Li_2SO_4 was introduced to prompt the reduction of W^{6+} colorless ion to W^{5+} blue colored ion by compensating the negative charge that produced during the reduction reaction. The prepared composite was colorless and transparent in the dark environment. Upon the irradiation of the UV, the material changed to blue color (**Figure 19**a). Figure 19b shows the time-elapsed absorption spectra of the hybrid xerogel. With the increasing of irradiation time, two absorption peaks located at 640 and 940 nm appeared. The formation of absorption peaks was due to the intervalence charge transfer between W^{5+} and W^{6+} ions.

Recently a new approach was reported to improve the PC sensitivity and efficiency of tungsten oxides. The researchers fabricated a multilayered structure that overcoats $Y_2SiO_5:Pr^{3+}$ film on $H_3PW_{12}O_{40}$ film.[291] The $Y_2SiO_5:Pr^{3+}$ is the phosphor material that converts visible light in the solar light into UV light. Because the larger intensity of UV irradiated on the PC on $H_3PW_{12}O_{40}$ film, the coloration rate of $H_3PW_{12}O_{40}$ film was largely accelerated by seven times compared to the pristine $H_3PW_{12}O_{40}$ film. (Figure 19c,d) Moreover, the PC process can be triggered by the lower intensity of UV compared to conventional tungsten oxide–based film.

On the other hand, TiO_2 is another type of highly competitive PC material due to its abundance and nontoxic. Currently, TiO_2 NPs and TiO_2 gels are the two forms of TiO_2 that show the photochromism.[292,293] Similar to the WO_3, the PC response of TiO_2 is attributed to the light-induced redox reaction of Ti^{4+} ion. Once absorbing the photon, the electron-hole pair will be formed in TiO_2. The electron will subsequently reduce the Ti^{4+} ion and produce the colored Ti^{3+}. Such reactions can be described by the formulae below

$$TiO_2 + h\nu \rightarrow e^-_{CB} + h^+_{VB} \tag{4}$$

$$e^-_{CB} + Ti^{4+} \rightarrow Ti^{3+} \tag{5}$$

Joost et al. recently reported a TiO_2 NPs/butanol PC system that able to achieve the 100–0% transmittance switching over a broad wavelength range (400–12 000 nm).[294] As shown in Figure 19e, the initial state of the hybrid system is a yellow-colored transparent liquid; upon the irradiation of UV, the liquid turned into black color. However, the color of the liquid cannot be switched back by removing the UV radiation. To switch the liquid back to its original state, air (or oxygen) needs to be injected into the liquid to oxidize black colored Ti^{3+} ion back to Ti^{4+} ion. The color changing can take place within 15 minutes for both visible and IR wavelength (Figure 19f,g). With increasing irritation time, the absorption increases resulting in reduced transmission. The authors pointed out that the color switching mechanism for the visible and IR range was different. In the visible range, the changing of absorption is due to the polaronic lattice distortions in the NPs while the IR transmittance switching is caused by the photoreduction of TiO_2.

5.3. Brief Conclusion

Both organic and inorganic PC materials were introduced and discussed in this chapter. Their name, type, photochromism principle, method of bleaching, and color change are summarized in **Table 4**. From the table, it can be concluded that the organic PC material shows variable color change. However, except the naphthopyran, the majority of the organic PC materials cannot turn to their original color by simply removing the UV. Such a shortcoming restricts their application as smart window. On the other hand, many inorganic PC materials

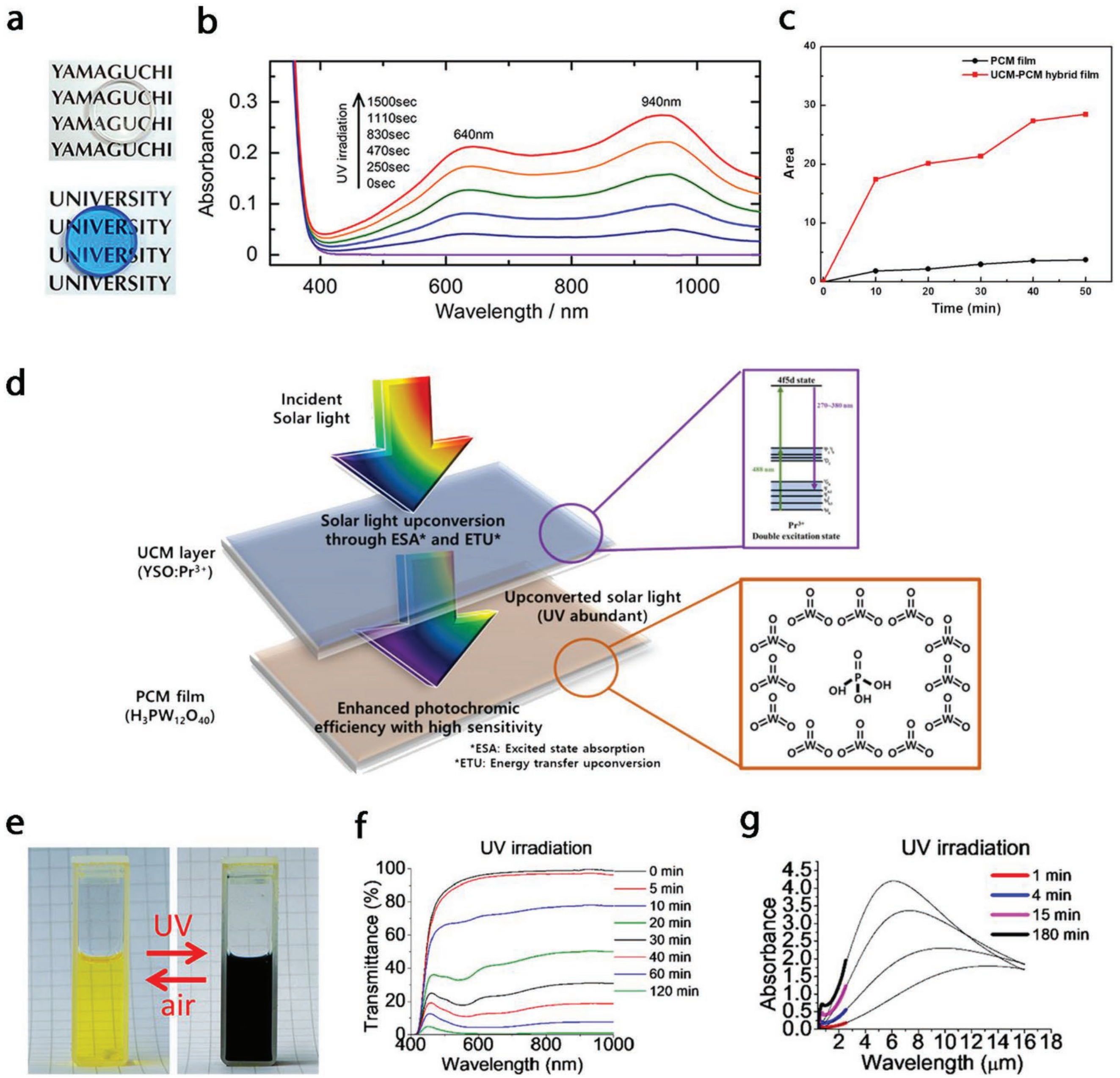

Figure 19. a) Photo of transparent as-prepared (above) and colored (below) WO_3/TESPMA/TEOS hybrid xerogels. b) Absorption spectral change of the WO_3/TESPMA/TEOS hybrid xerogel containing Li_2SO_4 upon UV irradiation at 25 °C. Reproduced with permission.[290] Copyright 2016, American Chemical Society. c) Total amount of absorbed visible light (400–800 nm) versus solar light irradiation time for hybrid film (red) and pristine tungsten oxide film (black). d) Scheme on the PC process of Y_2SiO_5:Pr^{3+}/$H_3PW_{12}O_{40}$ hybrid film. Reproduced with permission.[291] Copyright 2018, American Chemical Society. e) Photo of transparent (left) and colored (right) anatase TiO_2 NPs/butanol system. f) Optical response of TiO2 NPs to UV irradiation. g) Optical response of TiO_2 NPs to air oxidation. Reproduced with permission.[294] Copyright 2018, American Chemical Society.

are able to switch color by irradiating/removing the UV light. Therefore, the color of inorganic PC material-based smart window can be easily controlled by the change of light intensity. Although the color change for the inorganic PCc material is mainly limited to colorless/white to blue, it is more suitable for employing as smart window in current stage due to the less restriction on bleaching process and better durability Compared with the other three categories of smart windows, more fundamental research could be conducted to enrich this library of photochromism to suit the requirement of energy-saving smart windows.

6. Conclusion and Perspective

The review systematically summarizes the recent progress of smart windows from electro-, thermo-, mechano-, to photochromics. We conclude the strategies and working mechanisms

Table 4. Principles and performance summary for organic and inorganic photochromic materials.

Type of the material		Name of material	Photochromism principle	Method of bleaching	Color change	Ref.
Organic		Diarylethenes	Photocyclization reaction	Expose to visible light	Colorless → red	[262]
		Fulgide	Photochemical conrotatory electrocyclization	Expose to visible light	Pale yellow → red	[265]
		Spriopyran	Heterolytic cleavage/ photocyclization	Expose to visible light/heating	Colorless → purple	[268]
		Spirooxazine	Heterolytic cleavage/ photocyclization	Expose to visible light/heating	Colorless → blue	[271]
		Azobenzene	*Trans–cis* photoisomerization	Expose to visible light/heating	Opaque yellow → transparent Red	[272]
		Naphthopyran	Heterolytic cleavage/ photocyclization	Removing UV	Colorless → gray	[273]
Inorganic	TMOs	WO_3	Photon prompted redox reaction	Removing UV	Colorless → blue	[275,290]
		TiO_2	Photon prompted redox reaction	Removing UV and expose to air	Light yellow → black	[294]
		V_2O_5	Photon prompted redox reaction	Removing UV	Yellow → green	[295]
		MoO_3	Intercalation–deintercalation of univalent cations	Removing UV	White → blue	[277,296]
		Nb_2O_5	Photon prompted redox reaction	Expose to air	Colorless → blue	[279]
	Metal halides	Lead chloride $[Pb_3Cl_6(CV)]\ H_2O]n$	Light-triggered electron transfer	Remove UV/anneal in air	Pale yellow → blue	[280]
		AgCl	Light-triggered reversible decomposition	Remove UV	Transparent → brown	[282]
	Rare-earth complexes	Rare earth–doped barium haloapatite $Ba_5(PO_4)_3Cl{:}Eu^{2+},R^{3+}$ (R = Y, La–Nd, and Sm–Lu)	Light-triggered electron transfer	Expose to green light/heating	White → pink	[281]

for each category focusing on different materials and techniques for performance improvement. We also discuss the derived multifunctional devices based on the electro- and thermochromic technologies. Brief conclusions of the four categories are provided at the end of each section. In this section, we comment on these smart windows and outline the challenge and future development in the area.

The brief comparison between these four categories of smart window is presented in **Table 5**. The electro- and mechanochromics are classified to be active methods, while the thermal- and photochromics that respectively respond to surrounding temperature and light intensity are commonly recognized as passive modes, even though some integrated methods, such as electrothermal technology, may assist with both modes. The electro- and mechanochromic windows are believed to be more complex than the other two because they require either the electric or mechanical control systems. Moreover, the electrochromics often employ a sandwich structure composed of several layers with different materials, thus, it increases the device complexity. As to the transition speed, all these technologies are able to achieve the optical switch in less than a few seconds, which is considered to meet the most practical demands in smart windows.

Challenges remain for the future development of smart window technology to be fully utilized in the buildings. Even though some pristine smart windows have been

Table 5. The brief comparison of electro-, thermo-, mechano-, and photochromic windows.

	Electrochromics	Thermochromics	Mechanochromics	Photochromics
Actuation	Active	Passive	Active	Passive
Stimuli	Electrical	Thermal	Mechanical	UV light
Device complexity Degree	High Multilayered structure, electric control system is required	Low Simple coating or encapsulation	Medium The mechanical control system is required	Low Simple coating or encapsulation
For energy-saving windows	Suitable, with one-time low energy input	Suitable	Suitable with additional control	Suitable for tropic countries
Optical transition speed	Acceptable	Acceptable	Acceptable	Acceptable

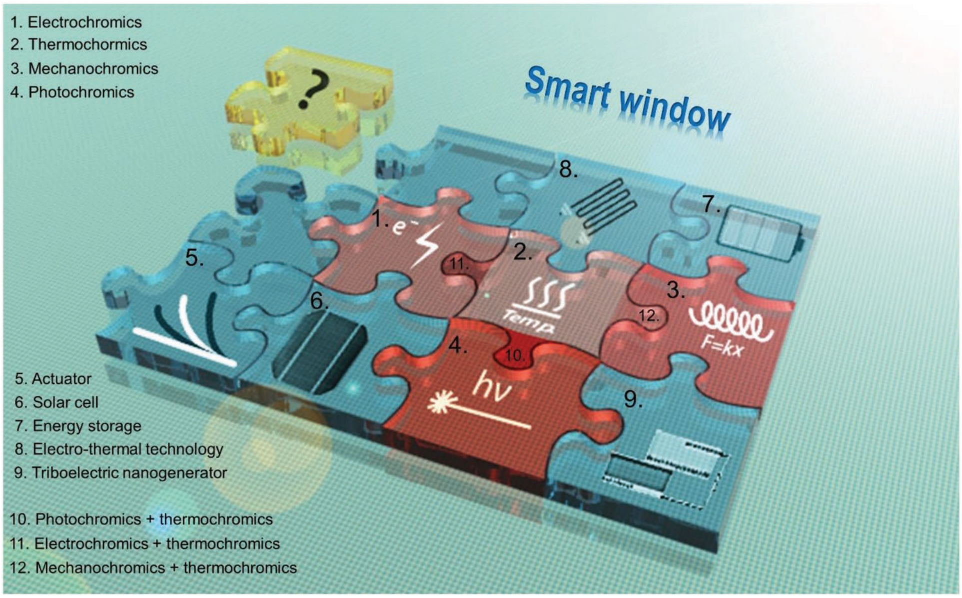

Figure 20. Illustration of the four optical modulation modes, the multifunctional technologies, and other potential technologies.

commercialized, some technical and economic hurdles prevent them from widespread adoption. 1) High cost. The payback period must be considered and the market analysis suggests that the acceptable payback period are 12 and 22 years for residential and commercial buildings, respectively.[26,297] Additional cost comes from installation, maintenance, repair, and so on. The new materials and or process may revolutionize the ways of window installation and maintenance to potentially lower the cost. Moreover, it is worthwhile to optimize the device design toward robust and simple structures for more cost-effective products. 2) Durability. The commercial energy-saving smart windows have to be highly durable for long-term service, which imposes stringent requirements for the durability of materials and devices. A better understanding of the material transition is critical to promote the performance and enhance the stability in terms of materials, structures, and optical performances. 3) Energy-saving maximization. Optimizing the solar modulation properties is the key to energy saving. There is no unified index to assess the energy-saving performance, for example, in thermochromic system, the T_{lum} and ΔT_{sol} are commonly used as reliable and comprehensive index to gauge the energy modulation. Considerations on solar heat gain coefficient are often important for electrochromics smart windows. More comprehensive energy calculation via multi-interdisciplinary collaborations are needed to understand the complex heat transfer mechanisms and translate the optical response to the real energy consumption in the buildings. It is worthy to mention that the haze effect dramatically affects the appearance of objects viewed through windows by scattering. Though a few works have discussed this effect,[19,20] it is generally overlooked by most researchers in the smart windows fields. It is believed the haze effect is notable on films with dispersive particles of size near or larger than visible wavelength, such as the smart windows based on the hydrogels,[126] liquid crystals,[6] inorganic particles,[158] and on films with rough surface with characteristic dimension of around/larger than several hundred nanometers, such as smart windows based on wrinkles,[237,238] cracks,[238] and surface patterns.[140,150] Thus, it is suggested to consider the haze effect when discussing the transparency and energy-saving performance.

Future development can continue to break the boundaries among different modes of stimuli as well as integrate the smart window technologies with other functionalities to fully utilize the large surface area provided in urban windows, i.e., next generation of multifunctional smart window (**Figure 20**). One of the recent trends is to rationally combine the different stimulus to further enhance chromic window performance. For example, the combination of thermochromic VO_2 with mechanical reconfigurable structures renders much enhanced performance.[152] Considering the large area of windows in the modern skyscrapers, the multifunctional device for energy harvesting, storage, and conversion are certain to be the trend for future development, which makes it more compelling to the market for economizing the energy bill. In addition, adding other functionality to the surface of smart window will add extra values for the smart window productions beyond the energy saving, e.g., superhydrophobicity for self-cleaning window,[128,139] energy storage electrochromics,[3] water harvesting and storage from the environment for addressing the water scarcity in arid regions,[298,299] anti-icing,[300–302] etc. The inevitable challenges lie in balancing the luminous transmission, transparency, energy saving, device performance, and durability.

Another interesting trend is to develop smart windows with novel light modulation and different stimulus beyond the current four more mature technologies, for example, the use of gasochromics, application of humidity-responsive materials with light modulation,[303,304] and the incorporation of the fluid system for smart windows.[305–307] These studies are in early stages which need extensive investigations prior to commercialization. Additional new stimulus to switch the transmittance of the windows may be of great interest to the research community (Figure 20).

The smart window is a highly interdisciplinary technology. By reviewing the recent progress of materials science in a broad picture, we expect this summarized work may accelerate the development of smart windows which can regulate heat favorably and promote multifunctional devices to collect, storage, and convert energy. Other functionalities such as privacy control, entertainment, and sensing are possible and attractive to be integrated into windows (Figure 20). The great potential of this highly interdisciplinary research is foreseen to have high social impact in the near future.

Acknowledgements

Y.K., J.C., and G.L. contributed equally to this work. Y.L., P.S.L., and J.Y. proposed the manuscript. Y.K. drafted and Y.L. revised the abstract, 1) Introduction, 3) Thermochromics, and 6) Conclusion and Perspective. J.C. drafted and P.S.L. revised the 2) Electrochromics. G.L. drafted and J.Y. revised the 4) Mechanochromics. S.W. and Y.Z. drafted and Y.L. revised the 5) Photochromics. Y.L., P.S.L., and J.Y. revised the manuscript and the perspectives. Y.L. and P.S.L. thank for the funding support by the National Research Foundation, Prime Minister's Office, Singapore, under its Campus for Research Excellence and Technological Enterprise (CREATE) programme. Y.L. also thanks the Singapore Ministry of Education (MOE) Academic Research Fund Tier one RG200/17 and the Sino-Singapore International Joint Research Institute for the funding support. P.S.L. also thanks the National Research Foundation Investigatorship, Award No. NRF-NRFI2016-05, for the funding support.

Conflict of Interest

The authors declare no conflict of interest.

Keywords

energy saving, optical modulation, responsive materials, smart windows, solar energy

Received: June 27, 2019
Revised: August 9, 2019

[1] C. G. Granqvist, *Thin Solid Films* **2016**, *614*, 90.
[2] A. Llordes, G. Garcia, J. Gazquez, D. J. Milliron, *Nature* **2013**, *500*, 323.
[3] G. Cai, J. Wang, P. S. Lee, *Acc. Chem. Res.* **2016**, *49*, 1469.
[4] Y. Cui, Y. Ke, C. Liu, Z. Chen, N. Wang, L. Zhang, Y. Zhou, S. Wang, Y. Gao, Y. Long, *Joule* **2018**, *2*, 1707.
[5] Y. Ke, C. Zhou, Y. Zhou, S. Wang, S. H. Chan, Y. Long, *Adv. Funct. Mater.* **2018**, *28*, 1800113.
[6] H. Khandelwal, A. P. H. J. Schenning, M. G. Debije, *Adv. Energy Mater.* **2017**, *7*, 1602209.
[7] E. Amasawa, N. Sasagawa, M. Kimura, M. Taya, *Adv. Energy Mater.* **2014**, *4*, 1400379.
[8] M. Isaac, D. P. van Vuuren, *Energy Policy* **2009**, *37*, 507.
[9] D. M. Kammen, D. A. Sunter, *Science* **2016**, *352*, 922.
[10] L. Pérez-Lombard, J. Ortiz, C. Pout, *Energy Build.* **2008**, *40*, 394.
[11] M. Wang, X. Xing, I. F. Perepichka, Y. Shi, D. Zhou, P. Wu, H. Meng, *Adv. Energy Mater.* **2019**, *9*, 1900433.
[12] R. Baetens, B. P. Jelle, A. Gustavsen, *Sol. Energy Mater. Sol. Cells* **2010**, *94*, 87.
[13] M. Tarantini, A. D. Loprieno, P. L. Porta, *Energy* **2011**, *36*, 2473.
[14] A. Aldawoud, *Energy Build.* **2013**, *59*, 104.
[15] J.-M. Dussault, L. Gosselin, T. Galstian, *Sol. Energy* **2012**, *86*, 3405.
[16] Y. K. Yi, J. Yin, Y. Tang, *Sol. Energy* **2018**, *163*, 140.
[17] S. Cao, S. Zhang, T. Zhang, Q. Yao, J. Y. Lee, *Joule* **2019**, *3*, 1152.
[18] C. J. Barile, D. J. Slotcavage, J. Hou, M. T. Strand, T. S. Hernandez, M. D. McGehee, *Joule* **2017**, *1*, 133.
[19] J. A. H. P. Sol, G. H. Timmermans, A. J. van Breugel, A. P. H. J. Schenning, M. G. Debije, *Adv. Energy Mater.* **2018**, *8*, 1702922.
[20] E. P. A. van Heeswijk, J. J. H. Kloos, N. Grossiord, A. P. H. J. Schenning, *J. Mater. Chem. A* **2019**, *7*, 6113.
[21] H. Kim, H.-S. Kim, J. Ha, N.-G. Park, S. Yoo, *Adv. Energy Mater.* **2016**, *6*, 1502466.
[22] G. Cai, P. Darmawan, X. Cheng, P. S. Lee, *Adv. Energy Mater.* **2017**, *7*, 1602598.
[23] Y. Wang, E. L. Runnerstrom, D. J. Milliron, *Annu. Rev. Chem. Biomol. Eng.* **2016**, *7*, 283.
[24] Commercial Building Energy Consumption Survey, https://www.eia.gov/consumption/commercial/data/2012/ (accessed: May 2019).
[25] Smart Glass Market by Technology, Application, and Geography, https://www.marketsandmarkets.com/Market-Reports/smart-glass-market-907.html?gclid=Cj0KCQjwoInnBRDDARIsANBVyATYrlUxmjlbeoXxV3VtvhGrzeLZ2O5OGU4xM70bXlapuFzbxKmaI-UaAlv-SEALw_wcB (accessed: May 2019).
[26] M. Casini, *Renewable Energy* **2018**, *119*, 923.
[27] Energy Benefits of View Dynamic Glass in Workplaces, https://view.com/assets/pdfs/workplace-white-paper.pdf (accessed: May 2019).
[28] Market Research Report: Smart Glass Market, https://www.grandviewresearch.com/industry-analysis/smart-glass-market (accessed: May 2019).
[29] SONTA, http://sonte.com/ (accessed: May 2019).
[30] Raven Window, http://www.ravenwindow.com/ (accessed: May 2019).
[31] Merck, https://www.merckgroup.com/en/brands/pm/licrivision.html (accessed: May 2019).
[32] Saint-Gobain, http://www.privalite.com/en/products (accessed: May 2019).
[33] R. J. Mortimer, D. R. Rosseinsky, P. M. Monk, *Electrochromic Materials and Devices*, John Wiley & Sons, Germany **2015**.
[34] D. Zhou, D. Xie, X. Xia, X. Wang, C. Gu, J. Tu, *Sci. China: Chem.* **2017**, *60*, 3.
[35] A. L.-S. Eh, A. W. M. Tan, X. Cheng, S. Magdassi, P. S. Lee, *Energy Technol.* **2018**, *6*, 33.
[36] P. Yang, P. Sun, W. Mai, *Mater. Today* **2016**, *19*, 394.
[37] G. Cai, A. L.-S. Eh, L. Ji, P. S. Lee, *Adv. Sustainable Syst.* **2017**, *1*, 1700074.
[38] C. G. Granqvist, M. A. Arvizu, İ. Bayrak Pehlivan, H. Y. Qu, R. T. Wen, G. A. Niklasson, *Electrochim. Acta* **2018**, *259*, 1170.
[39] Y. Li, D. Chen, R. A. Caruso, *J. Mater. Chem. C* **2016**, *4*, 10500.
[40] Y. Li, W. A. McMaster, H. Wei, D. Chen, R. A. Caruso, *ACS Appl. Nano Mater.* **2018**, *1*, 2552.
[41] W. Q. Wang, X. L. Wang, X. H. Xia, Z. J. Yao, Y. Zhong, J. P. Tu, *Nanoscale* **2018**, *10*, 8162.
[42] S. Xu, X. Li, Y. Ou, Q. Xu, X. M. Zhang, J. Xu, J. Weng, *Inorg. Chem. Front.* **2019**, *6*, 680.
[43] X. Zhang, S. Dou, W. Li, L. Wang, H. Qu, X. Chen, L. Zhang, Y. Zhao, J. Zhao, Y. Li, *Electrochim. Acta* **2019**, *297*, 223.
[44] G. Cai, M. Cui, V. Kumar, P. Darmawan, J. Wang, X. Wang, A. L.-S. Eh, K. Qian, P. S. Lee, *Chem. Sci.* **2016**, *7*, 1373.
[45] C. J. Barile, D. J. Slotcavage, M. D. McGehee, *Chem. Mater.* **2016**, *28*, 1439.

[46] T. D. Nguyen, L. P. Yeo, T. C. Kei, D. Mandler, S. Magdassi, A. I. Y. Tok, *Adv. Opt. Mater.* **2019**, *7*, 1801389.
[47] H. Ling, L. P. Yeo, Z. Wang, X. Li, D. Mandler, S. Magdassi, A. I. Y. Tok, *J. Mater. Chem. C* **2018**, *6*, 8488.
[48] H. Liang, R. Li, C. Li, C. Hou, Y. Li, Q. Zhang, H. Wang, *Mater. Horiz.* **2019**, *6*, 571.
[49] H. Li, L. McRae, C. J. Firby, M. Al-Hussein, A. Y. Elezzabi, *Nano Energy* **2018**, *47*, 130.
[50] H. Li, L. McRae, A. Y. Elezzabi, *ACS Appl. Mater. Interfaces* **2018**, *10*, 10520.
[51] S. Yan, K. P. Abhilash, L. Tang, M. Yang, Y. Ma, Q. Xia, Q. Guo, H. Xia, *Small* **2019**, *15*, e1804371.
[52] W. Cheng, J. He, K. E. Dettelbach, N. J. J. Johnson, R. S. Sherbo, C. P. Berlinguette, *Chem* **2018**, *4*, 821.
[53] A. Llordés, Y. Wang, A. Fernandez-Martinez, P. Xiao, T. Lee, A. Poulain, O. Zandi, C. A. S. Cabezas, G. Henkelman, D. J. Milliron, *Nat. Mater.* **2016**, *15*, 1267.
[54] H. Huang, X. Wang, E. Tervoort, G. Zeng, T. Liu, X. Chen, A. Sologubenko, M. Niederberger, *ACS Nano* **2018**, *12*, 2753.
[55] M. A. Arvizu, G. A. Niklasson, C. G. Granqvist, *Chem. Mater.* **2017**, *29*, 2246.
[56] S. Burkhardt, M. T. Elm, B. Lani-Wayda, P. J. Klar, *Adv. Mater. Interfaces* **2018**, *5*, 1701587.
[57] J. He, L. You, D. T. Tran, J. Mei, *ACS Appl. Mater. Interfaces* **2019**, *11*, 4169.
[58] Y. Zhan, M. R. J. Tan, X. Cheng, W. M. A. Tan, G. F. Cai, J. W. Chen, V. Kumar, S. Magdassi, P. S. Lee, *J. Mater. Chem. C* **2017**, *5*, 9995.
[59] H. Li, J. Chen, M. Cui, G. Cai, A. L.-S. Eh, P. S. Lee, H. Wang, Q. Zhang, Y. Li, *J. Mater. Chem. C* **2016**, *4*, 33.
[60] R. Giannuzzi, R. Da Silva, M. Barawi, L. De Trizio, G. Veramonti, A. Qualtieri, L. Manna, M. Manca, *ECS Trans.* **2017**, *77*, 1671.
[61] M. Barawi, G. Veramonti, M. Epifani, R. Giannuzzi, T. Sibillano, C. Giannini, A. Rougier, M. Manca, *J. Mater. Chem. A* **2018**, *6*, 10201.
[62] B.-R. Koo, K.-H. Kim, H.-J. Ahn, *Appl. Surf. Sci.* **2018**, *453*, 238.
[63] W. Q. Wang, Z. J. Yao, X. L. Wang, X. H. Xia, C. D. Gu, J. P. Tu, *J. Colloid Interface Sci.* **2019**, *535*, 300.
[64] R.-T. Wen, C. G. Granqvist, G. A. Niklasson, *Nat. Mater.* **2015**, *14*, 996.
[65] M. A. Arvizu, R. T. Wen, D. Primetzhofer, J. E. Klemberg-Sapieha, L. Martinu, G. A. Niklasson, C. G. Granqvist, *ACS Appl. Mater. Interfaces* **2015**, *7*, 26387.
[66] R. T. Wen, G. A. Niklasson, C. G. Granqvist, *ACS Appl. Mater. Interfaces* **2015**, *7*, 28100.
[67] D. Dong, W. Wang, A. Rougier, A. Barnabé, G. Dong, F. Zhang, X. Diao, *J. Mater. Chem. C* **2018**, *6*, 9875.
[68] M. A. Arvizu, C. G. Granqvist, G. A. Niklasson, *J. Phys.: Conf. Ser.* **2016**, *764*, 012009.
[69] H. Y. Qu, D. Primetzhofer, M. A. Arvizu, Z. Qiu, U. Cindemir, C. G. Granqvist, G. A. Niklasson, *ACS Appl. Mater. Interfaces* **2017**, *9*, 42420.
[70] R. T. Wen, G. A. Niklasson, C. G. Granqvist, *ACS Appl. Mater. Interfaces* **2016**, *8*, 5777.
[71] S. Heo, J. Kim, G. K. Ong, D. J. Milliron, *Nano Lett.* **2017**, *17*, 5756.
[72] L. Zheng, Y. Xu, D. Jin, Y. Xie, *Chem. Mater.* **2009**, *21*, 5681.
[73] J. A. Kerszulis, C. M. Amb, A. L. Dyer, J. R. Reynolds, *Macromolecules* **2014**, *47*, 5462.
[74] K. Cao, D. E. Shen, A. M. Österholm, J. A. Kerszulis, J. R. Reynolds, *Macromolecules* **2016**, *49*, 8498.
[75] D. T. Christiansen, J. R. Reynolds, *Macromolecules* **2018**, *51*, 9250.
[76] J. A. Kerszulis, K. E. Johnson, M. Kuepfert, D. Khoshabo, A. L. Dyer, J. R. Reynolds, *J. Mater. Chem. C* **2015**, *3*, 3211.
[77] R. H. Bulloch, J. A. Kerszulis, A. L. Dyer, J. R. Reynolds, *ACS Appl. Mater. Interfaces* **2015**, *7*, 1406.
[78] A. M. Osterholm, D. E. Shen, J. A. Kerszulis, R. H. Bulloch, M. Kuepfert, A. L. Dyer, J. R. Reynolds, *ACS Appl. Mater. Interfaces* **2015**, *7*, 1413.
[79] L. R. Savagian, A. M. Österholm, D. E. Shen, D. T. Christiansen, M. Kuepfert, J. R. Reynolds, *Adv. Opt. Mater.* **2018**, *6*, 1800594.
[80] A. M. Österholm, D. E. Shen, D. S. Gottfried, J. R. Reynolds, *Adv. Mater. Technol.* **2016**, *1*, 1600063.
[81] R. H. Bulloch, J. A. Kerszulis, A. L. Dyer, J. R. Reynolds, *ACS Appl. Mater. Interfaces* **2014**, *6*, 6623.
[82] C. Y. Hsu, J. Zhang, T. Sato, S. Moriyama, M. Higuchi, *ACS Appl. Mater. Interfaces* **2015**, *7*, 18266.
[83] M. K. Bera, T. Mori, T. Yoshida, K. Ariga, M. Higuchi, *ACS Appl. Mater. Interfaces* **2019**, *11*, 11893.
[84] M. K. Bera, C. Chakraborty, U. Rana, M. Higuchi, *Macromol. Rapid Commun.* **2018**, *39*, 1800415.
[85] C. Chakraborty, R. K. Pandey, U. Rana, M. Kanao, S. Moriyama, M. Higuchi, *J. Mater. Chem. C* **2016**, *4*, 9428.
[86] B. H. Chen, S. Y. Kao, C. W. Hu, M. Higuchi, K. C. Ho, Y. C. Liao, *ACS Appl. Mater. Interfaces* **2015**, *7*, 25069.
[87] L. Shen, L. Du, S. Tan, Z. Zang, C. Zhao, W. Mai, *Chem. Commun.* **2016**, *52*, 6296.
[88] G. Cai, X. Wang, M. Cui, P. Darmawan, J. Wang, A. L.-S. Eh, P. S. Lee, *Nano Energy* **2015**, *12*, 258.
[89] B.-H. Yu, S.-M. Ji, J.-H. Kim, J.-W. Huh, T.-H. Yoon, *J. Inf. Disp.* **2017**, *18*, 13.
[90] J. Heo, J.-W. Huh, T.-H. Yoon, *AIP Adv.* **2015**, *5*, 047118.
[91] V. K. Baliyan, K.-U. Jeong, S.-W. Kang, *Dyes Pigm.* **2019**, *166*, 403.
[92] Saint-Gobain, SegaGlass, https://www.sageglass.com/en (accessed: May 2019).
[93] M. Kim, K. J. Park, S. Seok, J. M. Ok, H.-T. Jung, J. Choe, D. H. Kim, *ACS Appl. Mater. Interfaces* **2015**, *7*, 17904.
[94] J. Huang, J. Li, J. Xu, Z. Wang, W. Sheng, H. Li, Y. Yang, W. Song, *Sol. Energy* **2019**, *188*, 857.
[95] H. Sun, Z. Xie, C. Ju, X. Hu, D. Yuan, W. Zhao, L. Shui, G. Zhou, *Polymers* **2019**, *11*, 694.
[96] S.-W. Oh, J.-M. Baek, S.-H. Kim, T.-H. Yoon, *RSC Adv.* **2017**, *7*, 19497.
[97] C.-W. Chen, A. N. Brigeman, T.-J. Ho, I. C. Khoo, *Opt. Mater. Express* **2018**, *8*, 691.
[98] J.-W. Huh, J.-H. Kim, S.-W. Oh, S.-M. Ji, T.-H. Yoon, *Dyes Pigm.* **2018**, *150*, 16.
[99] H. Khandelwal, R. C. G. M. Loonen, J. L. M. Hensen, M. G. Debije, A. P. H. J. Schenning, *Sci. Rep.* **2015**, *5*, 11773.
[100] H. Khandelwal, M. G. Debije, T. J. White, A. P. H. J. Schenning, *J. Mater. Chem. A* **2016**, *4*, 6064.
[101] J. Zhao, Y. Tian, Z. Wang, S. Cong, D. Zhou, Q. Zhang, M. Yang, W. Zhang, F. Geng, Z. Zhao, *Angew. Chem., Int. Ed.* **2016**, *55*, 7161.
[102] P. Zhang, F. Zhu, F. Wang, J. Wang, R. Dong, X. Zhuang, O. G. Schmidt, X. Feng, *Adv. Mater.* **2017**, *29*, 1604491.
[103] P. T. G. Gayathri, S. S. Shaiju, R. Remya, D. Biswapriya, *Mater. Today Energy* **2018**, *10*, 380.
[104] Y. Zhong, Z. Chai, Z. Liang, P. Sun, W. Xie, C. Zhao, W. Mai, *ACS Appl. Mater. Interfaces* **2017**, *9*, 34085.
[105] L. Zhu, C. K. N. Peh, T. Zhu, Y.-F. Lim, G. W. Ho, *J. Mater. Chem. A* **2017**, *5*, 8343.
[106] H. Li, C. J. Firby, A. Y. Elezzabi, *Joule* **2019**, https://doi.org/10.1016/j.joule.2019.06.021.
[107] G. Cai, P. Darmawan, M. Cui, J. Wang, J. Chen, S. Magdassi, P. S. Lee, *Adv. Energy Mater.* **2016**, *6*, 1501882.
[108] H. Li, L. McRae, C. J. Firby, A. Y. Elezzabi, *Adv. Mater.* **2019**, *31*, 1807065.
[109] K. Li, Y. Shao, H. Yan, Z. Lu, K. J. Griffith, J. Yan, G. Wang, H. Fan, J. Lu, W. Huang, B. Bao, X. Liu, C. Hou, Q. Zhang, Y. Li, J. Yu, H. Wang, *Nat. Commun.* **2018**, *9*, 4798.

[110] L. Hines, K. Petersen, G. Z. Lum, M. Sitti, *Adv. Mater.* **2017**, *29*, 1603483.
[111] K. Parida, J. Xiong, X. Zhou, P. S. Lee, *Nano Energy* **2019**, *59*, 237.
[112] P. Cui, K. Parida, M.-F. Lin, J. Xiong, G. Cai, P. S. Lee, *Adv. Mater. Interfaces* **2017**, *4*, 1700651.
[113] J. Xiong, P. Cui, X. Chen, J. Wang, K. Parida, M. F. Lin, P. S. Lee, *Nat. Commun.* **2018**, *9*, 4280.
[114] J. Xiong, M.-F. Lin, J. Wang, S. L. Gaw, K. Parida, P. S. Lee, *Adv. Energy Mater.* **2017**, *7*, 1701243.
[115] X. Chen, K. Parida, J. Wang, J. Xiong, M. F. Lin, J. Shao, P. S. Lee, *ACS Appl. Mater. Interfaces* **2017**, *9*, 42200.
[116] M.-H. Yeh, L. Lin, P.-K. Yang, Z. L. Wang, *ACS Nano* **2015**, *9*, 4757.
[117] K. Parida, V. Bhavanasi, V. Kumar, J. Wang, P. S. Lee, *J. Power Sources* **2017**, *342*, 70.
[118] X. Xia, Z. Ku, D. Zhou, Y. Zhong, Y. Zhang, Y. Wang, M. J. Huang, J. Tu, H. J. Fan, *Mater. Horiz.* **2016**, *3*, 588.
[119] T. G. Yun, D. Kim, Y. H. Kim, M. Park, S. Hyun, S. M. Han, *Adv. Mater.* **2017**, *29*, 1606728.
[120] A. L.-S. Eh, M.-F. Lin, M. Cui, G. Cai, P. S. Lee, *J. Mater. Chem. C* **2017**, *5*, 6547.
[121] J. Xu, Y. Zhang, T. T. Zhai, Z. Kuang, J. Li, Y. Wang, Z. Gao, Y. Y. Song, X. H. Xia, *ACS Nano* **2018**, *12*, 6895.
[122] J. R. Jennings, W. Y. Lim, S. M. Zakeeruddin, M. Gratzel, Q. Wang, *ACS Appl. Mater. Interfaces* **2015**, *7*, 2827.
[123] Y. Gao, H. Luo, Z. Zhang, L. Kang, Z. Chen, J. Du, M. Kanehira, C. Cao, *Nano Energy* **2012**, *1*, 221.
[124] L. Long, H. Ye, *Sci. Rep.* **2015**, *4*, 6427.
[125] J. A. H. P. Sol, V. Dehm, R. Hecht, F. Würthner, A. P. H. J. Schenning, M. G. Debije, *Angew. Chem.* **2018**, *130*, 1042.
[126] Y. Zhou, Y. Cai, X. Hu, Y. Long, *J. Mater. Chem. A* **2014**, *2*, 13550.
[127] J. D. Budai, J. Hong, M. E. Manley, E. D. Specht, C. W. Li, J. Z. Tischler, D. L. Abernathy, A. H. Said, B. M. Leu, L. A. Boatner, R. J. McQueeney, O. Delaire, *Nature* **2014**, *515*, 535.
[128] J. Zheng, S. Bao, P. Jin, *Nano Energy* **2015**, *11*, 136.
[129] T. Chang, X. Cao, L. R. Dedon, S. Long, A. Huang, Z. Shao, N. Li, H. Luo, P. Jin, *Nano Energy* **2018**, *44*, 256.
[130] L. Kang, Y. Gao, H. Luo, Z. Chen, J. Du, Z. Zhang, *ACS Appl. Mater. Interfaces* **2011**, *3*, 135.
[131] M. Liu, B. Su, Y. V. Kaneti, Z. Chen, Y. Tang, Y. Yuan, Y. Gao, L. Jiang, X. Jiang, A. Yu, *ACS Nano* **2017**, *11*, 407.
[132] Y. F. Gao, S. B. Wang, H. J. Luo, L. Dai, C. X. Cao, Y. L. Liu, Z. Chen, M. Kanehira, *Energy Environ. Sci.* **2012**, *5*, 6104.
[133] Z. Chen, Y. Gao, L. Kang, C. Cao, S. Chen, H. Luo, *J. Mater. Chem. A* **2014**, *2*, 2718.
[134] F. Xu, X. Cao, H. Luo, P. Jin, *J. Mater. Chem. C* **2018**, *6*, 1903.
[135] Y. F. Gao, S. B. Wang, L. T. Kang, Z. Chen, J. Du, X. L. Liu, H. J. Luo, M. Kanehira, *Energy Environ. Sci.* **2012**, *5*, 8234.
[136] N. Shen, S. Chen, Z. Chen, X. Liu, C. Cao, B. Dong, H. Luo, J. Liu, Y. Gao, *J. Mater. Chem. A* **2014**, *2*, 15087.
[137] D. Li, M. Li, J. Pan, Y. Luo, H. Wu, Y. Zhang, G. Li, *ACS Appl. Mater. Interfaces* **2014**, *6*, 6555.
[138] L. Zhong, M. Li, H. Wang, Y. Luo, J. Pan, G. Li, *CrystEngComm* **2015**, *17*, 5614.
[139] X. Qian, N. Wang, Y. Li, J. Zhang, Z. Xu, Y. Long, *Langmuir* **2014**, *30*, 10766.
[140] Y. Ke, I. Balin, N. Wang, Q. Lu, A. I. Tok, T. J. White, S. Magdassi, I. Abdulhalim, Y. Long, *ACS Appl. Mater. Interfaces* **2016**, *8*, 33112.
[141] Y. Ke, S. Ye, P. Hu, H. Jiang, S. Wang, B. Yang, J. Zhang, Y. Long, *Mater. Horiz.* **2019**, *6*, 1380.
[142] C. Liu, Y. Long, S. Magdassi, D. Mandler, *Nanoscale* **2017**, *9*, 485.
[143] Y. Ke, S. Wang, G. Liu, M. Li, T. J. White, Y. Long, *Small* **2018**, *14*, 1802025.
[144] Y. Cui, S. Shi, L. Chen, H. Luo, Y. Gao, *Phys. Chem. Chem. Phys.* **2015**, *17*, 20998.
[145] L. Dai, S. Chen, J. Liu, Y. Gao, J. Zhou, Z. Chen, C. Cao, H. Luo, M. Kanehira, *Phys. Chem. Chem. Phys.* **2013**, *15*, 11723.
[146] N. Wang, S. Liu, X. T. Zeng, S. Magdassi, Y. Long, *J. Mater. Chem. C* **2015**, *3*, 6771.
[147] S.-Y. Li, N. R. Mlyuka, D. Primetzhofer, A. Hallén, G. Possnert, G. A. Niklasson, C. G. Granqvist, *Appl. Phys. Lett.* **2013**, *103*, 161907.
[148] S. Y. Li, G. A. Niklasson, C. G. Granqvist, *J. Appl. Phys.* **2010**, *108*, 063525.
[149] S. Y. Li, G. A. Niklasson, C. G. Granqvist, *J. Appl. Phys.* **2011**, *109*, 113515.
[150] Y. Ke, X. Wen, D. Zhao, R. Che, Q. Xiong, Y. Long, *ACS Nano* **2017**, *11*, 7542.
[151] Y. Zhou, A. Huang, Y. Li, S. Ji, Y. Gao, P. Jin, *Nanoscale* **2013**, *5*, 9208.
[152] Y. Ke, Y. Yin, Q. Zhang, Y. Tan, P. Hu, S. Wang, Y. Tang, Y. Zhou, X. Wen, S. Wu, T. J. White, J. Yin, J. Peng, Q. Xiong, D. Zhao, Y. Long, *Joule* **2019**, *3*, 858.
[153] T. D. Vu, Z. Chen, X. Zeng, M. Jiang, S. Liu, Y. Gao, Y. Long, *J. Mater. Chem. C* **2019**, *7*, 2121.
[154] S. Wang, K. A. Owusu, L. Mai, Y. Ke, Y. Zhou, P. Hu, S. Magdassi, Y. Long, *Appl. Energy* **2018**, *211*, 200.
[155] R. Lopez, L. C. Feldman, R. F. Haglund Jr., *Phys. Rev. Lett.* **2004**, *93*, 177403.
[156] D. Fu, K. Liu, T. Tao, K. Lo, C. Cheng, B. Liu, R. Zhang, H. A. Bechtel, J. Wu, *J. Appl. Phys.* **2013**, *113*, 043707.
[157] S. Chen, Z. Wang, H. Ren, Y. Chen, W. Yan, C. Wang, B. Li, J. Jiang, C. Zou, *Sci. Adv.* **2019**, *5*, eaav6815.
[158] M. Li, S. Magdassi, Y. Gao, Y. Long, *Small* **2017**, *13*, 1701147.
[159] M. Li, X. Wu, L. Li, Y. Wang, D. Li, J. Pan, S. Li, L. Sun, G. Li, *J. Mater. Chem. A* **2014**, *2*, 4520.
[160] Z. Li, J. Wu, Z. Hu, Y. Lin, Q. Chen, Y. Guo, Y. Liu, Y. Zhao, J. Peng, W. Chu, C. Wu, Y. Xie, *Nat. Commun.* **2017**, *8*, 15561.
[161] N. Wang, M. Duchamp, C. Xue, R. E. Dunin-Borkowski, G. Liu, Y. Long, *Adv. Mater. Interfaces* **2016**, *3*, 1600164.
[162] M. Zhou, J. Bao, M. Tao, R. Zhu, Y. Lin, X. Zhang, Y. Xie, *Chem. Commun.* **2013**, *49*, 6021.
[163] J. Zhang, H. Jin, Z. Chen, M. Cao, P. Chen, Y. Dou, Y. Zhao, J. Li, *Chem. Mater.* **2015**, *27*, 7419.
[164] C. Cheng, K. Liu, B. Xiang, J. Suh, J. Q. Wu, *Appl. Phys. Lett.* **2012**, *100*, 103111.
[165] S. Wang, G. Liu, P. Hu, Y. Zhou, Y. Ke, C. Li, J. Chen, T. Cao, Y. Long, *Adv. Mater. Interfaces* **2018**, *5*, 1801063.
[166] Z. Chen, Y. Gao, L. Kang, J. Du, Z. Zhang, H. Luo, H. Miao, G. Tan, *Sol. Energy Mater. Sol. Cells* **2011**, *95*, 2677.
[167] Z. Zhang, Y. Gao, H. Luo, L. Kang, Z. Chen, J. Du, M. Kanehira, Y. Zhang, Z. L. Wang, *Energy Environ. Sci.* **2011**, *4*, 4290.
[168] P. Jin, G. Xu, M. Tazawa, K. Yoshimura, *Jpn. J. Appl. Phys.* **2002**, *41*, L278.
[169] C. Liu, S. Wang, Y. Zhou, H. Yang, Q. Lu, D. Mandler, S. Magdassi, C. Y. Tay, Y. Long, *J. Alloys Compd.* **2018**, *731*, 1197.
[170] M. K. Dietrich, B. G. Kramm, M. Becker, B. K. Meyer, A. Polity, P. J. Klar, *J. Appl. Phys.* **2015**, *117*, 185301.
[171] L. Hu, H. Tao, G. Chen, R. Pan, M. Wan, D. Xiong, X. Zhao, *J. Sol–Gel Sci. Technol.* **2016**, *77*, 85.
[172] Z. Zhang, Y. Gao, Z. Chen, J. Du, C. Cao, L. Kang, H. Luo, *Langmuir* **2010**, *26*, 10738.
[173] S. Chen, L. Dai, J. Liu, Y. Gao, X. Liu, Z. Chen, J. Zhou, C. Cao, P. Han, H. Luo, M. Kanahira, *Phys. Chem. Chem. Phys.* **2013**, *15*, 17537.
[174] J. Zhu, Y. Zhou, B. Wang, J. Zheng, S. Ji, H. Yao, H. Luo, P. Jin, *ACS Appl. Mater. Interfaces* **2015**, *7*, 27796.
[175] Y. Zhou, Y. Cai, X. Hu, Y. Long, *J. Mater. Chem. A* **2015**, *3*, 1121.
[176] J. Zhu, A. Huang, H. Ma, Y. Ma, K. Tong, S. Ji, S. Bao, X. Cao, P. Jin, *ACS Appl. Mater. Interfaces* **2016**, *8*, 29742.

[177] C. Liu, I. Balin, S. Magdassi, I. Abdulhalim, Y. Long, *Opt. Express* **2015**, *23*, A124.
[178] Q. Lu, C. Liu, N. Wang, S. Magdassi, D. Mandler, Y. Long, *J. Mater. Chem. C* **2016**, *4*, 8385.
[179] A. Taylor, I. Parkin, N. Noor, C. Tummeltshammer, M. S. Brown, I. Papakonstantinou, *Opt. Express* **2013**, *21*, A750.
[180] J. Zhu, A. Huang, H. Ma, Y. Chen, S. Zhang, S. Ji, S. Bao, P. Jin, *New J. Chem.* **2017**, *41*, 830.
[181] J. T. Zhu, A. B. Huang, H. B. Ma, S. H. Bao, S. D. Ji, P. Jin, *RSC Adv.* **2016**, *6*, 67396.
[182] Y. Chen, J. Zhu, H. Ma, L. Chen, R. Li, P. Jin, *Sol. Energy Mater. Sol. Cells* **2019**, *196*, 124.
[183] A. Krishna, S. Gottis, M. K. Nazeeruddin, F. Sauvage, *Adv. Funct. Mater.* **2019**, *29*, 1806482.
[184] Y. Wei, H. Chu, Y. Tian, B. Chen, K. Wu, J. Wang, X. Yang, B. Cai, Y. Zhang, J. Zhao, *Adv. Energy Mater.* **2019**, *9*, 1900612.
[185] Z. Zhao, F. Gu, H. Rao, S. Ye, Z. Liu, Z. Bian, C. Huang, *Adv. Energy Mater.* **2019**, *9*, 1802671.
[186] C. Liu, W. Li, H. Li, H. Wang, C. Zhang, Y. Yang, X. Gao, Q. Xue, H.-L. Yip, J. Fan, R. E. I. Schropp, Y. Mai, *Adv. Energy Mater.* **2019**, *9*, 1803572.
[187] S. Ahmad, P. Fu, S. Yu, Q. Yang, X. Liu, X. Wang, X. Wang, X. Guo, C. Li, *Joule* **2019**, *3*, 794.
[188] J. Lin, M. Lai, L. Dou, C. S. Kley, H. Chen, F. Peng, J. Sun, D. Lu, S. A. Hawks, C. Xie, F. Cui, A. P. Alivisatos, D. T. Limmer, P. Yang, *Nat. Mater.* **2018**, *17*, 261.
[189] M. De Bastiani, M. I. Saidaminov, I. Dursun, L. Sinatra, W. Peng, U. Buttner, O. F. Mohammed, O. M. Bakr, *Chem. Mater.* **2017**, *29*, 3367.
[190] A. Halder, D. Choudhury, S. Ghosh, A. S. Subbiah, S. K. Sarkar, *J. Phys. Chem. Lett.* **2015**, *6*, 3180.
[191] W. Ning, X.-G. Zhao, J. Klarbring, S. Bai, F. Ji, F. Wang, S. I. Simak, Y. Tao, X.-M. Ren, L. Zhang, W. Huang, I. A. Abrikosov, F. Gao, *Adv. Funct. Mater.* **2019**, *29*, 1807375.
[192] H.-K. Kwon, K.-T. Lee, K. Hur, S. H. Moon, M. M. Quasim, T. D. Wilkinson, J.-Y. Han, H. Ko, I.-K. Han, B. Park, B. K. Min, B.-K. Ju, S. M. Morris, R. H. Friend, D.-H. Ko, *Adv. Energy Mater.* **2015**, *5*, 1401347.
[193] J. Sun, H. Wang, L. Wang, H. Cao, H. Xie, X. Luo, J. Xiao, H. Ding, Z. Yang, H. Yang, *Smart Mater. Struct.* **2014**, *23*, 125038.
[194] S. M. Guo, X. Liang, C. H. Zhang, M. Chen, C. Shen, L. Y. Zhang, X. Yuan, B. F. He, H. Yang, *ACS Appl. Mater. Interfaces* **2017**, *9*, 2942.
[195] X. Liang, M. Chen, S. Guo, L. Zhang, F. Li, H. Yang, *ACS Appl. Mater. Interfaces* **2017**, *9*, 40810.
[196] X. Liang, S. Guo, M. Chen, C. Li, Q. Wang, C. Zou, C. Zhang, L. Zhang, S. Guo, H. Yang, *Mater. Horiz.* **2017**, *4*, 878.
[197] X. Liang, C. Guo, M. Chen, S. Guo, L. Zhang, F. Li, S. Guo, H. Yang, *Nanoscale Horiz.* **2017**, *2*, 319.
[198] H. Kakiuchida, A. Matsuyama, A. Ogiwara, *ACS Appl. Mater. Interfaces* **2019**, *11*, 19404.
[199] W. Zhang, S. Kragt, A. P. H. J. Schenning, L. T. de Haan, G. Zhou, *ACS Omega* **2017**, *2*, 3475.
[200] H. Y. Lee, Y. Cai, S. Bi, Y. N. Liang, Y. Song, X. M. Hu, *ACS Appl. Mater. Interfaces* **2017**, *9*, 6054.
[201] Y.-S. Yang, Y. Zhou, F. B. Y. Chiang, Y. Long, *RSC Adv.* **2017**, *7*, 7758.
[202] Y. Zhou, M. Layani, F. Y. C. Boey, I. Sokolov, S. Magdassi, Y. Long, *Adv. Mater. Technol.* **2016**, *1*, 1600069.
[203] X.-H. Li, C. Liu, S.-P. Feng, N. X. Fang, *Joule* **2019**, *3*, 290.
[204] Y. Zhou, M. Layani, S. Wang, P. Hu, Y. Ke, S. Magdassi, Y. Long, *Adv. Funct. Mater.* **2018**, *28*, 1705365.
[205] Y. Chen, L. Fan, Q. Fang, W. Xu, S. Chen, G. Zan, H. Ren, L. Song, C. Zou, *Nano Energy* **2017**, *31*, 144.
[206] M. Li, S. Ji, J. Pan, H. Wu, L. Zhong, Q. Wang, F. Li, G. Li, *J. Mater. Chem. A* **2014**, *2*, 20470.
[207] M. Li, H. Wu, L. Zhong, H. Wang, Y. Luo, G. Li, *J. Mater. Chem. C* **2016**, *4*, 1579.
[208] S. Kiruthika, G. U. Kulkarni, *Sol. Energy Mater. Sol. Cells* **2017**, *163*, 231.
[209] A. K. Singh, S. Kiruthika, I. Mondal, G. U. Kulkarni, *J. Mater. Chem. C* **2017**, *5*, 5917.
[210] S. J. Lee, D. S. Choi, S. H. Kang, W. S. Yang, S. Nahm, S. H. Han, T. Kim, *ACS Sustainable Chem. Eng.* **2019**, *7*, 7111.
[211] X. Liang, M. Chen, Q. Wang, S. Guo, L. Zhang, H. Yang, *J. Mater. Chem. C* **2018**, *6*, 7054.
[212] F. Chen, Y. Ren, J. Guo, F. Yan, *Chem. Commun.* **2017**, *53*, 1595.
[213] X. Liao, C. Shi, T. Wang, B. Qie, Y. Chen, P. Yang, Q. Cheng, H. Zhai, M. Chen, X. Wang, X. Chen, Y. Yang, *Adv. Energy Mater.* **2019**, *9*, 1802998.
[214] J. Cui, F. R. Poblete, Y. Zhu, *Adv. Funct. Mater.* **2018**, *28*, 1802768.
[215] B. H. Kim, F. Liu, Y. Yu, H. Jang, Z. Xie, K. Li, J. Lee, J. Y. Jeong, A. Ryu, Y. Lee, D. H. Kim, X. Wang, K. Lee, J. Y. Lee, S. M. Won, N. Oh, J. Kim, J. Y. Kim, S.-J. Jeong, K.-I. Jang, S. Lee, Y. Huang, Y. Zhang, J. A. Rogers, *Adv. Funct. Mater.* **2018**, *28*, 1803149.
[216] Y. Tang, G. Lin, S. Yang, Y. K. Yi, R. D. Kamien, J. Yin, *Adv. Mater.* **2017**, *29*, 1604262.
[217] D. Kim, E. Lee, H. S. Lee, J. Yoon, *Sci. Rep.* **2015**, *5*, 7646.
[218] Z. Xu, S. Wang, X.-Y. Hu, J. Jiang, X. Sun, L. Wang, *Sol. RRL* **2018**, *2*, 1800204.
[219] D. Cao, C. Xu, W. Lu, C. Qin, S. Cheng, *Sol. RRL* **2018**, *2*, 1700219.
[220] M. Wu, Y. Shi, R. Li, P. Wang, *ACS Appl. Mater. Interfaces* **2018**, *10*, 39819.
[221] N. C. Davy, M. Sezen-Edmonds, J. Gao, X. Lin, A. Liu, N. Yao, A. Kahn, Y.-L. Loo, *Nat. Energy* **2017**, *2*, 17104.
[222] H. Chen, L. Shao, T. Ming, Z. Sun, C. Zhao, B. Yang, J. Wang, *Small* **2010**, *6*, 2272.
[223] S. Qin, Q. Zhang, X. Yang, M. Liu, Q. Sun, Z. L. Wang, *Adv. Energy Mater.* **2018**, *8*, 1800069.
[224] S. Dai, X. Zhan, *Adv. Energy Mater.* **2018**, *8*, 1800002.
[225] Y. Li, G. Xu, C. Cui, Y. Li, *Adv. Energy Mater.* **2018**, *8*, 1701791.
[226] H. Shi, R. Xia, G. Zhang, H.-L. Yip, Y. Cao, *Adv. Energy Mater.* **2019**, *9*, 1803438.
[227] S. Chen, H. Yao, B. Hu, G. Zhang, L. Arunagiri, L.-K. Ma, J. Huang, J. Zhang, Z. Zhu, F. Bai, W. Ma, H. Yan, *Adv. Energy Mater.* **2018**, *8*, 1800529.
[228] J. Zhou, Y. Gao, Z. Zhang, H. Luo, C. Cao, Z. Chen, L. Dai, X. Liu, *Sci. Rep.* **2013**, *3*, 3029.
[229] F. Guo, S. Chen, Z. Chen, H. Luo, Y. Gao, T. Przybilla, E. Spiecker, A. Osvet, K. Forberich, C. J. Brabec, *Adv. Opt. Mater.* **2015**, *3*, 1524.
[230] S. Wang, M. Liu, L. Kong, Y. Long, X. Jiang, A. Yu, *Prog. Mater. Sci.* **2016**, *81*, 1.
[231] M. E. A. Warwick, R. Binions, *J. Mater. Chem. A* **2014**, *2*, 3275.
[232] Y. Mei, S. Kiravittaya, S. Harazim, O. G. Schmidt, *Mater. Sci. Eng., R* **2010**, *70*, 209.
[233] N. Bowden, S. Brittain, A. G. Evans, J. W. Hutchinson, G. M. Whitesides, *Nature* **1998**, *393*, 146.
[234] P. Kim, Y. Hu, J. Alvarenga, M. Kolle, Z. Suo, J. Aizenberg, *Adv. Opt. Mater.* **2013**, *1*, 381.
[235] B. Jiang, L. Liu, Z. Gao, W. Wang, *Adv. Opt. Mater.* **2018**, *6*, 1800195.
[236] M. Shrestha, G. K. Lau, *Opt. Lett.* **2016**, *41*, 4433.
[237] G. Lin, P. Chandrasekaran, C. Lv, Q. Zhang, Y. Tang, L. Han, J. Yin, *ACS Appl. Mater. Interfaces* **2017**, *9*, 26510.
[238] Z. Li, Z. Yao, W. Yu, G. M. Wendland, X. Yin, J. Xiao, Z. Li, Z. Yao, W. Yu, G. M. Wendland, *Adv. Opt. Mater.* **2017**, *5*, 1700425.
[239] S. Zeng, D. Zhang, W. Huang, Z. Wang, S. G. Freire, X. Yu, A. T. Smith, E. Y. Huang, H. Nguon, L. Sun, *Nat. Commun.* **2016**, *7*, 11802.

[240] J. Yin, J. L. Yagüe, D. Eggenspieler, K. K. Gleason, M. C. Boyce, *Adv. Mater.* **2012**, *24*, 5441.
[241] C. Cao, H. F. Chan, J. Zang, K. W. Leong, X. Zhao, *Adv. Mater.* **2014**, *26*, 1763.
[242] H.-N. Kim, D. Ge, E. Lee, S. Yang, *Adv. Mater.* **2018**, *30*, 1803847.
[243] S. G. Lee, D. Y. Lee, H. S. Lim, D. H. Lee, S. Lee, K. Cho, *Adv. Mater.* **2010**, *22*, 5013.
[244] M. Shrestha, A. Asundi, G.-K. Lau, *ACS Photonics* **2018**, *5*, 3255.
[245] S. Zeng, R. Li, S. G. Freire, V. M. M. Garbellotto, E. Y. Huang, A. T. Smith, C. Hu, W. R. T. Tait, Z. Bian, G. Zheng, D. Zhang, L. Sun, *Adv. Mater.* **2017**, *29*, 1700828.
[246] H.-Y. Ong, M. Shrestha, G.-K. Lau, *Appl. Phys. Lett.* **2015**, *107*, 132902.
[247] D. van den Ende, J.-D. Kamminga, A. Boersma, T. Andritsch, P. G. Steeneken, *Adv. Mater.* **2013**, *25*, 3438.
[248] H. Hou, J. Yin, X. Jiang, *Adv. Mater.* **2016**, *28*, 9126.
[249] Q. Zhang, J. Yin, *J. Mech. Phys. Solids* **2018**, *118*, 40.
[250] Q. Zhang, Y. Tang, M. Hajfathalian, C. Chen, K. T. Turner, D. A. Dikin, G. Lin, J. Yin, *ACS Appl. Mater. Interfaces* **2017**, *9*, 44938.
[251] J. Zang, S. Ryu, N. Pugno, Q. Wang, Q. Tu, M. J. Buehler, X. Zhao, *Nat. Mater.* **2013**, *12*, 321.
[252] A. V. Thomas, B. C. Andow, S. Shravan, E. Osman, Y. Jie, A. H. Dyson, K. Nikhil, *Adv. Mater.* **2015**, *27*, 3256.
[253] H. Xian, M. Liu, X. Wang, F. Ye, P. Wen, H. Bai, Y. Liu, W. Wang, *Nanotechnology* **2019**, *30*, 085705.
[254] M. K. Blees, A. W. Barnard, P. A. Rose, S. P. Roberts, K. L. McGill, P. Y. Huang, A. R. Ruyack, J. W. Kevek, B. Kobrin, D. A. Muller, P. L. McEuen, *Nature* **2015**, *524*, 204.
[255] A. Lamoureux, K. Lee, M. Shlian, S. R. Forrest, M. Shtein, *Nat. Commun.* **2015**, *6*, 8092.
[256] Y. Zhang, Z. Yan, K. Nan, D. Xiao, Y. Liu, H. Luan, H. Fu, X. Wang, Q. Yang, J. Wang, W. Ren, H. Si, F. Liu, L. Yang, H. Li, J. Wang, X. Guo, H. Luo, L. Wang, Y. Huang, J. A. Rogers, *Proc. Natl. Acad. Sci. USA* **2015**, *112*, 11757.
[257] Z. Wang, W. Fan, Q. He, Y. Wang, X. Liang, S. Cai, *Extreme Mech. Lett.* **2017**, *11*, 42.
[258] X. Yao, Y. Hu, A. Grinthal, T.-S. Wong, L. Mahadevan, J. Aizenberg, *Nat. Mater.* **2013**, *12*, 529.
[259] D. Ge, E. Lee, L. Yang, Y. Cho, M. Li, D. S. Gianola, S. Yang, *Adv. Mater.* **2015**, *27*, 2489.
[260] F. López Jiménez, S. Kumar, P. M. Reis, *Adv. Opt. Mater.* **2016**, *4*, 620.
[261] E. H. Ko, H. J. Kim, S. M. Lee, T. W. Kim, H. K. Kim, *Sci. Rep.* **2017**, *7*, 46739.
[262] R. Pardo, M. Zayat, D. Levy, *Chem. Soc. Rev.* **2011**, *40*, 672.
[263] V. I. Minkin, *Chem. Rev.* **2004**, *104*, 2751.
[264] H. Li, S. Pu, G. Liu, B. Chen, *Dyes Pigm.* **2014**, *101*, 15.
[265] X. Chen, N. I. Islamova, S. P. Garcia, J. A. DiGirolamo, W. J. Lees, *J. Org. Chem.* **2009**, *74*, 6777.
[266] J. Harada, M. Taira, K. Ogawa, *Cryst. Growth Des.* **2017**, *17*, 2682.
[267] M. Morimoto, S. Kobatake, M. Irie, *J. Am. Chem. Soc.* **2003**, *125*, 11080.
[268] M. Schulz-Senft, P. J. Gates, F. D. Sönnichsen, A. Staubitz, *Dyes Pigm.* **2017**, *136*, 292.
[269] Y.-S. Nam, I. Yoo, O. Yarimaga, I. S. Park, D.-H. Park, S. Song, J.-M. Kim, C. W. Lee, *Chem. Commun.* **2014**, *50*, 4251.
[270] S. Kawauchi, H. Yoshida, N. Yamashina, M. Ohira, S. Saeda, M. Irie, *Bull. Chem. Soc. Jpn.* **1990**, *63*, 267.
[271] H. Xia, K. Xie, G. Zou, *Molecules* **2017**, *22*, 2236.
[272] D.-Y. Kim, S.-A. Lee, H. Kim, S. Min Kim, N. Kim, K.-U. Jeong, *Chem. Commun.* **2015**, *51*, 11080.
[273] H. Kuroiwa, Y. Inagaki, K. Mutoh, J. Abe, *Adv. Mater.* **2019**, *31*, 1805661.
[274] J. Bonefacino, M.-L. V. Tse, C.-F. J. Pun, X. Cheng, W. K. E. Chan, A. Boersma, H.-Y. Tam, *Opt. Photonics J.* **2013**, *03*, 11.
[275] W. Li, P. Da, Y. Zhang, Y. Wang, X. Lin, X. Gong, G. Zheng, *ACS Nano* **2014**, *8*, 11770.
[276] J. N. Schrauben, R. Hayoun, C. N. Valdez, M. Braten, L. Fridley, J. M. Mayer, *Science* **2012**, *336*, 1298.
[277] N. Li, Y. Li, Y. Zhou, W. Li, S. Ji, H. Yao, X. Cao, P. Jin, *Sol. Energy Mater. Sol. Cells* **2017**, *160*, 116.
[278] Y. Wang, L. Pan, Y. Li, A. I. Gavrilyuk, *Appl. Surf. Sci.* **2014**, *314*, 384.
[279] L. Pan, Y. Wang, X. Wang, H. Qu, J. Zhao, Y. Li, A. Gavrilyuk, *Phys. Chem. Chem. Phys.* **2014**, *16*, 20828.
[280] C. Sun, G. Xu, X.-M. Jiang, G.-E. Wang, P.-Y. Guo, M.-S. Wang, G.-C. Guo, *J. Am. Chem. Soc.* **2018**, *140*, 2805.
[281] G. Ju, Y. Hu, L. Chen, X. Wang, *J. Photochem. Photobiol., A* **2013**, *251*, 100.
[282] W. H. Armistead, S. D. Stookey, *Science* **1964**, *144*, 150.
[283] S. Kawata, Y. Kawata, *Chem. Rev.* **2000**, *100*, 1777.
[284] M. Irie, *Chem. Rev.* **2000**, *100*, 1683.
[285] S. Wang, W. Fan, Z. Liu, A. Yu, X. Jiang, *J. Mater. Chem. C* **2018**, *6*, 191.
[286] K. Thummavichai, Y. Xia, Y. Zhu, *Prog. Mater. Sci.* **2017**, *88*, 281.
[287] F. Amano, D. Li, B. Ohtani, *Chem. Commun.* **2010**, *46*, 2769.
[288] M. Hočevar, U. Opara Krašovec, *Sol. Energy Mater. Sol. Cells* **2016**, *154*, 57.
[289] Z.-G. Zhao, Z.-F. Liu, M. Miyauchi, *Adv. Funct. Mater.* **2010**, *20*, 4162.
[290] K. Adachi, M. Tokushige, K. Omata, S. Yamazaki, Y. Iwadate, *ACS Appl. Mater. Interfaces* **2016**, *8*, 14019.
[291] M. J. Kang, E. G. Santoro, Y. S. Kang, *ACS Omega* **2018**, *3*, 9505.
[292] C. Kormann, D. W. Bahnemann, M. R. Hoffmann, *J. Phys. Chem.* **1988**, *92*, 5196.
[293] F. N. Castellano, J. M. Stipkala, L. A. Friedman, G. J. Meyer, *Chem. Mater.* **1994**, *6*, 2123.
[294] U. Joost, A. Šutka, M. Oja, K. Smits, N. Döbelin, A. Loot, M. Järvekülg, M. Hirsimäki, M. Valden, E. Nõmmiste, *Chem. Mater.* **2018**, *30*, 8968.
[295] H. Miyazaki, T. Matsuura, T. Ota, *RSC Adv.* **2017**, *7*, 2388.
[296] M. Wang, K. J. Koski, *ACS Nano* **2015**, *9*, 3226.
[297] Windows and Building Envelope Research and Development: Roadmap for Emerging Technologies, https://www.energy.gov/sites/prod/files/2014/02/f8/BTO_windows_and_envelope_report_3.pdf (accessed: May 2019).
[298] L. E. Helseth, X. D. Guo, *Renewable Energy* **2016**, *99*, 845.
[299] D. K. Nandakumar, S. K. Ravi, Y. Zhang, N. Guo, C. Zhang, S. C. Tan, *Energy Environ. Sci.* **2018**, *11*, 2179.
[300] P. Mazumder, Y. Jiang, D. Baker, A. Carrilero, D. Tulli, D. Infante, A. T. Hunt, V. Pruneri, *Nano Lett.* **2014**, *14*, 4677.
[301] E. Mitridis, T. M. Schutzius, A. Sicher, C. U. Hail, H. Eghlidi, D. Poulikakos, *ACS Nano* **2018**, *12*, 7009.
[302] T. Yamazaki, M. Tenjimbayashi, K. Manabe, T. Moriya, H. Nakamura, T. Nakamura, T. Matsubayashi, Y. Tsuge, S. Shiratori, *Ind. Eng. Chem. Res.* **2019**, *58*, 2225.
[303] E. Castellón, M. Zayat, D. Levy, *Adv. Funct. Mater.* **2018**, *28*, 1704717.
[304] G. Cai, J. Wang, A. L.-S. Eh, J. Chen, K. Qian, J. Xiong, G. Thangavel, P. S. Lee, *ACS Appl. Mater. Interfaces* **2018**, *10*, 37685.
[305] B. P. V. Heiz, Z. Pan, G. Lautenschläger, C. Sirtl, M. Kraus, L. Wondraczek, *Adv. Sci.* **2017**, *4*, 1600362.
[306] B. P. V. Heiz, Z. Pan, L. Su, S. T. Le, L. Wondraczek, *Adv. Sustainable Syst.* **2018**, *2*, 1700140.
[307] B. P. V. Heiz, L. Su, Z. Pan, L. Wondraczek, *Adv. Sustainable Syst.* **2018**, *2*, 1800047.